ETH zürich

Dissertation No. 29784

Microfluidic systems for quantitative analysis of secreted proteins at the single-cell level

by

Claudius L. Dietsche

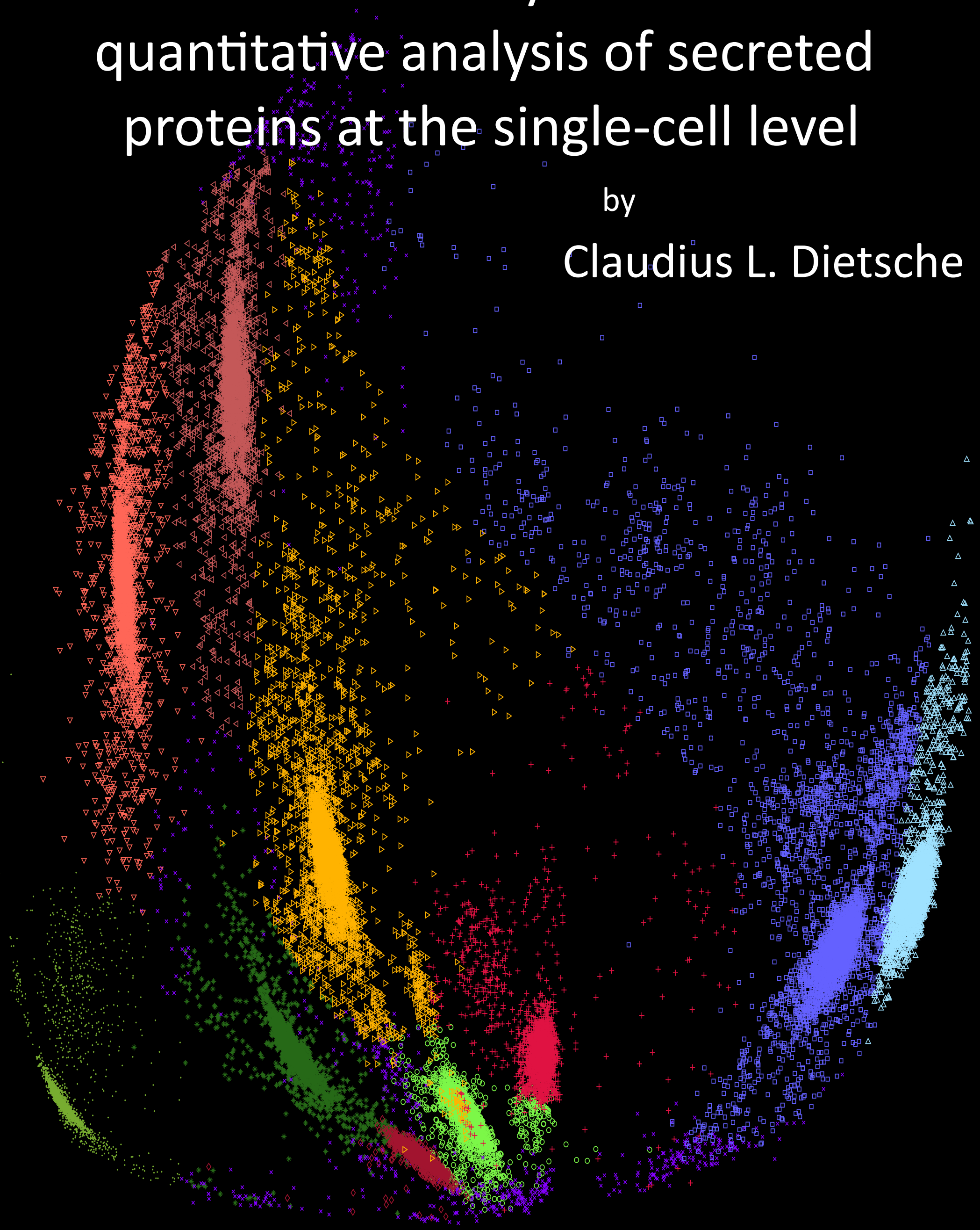

Diss. ETH No. 29784

MICROFLUIDIC SYSTEMS FOR QUANTITATIVE ANALYSIS OF SECRETED PROTEINS AT THE SINGLE-CELL LEVEL

A thesis submitted to attain the degree of

DOCTOR of SCIENCES

(Dr. sc. ETH Zurich)

presented by

CLAUDIUS L. DIETSCHE

MSc ETH ME, ETH Zurich,
born on 21.10.1989

Accepted on the recommendation of

Prof. Dr. Petra S. Dittrich
Prof. Dr. Christoph Merten
Prof. Dr. Ute Resch-Genger

2024

Contents

List of figures

List of abbreviations

μTAS	Miniaturized total analysis systems
5PL	Five parameter logistic curve fitting
ABS	Acrylonitrile butadiene styrene
AC	Alternating current
AF4	Asymmetric flow field-flow fractionation
Ag	Silver
AgCl	Silver chloride
AM	Acetoxymethyl
Au	Gold
B1	First fluorescence barcode (1) in the red fluorescence spectrum
B2	Second fluorescence barcode (2) in the far-red fluorescence spectrum
BSA	Bovine serum albumin
CAD	Computer-aided design
CCL18	Chemokine (C-C motif) ligand 18 (alias: MIP-4)
CCL3	Chemokine (C-C motif) ligand 3 (alias: MIP-1α)
CFI	Chromatic aberration-free infinity
CNI	Compact nanoimprint
CNN	Convolutional neural network
COC	Cyclic olefin copolymer
CRISPR	Clustered regularly interspaced short palindromic repeats
CTC	Circulating tumor cell
DAPI	4′,6-Diamidin-2-phenylindol
DC	Direct current
DI	Deionized water
DLD	Deterministic lateral displacement
DM	Dichroic mirror
DMEM	Dulbecco's modified Eagle's medium
DMF	Digital microfluidics

DNA	Deoxyribonucleic acid
DTX	Docetaxel (Taxotere)
EIS	Electrical impedance spectroscopy
ELISA	Enzyme-linked immunosorbent assay
ELISpot	Enzyme-linked immunosorbent spot
EM	Emission
ER	Elastic reversible
ESI-MS	Electrospray ionization mass spectrometry
ETP	Electromagnet-triggered pillar
EV	Extracellular vesicles
EX	Excitation
F127-DA	Pluronic F127 diacrylate
F127-PDL	Poly-d-lysine-conjugated Pluronic F127
FBS	Foetal bovine serum
FC-40	Immiscible fluorocarbon oil
FDM	Fused deposition modeling
FRET	Förster resonance energy transfer
Gal-3	Galectin-3
Gal-3bp	Galectin-3 binding protein
GAPDH	Glycerinaldehyd-3-phosphat-dehydrogenase
GFP	Green fluorescent protein
HER2	Human epidermal growth factor receptor 2
HFE-7500	Immiscible fluorocarbon oil
HPLC	High pressure liquid chromatography
ICP-MS	Inductively coupled plasma mass spectrometry
IgG	Immunoglobulin G
IL-1β	Interleukin-1β
IL-10	Interleukin-10
IL-13	Interleukin-13
IL-4	Interleukin-4
IL-6	Interleukin-6
IL-8	Interleukin-8
INF-γ	Interferon-γ
IP-10	Interferon gamma-induced protein 10 (alias: CXCL10)
IPA	Isopropyl alcohol
LLI	Liquid-liquid interfaces
LOD	Limit of detection
LPS	Lipopolysaccharide
MΦ	Unpolarized macrophages (native)
$M_{treated}$	Macrophages treated with the supernatant from cancer cells

M0	Unpolarized macrophages (native)
M1	Classically activated macrophages (pro-inflammatory)
M2	Alternatively activated macrophages (anti-inflammatory)
MALDI-MS	Matrix-assisted laser desorption/ionization mass spectrometry
MCAM	Melanoma cell adhesion molecule
MCF-7	Human breast cancer cell line
MCP-1	Monocyte chemoattractant protein-1 (alias: CCL2)
MCSP	Melanoma-associated chondroitin sulfate proteoglycan
MIP-1α	Macrophage inflammatory protein-1 α (alias: CCL3)
MIP-4	Macrophage inflammatory protein-4 (alias: CCL18)
miRNA	Micro ribonucleic acid
mRNA	Messenger ribonucleic acid
MS	Mass spectrometry
NMR	Nuclear magnetic resonance
OPN	Osteopontin (alias: SPP1)
PA	Polyacrylamide
PBS	Phosphate buffer saline
PC	Polycarbonate
PDMS	Poly(dimethylsiloxane)
PE	Phycoerythrin
PEG	Polyethylene glycol
PET	Positron emission tomography
PFOTS	Perfluorodecyltrichlorosilane
ph	Potential of hydrogen
PLA	Polylactic acid
PMA	Phorbol 12-myristate 13-acetate
POC	Point-of-care
PP	Polypropylene
PTFE	Polytetrafluoroethylene
PTX	Paclitaxel (Taxol)
RNA	Ribonucleic acid
RNAseq	RNA sequencing
ROS	Reactive oxygen species
RPMI	Roswell Park Memorial Institute
RT-LAMP	Reverse transcription loop-mediated isothermal amplification
SARS-CoV-2	Severe acute respiratory syndrome coronavirus 2
SAW	Surface acoustic waves
SCBC	Single-cell barcode chip
SERS	Surface-enhanced Raman scattering
SLA	Stereolithography

SMP	Shape memory polymer
SU-8	Epoxy-based negative photoresist
TAM	Tumour associated macrophages
THP-1	Human monocytic cell line
TiO_2	Titanium dioxide
TME	Tumour microenvironment
TNF-α	Tumor necrosis factor α
UV	Ultraviolet
VEGF	Vascular endothelial growth factor
WBC	White blood cell

Abstract

Cancer is responsible for million of deaths in every population across all continents. Extensive research is conducted to fundamentally understand the disease; specifically, the formation and progression of tumours and their surrounding environment. The highly heterogeneous cell population in the tumour microenvironment consists of a vast array of different cells. Particularly, the body's own immune cells are a significant portion of the tumour microenvironment and interact with their surrounding by secretion of various stimuli. They play a crucial role in the development of the tumour and have the potential to alter the course of the disease. A key classification parameter of anti- or pro-tumoural cells is their secretion profile. However, the detection and quantification of secreted proteins from single cells is still challenging. Specifically, thousands of single cells need to be analysed to obtain significant findings which necessitates high throughput.

Microfluidic devices are well suited to overcome these challenges. Their small geometries are on the same length scale as mammalian cells and are perfectly suited to control and handle cell suspensions. The laminar flow in micro-scaled channels can be utilized to capture and isolate single cells. The secreted proteins are concentrated in the small volumes increasing the sensitivity of commonly applied detection and quantification assays. This thesis exploits microfluidic systems to tackle the challenges for single-cell protein secretion analysis and presents two microfluidic platforms.

The first device developed in this thesis is capable of measuring the secreted proteins of up to 1084 single cells. The cells are captured with hydrodynamic traps and isolated with pneumatically activated donutshaped valves. The cells are co-captured with magnetic beads embedded with a fluorescent barcode enabling multiplexed secretion measurements. As a proof of concept, the versatile platform was used to characterize different macrophage polarization states based on their secretion profile. The profile of pro- and anti-inflammatory macrophages were compared to macrophages stimulated with cancerous cell supernatant. The findings help to understand the impact of the tumour microenvironment on the immune cells in it.

The second device increased the throughput of analysed cells from 10^3 to 10^5 by two orders of magnitude while reducing the complexity of the system drastically. Instead of the actively controlled valves to isolate single cells, a two-phase system in combination with a microwell array was developed. The open system is operated by only using standard laboratory equipment resulting in an easy-to-use system. With the developed device, the impact of different stimuli on the secretion profile of native macrophages was investigated. Additionally, the impact of anti-cancer drugs on the macrophages was examined and compared to pro- and anti-inflammatory stimuli.

Recently, it became apparent that the cellular heterogeneity is a crucial factor in characterization of populations, disease development, and fundamental research. Specifically for the realization of personalized medicine, it is crucial to develop easy-to-use devices which can be applied in standard laboratories. The final platform presented in this thesis is a step towards adaptable and easily operatable microfluidic devices.

Kurzfassung

Krebs ist in jeder Bevölkerungsschicht und auf allen Kontinenten für Millionen von Todesfällen verantwortlich. Es werden umfangreiche Forschungsarbeiten durchgeführt, um die Krankheit grundlegend zu verstehen, insbesondere bezüglich der Entstehung und des Fortschreitens von Tumoren und ihrer Umgebung. Eine der Herausforderungen ist die äußerst heterogene Zellpopulation in der Mikroumgebung des Tumors, die aus einer Vielzahl unterschiedlicher Zelltypen besteht. Vor allem die körpereigenen Immunzellen sind ein bedeutender Teil der Mikroumgebung und interagieren mit ihrer Umgebung, indem sie verschiedene Reize absondern. Sie spielen eine entscheidende Rolle bei der Entwicklung des Tumors und haben das Potenzial, den Krankheitsverlauf zu verändern. Ein wichtiger Parameter zur Klassifizierung von anti- und protumorösen Zellen ist ihr Sekretionsprofil. Der Nachweis und die Quantifizierung von sekretierten Proteinen aus einzelnen Zellen ist jedoch nach wie vor eine Herausforderung. Insbesondere müssen tausende einzelner Zellen analysiert werden, um aussagekräftige Ergebnisse zu erhalten, was einen hohen Durchsatz voraussetzt.

Mikrofluidische Geräte sind gut geeignet, um diese Herausforderungen zu meistern. Ihre kleinen Geometrien liegen auf der gleichen Längenskala wie Säugetierzellen und eignen sich für die Kontrolle und Handhabung von Zellsuspensionen. Die laminare Strömung in solch kleinen Kanälen kann genutzt werden, um einzelne Zellen einzufangen und zu isolieren. Die sekretierten Proteine sind in den kleinen Volumina hochkonzentriert, was die Empfindlichkeit der üblicherweise verwendeten Nachweis- und Quantifizierungstests erhöht. In dieser Arbeit werden mikrofluidische Systeme genutzt, um die Herausforderungen bei der Messung der Einzelzellproteinsekretion zu bewältigen und zwei mikrofluidische Plattformen vorgestellt.

Das erste in dieser Arbeit entwickelte Gerät ist in der Lage, die sekretierten Proteine von bis zu 1084 Einzelzellen zu messen. Die Zellen werden mit hydrodynamischen Fallen eingefangen und mit pneumatisch aktivierten, Donut-förmigen Ventilen isoliert. Die Zellen werden mit magnetischen Kügelchen eingefangen, die mit einem fluoreszierenden Barcode versehen sind, was Multiplexmessungen der Sekretion ermöglicht. Zur Erprobung des Konzepts wurde die vielseitige Plattform zur Charakterisierung von Makrophagen anhand ihres Sekretionsprofils eingesetzt. Das Profil von pro- und antiinflammatorischen Makrophagen wurde mit Makrophagen verglichen, die mit dem Überstand von Krebszellen stimuliert wurden. Die Ergebnisse helfen, die Auswirkungen der Mikroumgebung des Tumors auf die darin befindlichen Immunzellen zu verstehen.

Mit dem zweiten Gerät konnte die Anzahl der analysierten Zellen von 10^3 auf 10^5 um zwei Größenordnungen erhöht und gleichzeitig die Komplexität des Systems drastisch reduziert werden. Anstelle der aktiv gesteuerten Ventile zur Isolierung einzelner Zellen wurde ein Zwei-Phasen-System in Kombination mit einem Mikrotiterplatten-Array entwickelt. Das offene System wird nur mit Standard-Laborausrüstung betrieben, was zu einem einfach zu bedienenden System führt. Mit dem entwickelten Gerät wurde der Einfluss verschiedener Stimuli auf das Sekretionsprofil nativer Makrophagen untersucht. Außerdem wurde die Wirkung von Krebsmedikamenten auf die Makrophagen untersucht und mit normalen Stimuli verglichen.

Kürzlich wurde deutlich, dass die zelluläre Heterogenität ein entscheidender Faktor bei der Charakterisierung von Populationen, der Krankheitsentwicklung und in der Grundlagenforschung ist. Insbesondere für die Verwirklichung der personalisierten Medizin ist es von entscheidender Bedeutung, einfach zu bedienende Geräte zu entwickeln, die in Standardlabors eingesetzt werden können. Die in dieser Arbeit vorgestellte Plattform ist ein Schritt in Richtung anpassungsfähiger und leicht bedienbarer mikrofluidischer Geräte.

Chapter 1

Introduction

1.1 Tumours and the tumour microenvironment

Cancer is a widespread disease with approximately 19 million new cases every year worldwide [1]. There are 97 classified cancer types which are responsible for nearly 10 million deaths every year. The cumulative probability to get cancer between the age of 0-74 is worldwide around 20% and can go as high as 40% in certain countries. Over the years, treatments for varies types of cancer were developed and successfully implemented [2–4]. However, due to the diversity of cancer types and heterogeneity of cancer, the need for more and better treatments remains high.

Cancer is caused by a genomic instability in single or multiple cells leading to uncontrolled cell growth. Usually, genetic mutations lead to a disruption of the cell life cycle, resulting in uninhibited cell proliferation. Initially, the dysfunctional cell clusters, also known as benign tumours, are contained, and do not invade neighbouring tissues. However, many benign tumours have the potential the transform into a malignant tumour that extravasates into neighbouring tissues and metastasize in the body. This process is called tumour progression and is strongly impacted by the biochemical environment of the tumour [5, 6]. A key challenge is the understanding of the complex interplay between this heterogeneous cell population of cancer cells, immune cells, and its surrounding tissue [7, 8].

1.1.1 The tumour microenvironment (TME)

The long-established view that a tumour consists exclusively of cancer cells is replaced by a more comprehensive understanding of cancerous cells and their surround environment (Fig. 1.1). These cells and tissues inside and around the tumour are known as the tumour microenvironment (TME) [5, 9]. The cancerous cells interact with surrounding cells and tissue transforming a stable and healthy environment in a tumour supporting surrounding. The secretion of chemokines such as MCP-1 or IL-8 by the tumour cells lead to the recruitment of additional cells resulting in an increase of immunosuppressive cells inside the TME [10, 11]. Secreted cytokines such as VEGF and IL-6 upregulate angiogenesis resulting in formation of new vasculature in the TME [12]. This interplay between signaling proteins such as chemokines and cytokines from numerous cells and cell types results in a highly complex environment.

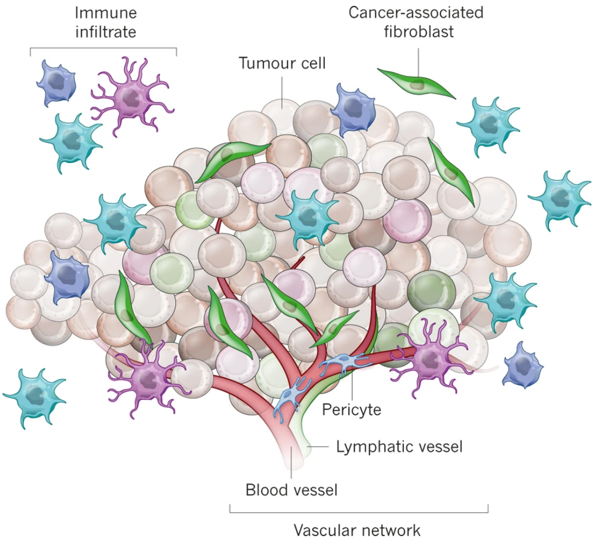

Figure 1.1: The TME consists of a vast variety of different cell types. Tumours recruit and adapt host body cells including immune cells, stromal cell, and blood and lymphatic vessels. Reprinted from Junttila et al. [8].

Immune cells residing in the TME have a crucial impact on the development of tumour progression [13, 14]. The immune cells in the TME are known to have an ambivalent role in the progression of the tumour. They are recruited and can be altered by the TME to exhibit immunosuppressing properties leading to a pro-tumoural environment [14, 15]. However, depending on the complex cytokine and chemokine profile in the TME, immune cells can exhibit anti-tumoural properties supressing tumour growth. The countless different cell types and phenotypes inside the TME result in a heterogeneous population. Therefore, to fundamentally understand the complex TME, it is crucial to investigate the secretion profile of cells at the single-cell level [8, 13, 16].

1.1.2 Macrophages

Macrophages are part of the innate immune system responding to pathogens in the body. Macrophages can be found in all tissues in the body and are the main initiator for inflammatory and anti-inflammatory responses [17]. With the secretion of cytokines and chemokines they can activate the immune response of surrounding cells. However, the highly plastic cells can change their phenotype according to external stimuli such as cytokines, chemokines, or extracellular vesicles [18, 19]. This change in phenotype is also known as polarization or activation of the macrophages. They can be characterized mainly in two extreme polarization states: pro-inflammatory macrophages also known as M1 macrophages and anti-inflammatory macrophage also known as M2 or alternatively activated macrophages. Even though most of the publications only reference the extreme polarization states of macrophages, it was shown that macrophage polarization is more a spectrum between the two extreme variants [17, 20]. The extreme M1 macrophages are polarized with lipopolysaccharide (LPS) and interferon γ (INF-γ) simulating an infection and are associated with anti-tumoural properties. In contrast, the anti-inflammatory M2 phenotype is stimulated with a combination of interleukin 4 (IL-4) and IL-13, and it is generally accepted that they exhibit immunosuppressing properties.

Tumour associated macrophages (TAM)

The macrophages residing in the TME are referred to as tumour associated macrophages (TAM). They are one of the most abundant immune cells in the TME [21]. The highly plastic macrophages are designed to respond to different cues and stimuli and, therefore, are impacted by the cytokines secreted in the TME [22, 23]. Depending on protein profiles within the TME, they can adopt phenotypes supporting tumour growth or, in contrast, show tumour supressing properties. TAMs exhibiting anti-tumoural properties are comparable to the M1 phenotype. They inhibit tumour growth and progression by secreting cytokines such as tumor necrosis factor α (TNF-α) and interferon gamma-induced protein 10 (IP-10) [21]. On the contrary, most TAMs exhibit pro-tumoural properties and are comparable to the M2 phenotype. They secrete cytokines and chemokines such as IL-10 and macrophage inflammatory protein 4 (MIP-4), thereby, promoting tumour growth [21]. However, many contradicting studies on the positive or negative impact of cytokines such as IL-1β or IL-10 show that the complex interplay of different cytokines and chemokines inside the TME is not yet fully understood [12].

A high number of TAMs in the TME are generally correlated with a poor patient survival prognostic [21]. The TAMs are responsible for a high immunosuppressing property and help the cancer to evade drug treatment [24, 25]. Therefore, novel cancer treatments are targeting the anti-inflammatory macrophages (M2) to improve patients' survival rate [25]. This is accomplished by preventing the recruitment of monocytes into the TME resulting in reduced numbers of M2 like TAMs [16]. A different approach is focused on reprogramming the M2-like TAMs towards the more anti-tumoural phenotype M1 [26]. Anti-cancer drugs such as paclitaxel and docetaxel impact the phenotype of macrophages and are of interest for combinatorial treatments [26]. Even though extensive research was conducted on TAMs in the TME, their role and especially the interaction with the TME remains largely unsolved and is in need for further investigations. The heterogeneous cell population within the TME requires the development of new technologies for single-cell analysis.

1.2 Immune assays for protein quantification

Proteins are essential for all living organism governing functions from proliferation over differentiation to cell-to-cell signaling. They are highly specialized macromolecules comprised out of thousands of amino acids designed to interact with other molecules or proteins. The complex interplay between proteins results in specific cellular phenotypes and control the cellular response to external stimuli. A slight alteration in protein concentrations can lead to diseases or dysfunctional cells. The sheer number of proteins in mammalian cells reach numbers as high as 10^9 and contain up to 10^4 different kinds of proteins [27]. Therefore, it is challenging but critical to be able to measure the protein concentrations with high sensitivity, selectivity, and specificity in a suspension [28]. There are different methods to quantify the protein concentration in a suspension [29, 30], but the method used in this thesis relies on the affinity binding between antibody and antigen and is described in more detail.

1.2.1 Antibody-antigen interactions

Antibodies are a specific type of proteins primarily known for their functionality in the immune system. They are employed to detect and identify pathogens with high selectivity and specificity. Antibodies, also known as immunoglobulins, exists in five configurations with immunoglobulin G (IgG) as the most prominent in bioanalytical applications [28]. The antigen binding site of an antibody is located on the ends of the Y-shaped proteins and is highly specific to certain antigens [31]. Depending on the antibody, an antigen can be fragment of a pathogen such as a virus or bacteria, but also a molecular sequence of a protein. The development of the *in vitro* production of antibodies binding to specific antigen enables the use of antibody-antigen interaction for the quantification of targeted proteins [28]. Several methods were developed to evaluate the concentration of proteins after binding to an antibody.

1.2.2 Sandwich immunoassay

In a sandwich immunoassay, proteins are sandwiched between two antibodies ideally binding to two different antigen sides of the protein [28]. The readout of the assay can rely on many diffrent methods such as an enzyme reaction, polymere chain reaction, radiometry, or fluorescence.

Briefly, the primary antibodies are bound mostly to a flat and defined surface such as the bottom of a microtiter plate well. During the incubation period with the protein solution to probe, proteins are binding to the stationary primary antibody. The second antibody and readout fluorophore are introduced into the system after thorough washing of the surface with the primary antibodies. Depending on the concentration of the protein in the investigated solution, a specific number of proteins are bound to the primary antibodies resulting in specific number of target antigens for the secondary antibody and the fluorophore. Characterization measurements directly link the intensity signal of the fluorophore to a known amount of proteins bound to the immune sandwich complex.

The enzyme-linked immunosorbent assay (ELISA) is a common assay used in biological laboratories and medical facilities. There are many variations of ELISA assays, but the core principle relies on an enzyme which is linked to an antibody [32–34]. If the target protein (antigen) is present in the solution, the enzyme catalyses a reagent which leads to a readout proportional to the amount of protein in the solution. The readout can be a colorimetric assay, but also fluorescence-based readouts were used to allow measuring of multiple proteins at the same time.

A special variant of an sandwich immunoassay is a relocation-based immunoassay [35]. At the start of the experiment, all reagents, namely secondary antibody and labelling fluorophore, are introduced into the system at the same time. If proteins are present in the solution or secreted during the incubation time, the secondary antibody and the readout fluorophore accumulate at the location of the primary antibody. This relocation of the readout fluorophore can be characterized resulting in a precise quantification of the protein concentration. The dynamic readout of this method is its greatest advantage; however, the increased background signal reduces the sensitivity, and, at higher concentrations, the Hook effect is detrimental for a precise readout [36].

1.2.3 Multiplexing with barcoded beads

Bead-based sandwich immunoassays are a subgroup of sandwich immunoassays [37]. The primary antibody is integrated in or bound on the surface of the bead. Multiple beads are used to establish the concentration of proteins in a solution and the average fluorescence signal of all beads is used to determine the protein concentration. Some manufacturers include iron oxide particles inside the polystyrene beads during the fabrication process resulting in magnetic beads [38]. This facilitates the washing between the different assay steps and prevents the loss of beads.

During the fabrication, different fluorophores can be integrated into the bead resulting in a precise fluorescence signal of the bead. A combination of different signal strengths with different fluorophores can be used as a unique identifier for a bead type. This can be used to imprint a barcode to each bead type which identifies each bead from a population. Luminex®, a well-known manufacturing company of barcoded beads, fabricates beads with 100 different barcodes with only two fluorophores (Fig. 1.2) [39].

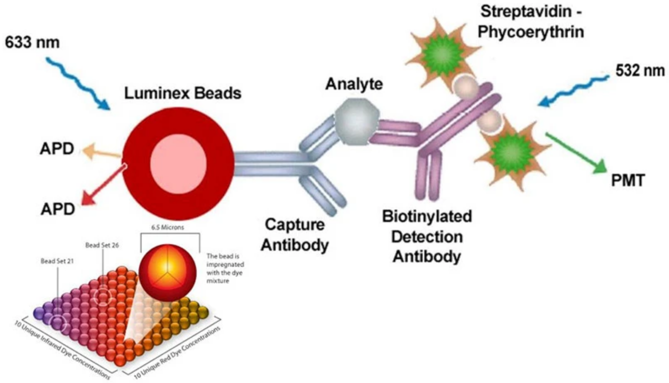

Figure 1.2: Luminex beads contain two fluorophores at defined concentrations resulting in a unique identifier for each bead. Up to 100 unique combinations, barcodes, can be distinguished. The barcode is correlated to the captured antibody, identifying the target protein of each bead. The concentration of the targeted protein is evaluated by a shared readout fluorophore connected with a detection antibody to the target protein. Reprinted from Adamcova et al. [40]

By coupling a barcode with a primary antibody targeting a specific protein, the fluorescent readout of the bead not only correlates with the protein concentration but also with the identity of the protein which is targeted by this bead. This is especially important, because the readout fluorophore does not need to differ between proteins. The number of different proteins measurable is then only limited by the number of barcodes imbedded into the beads. This enables multiplexed measurements, measuring multiple proteins at the same time, from one solution.

1.3 Analysis of secreted proteins at the single-cell level

The analysis of single cells is challenging due to their small size, frail structure, and the number of analysed cells needed to obtain statistically significant findings. Flow cytometry is one of the most used single-cell analysis method to date and is applied in most laboratories [41, 42]. It is a standard method to quantify the state of a population and measure cellular properties based on fluorescence readout. It is well suited to measure intra-cellular protein concentrations, or the abundance of membrane bound proteins. However, additional steps are needed to bind the secreted proteins on the surface of the cells enabling secretion detection in common flow cytometry [43, 44]. Therefore, it is ill-suited to quantify the secretion of cells due to complex and highly specialized assays. Preferably, an isolation and separation between each cell is desired to quantify the secretome of a single cell with a high specificity.

A well-established and widely used method to detect the secretion of single cells is an enzyme-linked immunosorbent spot (ELISpot) assay [45, 46]. Cells are spread across an antibody coated surface which captures the secreted protein in proximity of the cell during incubation. This approach allows easy and cost-effective analysis of secreted protein from single cells; however, the major limitation of the system includes that the proteins diffuse in all directions, reducing the specificity of the assay and guarantee only partial capture of the proteins [47].

1.4 Microfluidics as a tool for analysing secreted proteins from single cells

Microfluidics encompasses the field of fluids confined to micrometre-sized geometries to perform specific tasks with high throughput and minimal sample consumption. Even though the first microfluidic devices were developed already in 1975, the field gained traction in 1990 when Manz et al. introduced the concept of miniaturized total analysis systems (μTAS) [48]. The already existing microfabrication approaches were extended, and novel approaches enabled more complex and more accessible microfluidic devices [49]. Since its introduction, it was applied in fields such as analytical chemistry, cellular biology, and personalized medicine, and remains an important field of research to date [50, 51]. A current overview of the field with the focus on bioanalysis and diagnositc is found in chapter 2 of this thesis.

Microfluidic devices are well suited for handling biological samples due to the comparable size of the micro-scaled geometries and the sizes of living cells (~1-100 μm) [50, 51]. Several microfluidic methods were developed to overcome the limitations of ELISpot assays and enabled the isolation, incubation, and analysis of single cells over the recent years [47, 52–62]. Most of the micro-scaled devices have the advantage to isolate the cells in small volumes, resulting in an up concentration of secreted proteins. Therefore, already low secreting cells have the potential to increase the concentration in the volume above the limit of detection (LOD). The developed devices can roughly be grouped in four groups: droplet devices, utilizing two phases to separate cells; hydrogel particles functionalized to capture secreted proteins on their surface; microvalve devices enclosing cells in micro-scaled chambers; and microwell array devices isolating devices based on distance or sealing.

1.4.1 Droplet devices

Droplet-based devices employ two immiscible phases to separate cells from each other. The inner phase, containing the cells, nutrients, and assay reagents, is surrounded by the continuous phase consisting of fluorocarbon, silicon, or hydrocarbon oil [63]. The low solubility of proteins in the continuous phase essentially ensures that the proteins secreted by the cells are contained in each droplet. The gas permeability and the biocompatibility of oil is critical for cell survival but oils such as FC-40, or HFE-7500 are well known to provide the needed properties [64]. The microfluidic devices are designed to generate droplets at high frequency encapsulating single cells inside the droplets. The most common readout methods of the droplet-based assays are fluorescence [35, 65] or Förster resonance energy transfer (FRET) [66, 67] due to the closed system.

Many platforms rely on a relocation immunoassay as a protein detection and quantification readout [35, 52, 53, 65, 68–70]. The method was first applied by Konry et al. [35] to measure the secretion of IL-10 from single cells. They co-encapsulated a cell, a functionalized microsphere coated with the target primary antibody, and all needed reagents for a sandwich immunoassay inside the droplet during its generation. The secreted proteins are captured, and antibody-fluorophore complexes relocate to the beads surface. The ratio between the fluorescence intensity on the bead and the background gives a quantitative readout of the protein concentration. Similar principles were used to screen for antibody secreting cells [65, 69] or was applied to dynamically monitor single immune cells [52, 53]. In the DropMap platform, single cells are co-captured with nanosized magnetic beads functionalized with primary antibodies (Fig. 1.3). The platform provides temporal readout of the protein secretion at high throughput and resolution. Portmann et al. multiplexed the DropMap platform and measured three proteins with three different fluorophores [68].

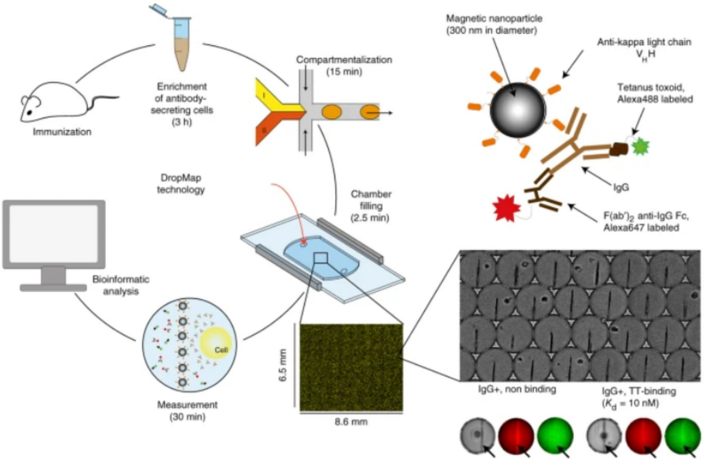

Figure 1.3: DropMap platform. Single cells are isolated in droplets and the secreted proteins are measured with a relocation sandwich immunoassay. Reprinted from Eyer et al. [52]

In general, the main challenge of droplet microfluidics is the implementation of a facil and reliable approach to exchange reagents inside the droplets, limiting the washing capabilities needed for many assays significantly [71]. This leads to less sensitive measurements and, at higher concentration, to the Hook effect [36]. Furthermore, the multiplex capabilities are generally limited by the number of fluorophores measurable without crosstalk.

1.4.2 Hydrogel devices

Several research groups utilized form-stable hydrogel particles for the detection or quantification of secreted proteins from single cells. Generally, the hydrogel particles are generated in a two-phase system resulting in a uniform population of hydrogel particles. After generation of the hydrogel particles, they can be demulsified from the oil, washed, and used in common flow cytometers.

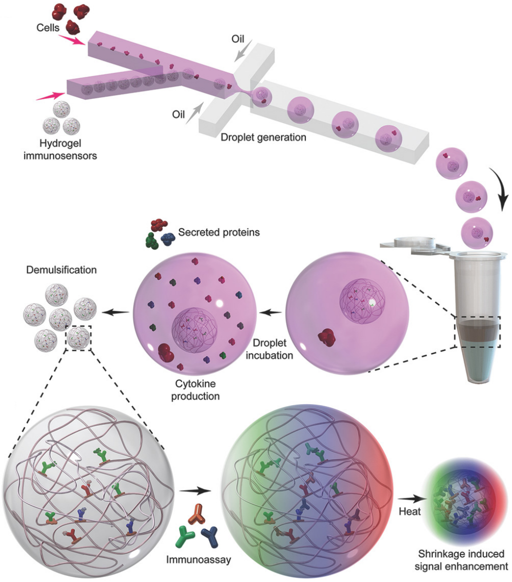

Figure 1.4: Platform employing hydrogel particles to quantify the secretion of single cells multiplexed from 3 proteins. Reprinted from Hsu et al. [72]

Chokkalingam et al. [73] co-encapsulated functionalized beads with single cells in hydrogel droplets. The secreted proteins are contained in the droplets and are captured by the antibodies on the beads surface. After incubation, the droplets are broken (demulsified), and the standard sandwich immunoassay is conducted. This method allows to combine the high throughput of droplet microfluidics with the flexibility of washing and reagents exchange. It was further developed to enable the multiplexed measurement of up to three proteins (Fig. 1.4) [72].

Recently, a novel technology was proposed where 3D structured hydrogel were used to capture and analyse secreted protein from single cells [74, 75]. Open cavities inside the structured hydrogels have cell-adhesive properties capturing single cells in these so called nanovials (Fig. 1.5). The hydrogel particles with the cells can be encapsulated in droplets isolating the secreting cells and preventing cross-contamination. The proteins are captured on the surface of the hydrogel particle before the particle is demulsified after incubation. This enables the use of a standard sandwich immunoassay with washing steps.

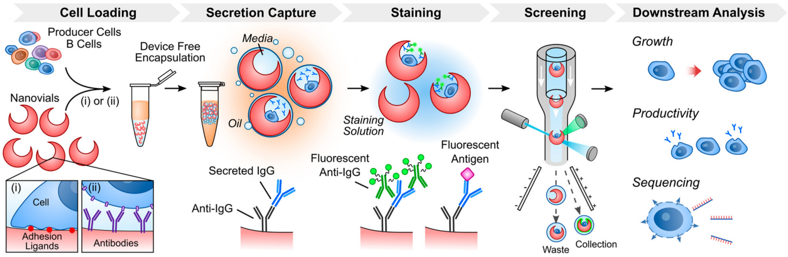

Figure 1.5: Structured hydrogel particles are utilized to capture single cells in nanovials and measure the secreted proteins on the surface with a sandwich immunoassay. Reprinted from Hsu et al. [74]

1.4.3 Microvalve devices

In microvalve devices the cells are captured and actively separated from neighbouring cells by sophisticated pneumatic valves. The cells are enclosed in pico- to nanolitre sized chambers preventing the diffusion of proteins to neighbouring cells. Several capturing principles were introduced to achieve single cell capture such as hydrodynamic traps or size-based capturing [54, 55, 76–78]. The capture efficiency in devices is generally good enabling the single-cell studies of rare samples such as circulating tumour cells. Additionally, the complexity of the system allows the easy and fast reagent exchange. This enables the use of highly sensitive bioassays to detect and quantify the secretome of cells. Typically, the readout is based on a sandwich immunoassay, but other readouts were implemented as well [79].

Recently, a versatile platform based on microvalves was developed which utilized commercially available beads to quantify proteins at the single-cell level [54] (Fig. 1.6). The platform consists of 1026 wells with a well density of 11 microchambers per square millimetre. The cells were labelled with magnetic beads and co-capture with barcoded magnetic beads. Pneumatic valves isolated each cell preventing cross contamination. The barcoded beads are commercially offered with more than 300 tested and characterized protein assays resulting in a versatile and easy to adapt platform.

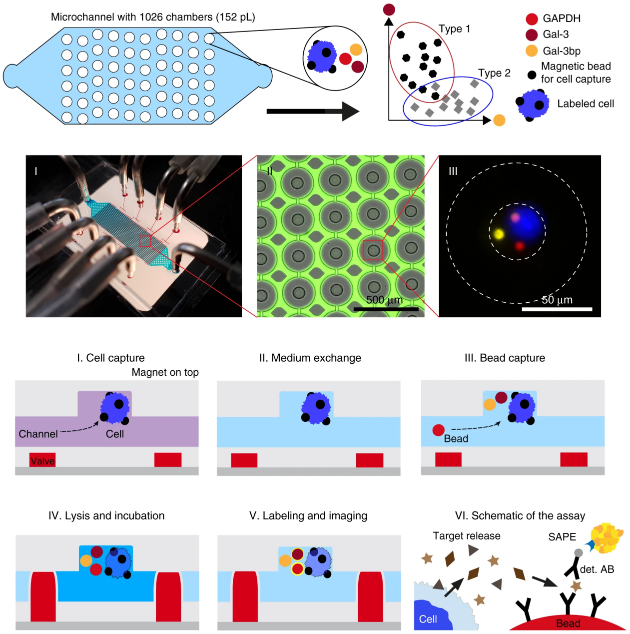

Figure 1.6: Microvalve based platform for single-cell anaylsis. Single cells are co-captured with magnetic beads and the secreted proteins are measured based on an on-bead sandwich immunoassay. Reprinted from Armbrecht et al. [54]

The main limitation in microvalve-based devices is the inadequate throughput due to the complex mechanism usually needed to achieve the desired functionalities. Additionally, the complexity of the system necessitates well-trained users preventing a widespread application of the devices and commercialization.

1.4.4 Microwell devices

Microwell array devices are known for their high-throughput and easy-to-use properties. The cells are introduced in bulk and sediment into micro-sized wells. One can distinguish two major device types: open microwell arrays and closed microwell arrays.

Closed microwell devices

Microwells in closed systems are usually sealed by a glass slide clamped on top of the device [56, 58, 61, 76, 80–82]. Here, the antibodies are micropatterned on the glass slide instead of the microwells.

Lu et al. patterned a glass slide with 42 different primary antibodies enabling the multiplexed measurement of 42 immune effector proteins from single cells in closed microwells [61] (Fig. 1.6). Single cells were captured in microwells fabricated in PDMS and sealed with the functionalized glass slide. The platform contained 5044 microwells leading to a well density of around 3 wells per square millimetre.

Open microwell devices

In open systems, a similar principle as in the ELISpot assay is applied [47, 57, 59, 83, 84]. The microwells or beads inside the microwells are coated with antibody capturing the target proteins secreted by the cell in the well.

Choi et al. developed an open microwell platform integrated into a 384-wells plate [47]. With laser micropatterning, they reached a well density inside the 384-well plate of around 30 wells per square millimetre. The proteins secreted by the cells were captured and evaluated based on a sandwich immunoassay. However, to prevent cross contamination between wells, they added methylcellulose to the media, increasing the viscosity and thereby reducing diffusion.

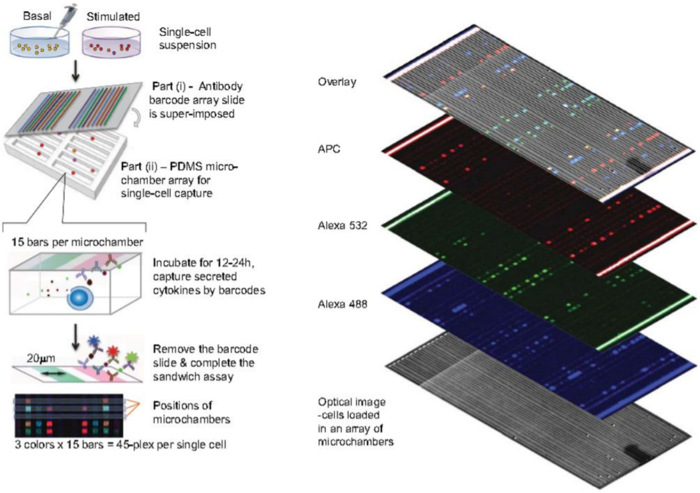

Figure 1.7: Microwell array based platform for single-cell anaylsis. Single cells are captured in microwells patterned with 42 regions of different antibodies. The secreted proteins are measured with a sandwich immunoassay. Reprinted frum Lu et al. [61]

Depending on the principle, the limitation of microwell-based devices differ. In open systems, in general, diffusion between the wells reduces the sensitivity, selectivity, and the up-concentration of proteins in a confined volume. In closed systems, on the other hand, it is challenging to seal and isolate the microwells without leakage preventing cross-contamination.

1.4.5 Unmet needs

In the recent years, several new technologies were developed allowing the analysis of the whole-genome transcriptome of single cells [85, 86]. These methods utilize sequencing as a readout and implemented unique molecular identifiers (UMI) allowing the detection of more than 10^3 to 10^4 genes from each cell while providing a throughput of more than 10^4 cells. The technologies were further developed to be able to detect up to 82 membrane-bound proteins from the cells by tagging DNA labelled antibodies to the surface of the cells [87, 88]. However, the quantification of secreted proteins at the single-cell level is still a challenge, as the secreted proteins cannot be clearly and easily assigned towards each cell. The microfluidic methods presented in this chapter are still lacking the high dimensional multiplexing in combination with the throughput achieved for single-cell transcriptome analysis.

1.5 Goal of this thesis

The aim of this work is to develop microfluidic devices for the multiplexed quantification of secreted proteins at the single-cell level at high throughput. The developed devices were used to study the secretion profiles of individual macrophages in response to different stimuli modelling the influence of the TME on them.

In chapter 2, the latest progresses in the microfluidic field with the focus on bioanalysis and diagnostics are summarized. The review highlights new materials and methods employed (section 2.2), summarizes current integrated operational units (section 2.3), recaps recent developments of detection methods (section 2.4), and concludes with innovative application in the field (section 2.5).

Chapter 3 presents a microfluidic system for the analysis of up to 1084 single cells employing the combination of hydrodynamic traps, pneumatic valves, and barcoded magnetic beads to enable multiplexed quantification of secreted proteins. We showed that the platform can reliably quantify protein concentrations below 1250 molecules per chamber enabling the characterization of single macrophage polarization states. In section 3.2, the experimental setup and methods are described in detail whereas in section 3.3 the results obtained with the developed design are presented and discussed.

In chapter 4, we describe the development of a microfluidic platform able to isolate and analyse the secretome of up to 100’992 single cells. The combination of an open hexagonal microwell array with a two-phase system overcomes previous limitation enabling an unequalled well density. The high well density results in high throughput which we utilized to study the heterogeneity of macrophages and the impact of anti-cancer drugs on them. In section 4.2, the developed device is characterized, and the results obtained are discussed. In section 4.4, the experimental methods are presented and reviewed in detail.

Chapter 5 summarizes and concludes this thesis. The developed platforms are critically discussed and we give suggestions for further improvements and optimizations.

1.6 References

[1] H. Sung, J. Ferlay, R. L. Siegel, M. Laversanne, I. Soerjomataram, A. Jemal, and F. Bray, «Global cancer statistics 2020: globocan estimates of incidence and mortality worldwide for 36 cancers in 185 countries», CA: A Cancer Journal for Clinicians **71**, 209–249 (2021).

[2] D. B. Johnson, C. A. Nebhan, J. J. Moslehi, and J. M. Balko, «Immune-checkpoint inhibitors: long-term implications of toxicity», Nature Reviews Clinical Oncology **19**, 254–267 (2022).

[3] R. C. Sterner and R. M. Sterner, «Car-t cell therapy: current limitations and potential strategies», Blood Cancer Journal **11**, 69 (2021).

[4] T. Wen, J. Wang, Y. Shi, H. Qian, and P. Liu, «Inhibitors targeting bruton's tyrosine kinase in cancers: drug development advances», Leukemia **35**, 312–332 (2021).

[5] M.-Z. Jin and W.-L. Jin, «The updated landscape of tumor microenvironment and drug repurposing», Signal Transduction and Targeted Therapy **5**, 166 (2020).

[6] D. Entenberg, M. H. Oktay, and J. S. Condeelis, «Intravital imaging to study cancer progression and metastasis», Nature Reviews Cancer **23**, 25–42 (2023).

[7] N. M. Anderson and M. C. Simon, «The tumor microenvironment», Current Biology **30**, R921–R925 (2020).

[8] M. R. Junttila and F. J. de Sauvage, «Influence of tumour microenvironment heterogeneity on therapeutic response», Nature **501**, 346–354 (2013).

[9] R. Ge, Z. Wang, and L. Cheng, npj Precision Oncology **6**, 31 (2022).

[10] Q. Hao, J. V. Vadgama, and P. Wang, «Ccl2/ccr2 signaling in cancer pathogenesis», Cell Communication and Signaling **18**, 82 (2020).

[11] K. Fousek, L. A. Horn, and C. Palena, «Interleukin-8: a chemokine at the intersection of cancer plasticity, angiogenesis, and immune suppression», Pharmacology and Therapeutics **219**, 107692 (2021).

[12] D. Briukhovetska, J. Dörr, S. Endres, P. Libby, C. A. Dinarello, and S. Kobold, «Interleukins in cancer: from biology to therapy», Nature Reviews Cancer **21**, 481–499 (2021).

[13] F. R. Greten and S. I. Grivennikov, «Inflammation and cancer: triggers, mechanisms, and consequences», Immunity **51**, 27–41 (2019).

[14] M. Binnewies, E. W. Roberts, K. Kersten, V. Chan, D. F. Fearon, M. Merad, L. M. Coussens, D. I. Gabrilovich, S. Ostrand-Rosenberg, C. C. Hedrick, R. H. Vonderheide, M. J. Pittet, R. K. Jain, W. Zou, T. K. Howcroft, E. C. Woodhouse, R. A. Weinberg, and M. F. Krummel, «Understanding the tumor immune microenvironment (time) for effective therapy», Nature Medicine **24**, 541–550 (2018).

[15] B.-Z. Qian, J. Li, H. Zhang, T. Kitamura, J. Zhang, L. R. Campion, E. A. Kaiser, L. A. Snyder, and J. W. Pollard, «Ccl2 recruits inflammatory monocytes to facilitate breast-tumour metastasis», Nature **475**, 222–225 (2011).

[16] A. Mantovani, P. Allavena, F. Marchesi, and C. Garlanda, «Macrophages as tools and targets in cancer therapy», Nature Reviews Drug Discovery **21**, 799–820 (2022).

[17] M. Locati, G. Curtale, and A. Mantovani, «Diversity, mechanisms, and significance of macrophage plasticity», Annual Review of Pathology: Mechanisms of Disease **15**, 123–147 (2020).

[18] M. Najafi, N. H. Goradel, B. Farhood, E. Salehi, M. S. Nashtaei, N. Khanlarkhani, Z. Khezri, J. Majidpoor, M. Abouzaripour, M. Habibi, I. R. Kashani, and K. Mortezaee, «Macrophage polarity in cancer: a review», Journal of Cellular Biochemistry **120**, 2756–2765 (2019).

[19] P. J. Murray, «Macrophage polarization», Annual Review of Physiology **79**, 541–566 (2017).

[20] P. J. Murray, J. E. Allen, S. K. Biswas, E. A. Fisher, D. W. Gilroy, S. Goerdt, S. Gordon, J. A. Hamilton, L. B. Ivashkiv, T. Lawrence, M. Locati, A. Mantovani, F. O. Martinez, J.-L. Mege, D. M. Mosser, G. Natoli, J. P. Saeij, J. L. Schultze, K. A. Shirey, A. Sica, J. Suttles, I. Udalova, J. A. van Ginderachter, S. N. Vogel, and T. A. Wynn, «Macrophage activation and polarization: nomenclature and experimental guidelines», Immunity **41**, 14–20 (2014).

[21] G. Solinas, G. Germano, A. Mantovani, and P. Allavena, «Tumor-associated macrophages (tam) as major players of the cancer-related inflammation», Journal of Leukocyte Biology **86**, 1065–1073 (2009).

[22] M. J. Pittet, O. Michielin, and D. Migliorini, «Clinical relevance of tumour-associated macrophages», Nature Reviews Clinical Oncology **19**, 402–421 (2022).

[23] L. Cassetta and J. W. Pollard, «A timeline of tumour-associated macrophage biology», Nature Reviews Cancer **23**, 238–257 (2023).

[24] L. Zitvogel, L. Galluzzi, M. J. Smyth, and G. Kroemer, «Mechanism of action of conventional and targeted anticancer therapies: reinstating immunosurveillance», Immunity **39**, 74–88 (2013).

[25] M. D. Palma, S. Nassiri, and C. Cianciaruso, «Macrophage interference on chemotherapy», Nature Cell Biology **21**, 411–412 (2019).

[26] C. W. Wanderley, D. F. Colón, J. P. M. Luiz, F. F. Oliveira, P. R. Viacava, C. A. Leite, J. A. Pereira, C. M. Silva, C. R. Silva, R. L. Silva, C. A. Speck-Hernandez, J. M. Mota, J. C. Alves-Filho, R. C. Lima-Junior, T. M. Cunha, and F. Q. Cunha, «Paclitaxel reduces tumor growth by reprogramming tumor-associated macrophages to an m1 profile in a tlr4-dependent manner», Cancer Research **78**, 5891–5900 (2018).

[27] A. Schmid, H. Kortmann, P. S. Dittrich, and L. M. Blank, «Chemical and biological single cell analysis», Current Opinion in Biotechnology **21**, 12–20 (2010).

[28] L. Cohen and D. R. Walt, «Highly sensitive and multiplexed protein measurements», Chemical Reviews **119**, 293–321 (2019).

[29] J. R. Yates, C. I. Ruse, and A. Nakorchevsky, «Proteomics by mass spectrometry: approaches, advances, and applications», Annual Review of Biomedical Engineering **11**, 49–79 (2009).

[30] J. E. Noble and M. J. Bailey, «Quantitation of protein», in *Methods in enzymology*, Vol. 463 (Academic Press Inc., 2009) Chap. 8, pp. 73–95.

[31] X. Yu, Y.-P. Yang, E. Dikici, S. K. Deo, and S. Daunert, «Beyond antibodies as binding partners: the role of antibody mimetics in bioanalysis», Annual Review of Analytical Chemistry **10**, 293–320 (2017).

[32] E. Engvall and P. Perlmann, «Enzyme-linked immunosorbent assay (elisa) quantitative assay of immunoglobulin g», Immunochemistry **8**, 871–874 (1971).

[33] A. A. Hariri, S. S. Newman, S. Tan, D. Mamerow, A. M. Adams, N. Maganzini, B. L. Zhong, M. Eisenstein, A. R. Dunn, and H. T. Soh, «Improved immunoassay sensitivity and specificity using single-molecule colocalization», Nature Communications **13**, 5359 (2022).

[34] S. Braesch-Andersen, S. Paulie, C. Smedman, S. Mia, and M. Kumagai-Braesch, «Apoe production in human monocytes and its regulation by inflammatory cytokines», PLoS ONE **8**, e79908 (2013).

[35] T. Konry, M. Dominguez-Villar, C. Baecher-Allan, D. A. Hafler, and M. Yarmush, «Droplet-based microfluidic platforms for single t cell secretion analysis of il-10 cytokine», Biosensors and Bioelectronics **26**, 2707–2710 (2011).

[36] J. F. Jacobs, R. G. van der Molen, X. Bossuyt, and J. Damoiseaux, «Antigen excess in modern immunoassays: to anticipate on the unexpected», Autoimmunity Reviews **14**, 160–167 (2015).

[37] K. L. Kellar and M. A. Iannone, «Multiplexed microsphere-based flow cytometric assays», Experimental Hematology **30**, 1227–1237 (2002).

[38] B.-I. Haukanes and C. Kvam, «Application of magnetic beads in bioassays», Nature Biotechnology **11**, 60–63 (1993).

[39] H. Graham, D. J. Chandler, and S. A. Dunbar, «The genesis and evolution of bead-based multiplexing», Methods **158**, 2–11 (2019).

[40] M. Adamcova and F. Simko, «Multiplex biomarker approach to cardiovascular diseases», Acta Pharmacologica Sinica **39**, 1068–1072 (2018).

[41] W. A. Bonner, H. R. Hulett, R. G. Sweet, and L. A. Herzenberg, «Fluorescence activated cell sorting», Review of Scientific Instruments **43**, 404–409 (1972).

[42] S. P. Perfetto, P. K. Chattopadhyay, and M. Roederer, «Seventeen-colour flow cytometry: unravelling the immune system», Nature Reviews Immunology **4**, 648–655 (2004).

[43] R. Manz, M. Assenmacher, E. Pflüger, S. Miltenyi, and A. Radbruch, «Analysis and sorting of live cells according to secreted molecules, relocated to a cell-surface affinity matrix.», Proceedings of the National Academy of Sciences **92**, 1921–1925 (1995).

[44] G. Liu, C. Bursill, S. P. Cartland, A. G. Anwer, L. M. Parker, K. Zhang, S. Feng, M. He, D. W. Inglis, M. M. Kavurma, M. R. Hutchinson, and E. M. Goldys, «A nanoparticle-based affinity sensor that identifies and selects highly cytokine-secreting cells», iScience **20**, 137–147 (2019).

[45] G. Porebski, K. Piotrowicz-Wojcik, and R. Spiewak, «Elispot assay as a diagnostic tool in drug hypersensitivity reactions», Journal of Immunological Methods **495**, 113062 (2021).

[46] C. C. Czerkinsky, L.-A. Nilsson, H. Nygren, O. Ouchterlony, and A. Tarkowski, «A solid-phase enzyme-linked immunospot (elispot) assay for enumeration of specific antibody-secreting cells», Journal of Immunological Methods **65**, 109–121 (1983).

[47] J. R. Choi, J. H. Lee, A. Xu, K. Matthews, S. Xie, S. P. Duffy, and H. Ma, «Monolithic hydrogel nanowells-in-microwells enabling simultaneous single cell secretion and phenotype analysis», Lab on a Chip **20**, 4539–4551 (2020).

[48] A. Manz, N. Graber, and H. Widmer, «Miniaturized total chemical analysis systems: a novel concept for chemical sensing», Sensors and Actuators B: Chemical **1**, 244–248 (1990).

[49] D. C. Duffy, J. C. McDonald, O. J. A. Schueller, and G. M. Whitesides, «Rapid prototyping of microfluidic systems in poly(dimethylsiloxane)», Analytical Chemistry **70**, 4974–4984 (1998).

[50] P. S. Dittrich and A. Manz, «Lab-on-a-chip: microfluidics in drug discovery», Nature Reviews Drug Discovery **5**, 210–218 (2006).

[51] L. Armbrecht and P. S. Dittrich, «Recent advances in the analysis of single cells», Analytical Chemistry **89**, 2–21 (2017).

[52] K. Eyer, R. C. Doineau, C. E. Castrillon, L. Briseño-Roa, V. Menrath, G. Mottet, P. England, A. Godina, E. Brient-Litzler, C. Nizak, A. Jensen, A. D. Griffiths, J. Bibette, P. Bruhns, and J. Baudry, «Single-cell deep phenotyping of igg-secreting cells for high-resolution immune monitoring», Nature Biotechnology **35**, 977–982 (2017).

[53] Y. Bounab, K. Eyer, S. Dixneuf, M. Rybczynska, C. Chauvel, M. Mistretta, T. Tran, N. Aymerich, G. Chenon, J. F. Llitjos, F. Venet, G. Monneret, I. A. Gillespie, P. Cortez, V. Moucadel, A. Pachot, A. Troesch, P. Leissner, J. Textoris, J. Bibette, C. Guyard, J. Baudry, A. D. Griffiths, and C. Védrine, «Dynamic single-cell phenotyping of immune cells using the microfluidic platform dropmap», Nature Protocols **15**, 2920–2955 (2020).

[54] L. Armbrecht, R. S. Müller, J. Nikoloff, and P. S. Dittrich, «Single-cell protein profiling in microchambers with barcoded beads», Microsystems and Nanoengineering **5**, 55 (2019).

[55] L. Armbrecht, O. Rutschmann, B. M. Szczerba, J. Nikoloff, N. Aceto, and P. S. Dittrich, «Quantification of protein secretion from circulating tumor cells in microfluidic chambers», Advanced Science **7**, 1903237 (2020).

[56] M. Elitas, K. Brower, Y. Lu, J. J. Chen, and R. Fan, «A microchip platform for interrogating tumor-macrophage paracrine signaling at the single-cell level», Lab Chip **14**, 3582–3588 (2014).

[57] X. An, V. G. Sendra, I. Liadi, B. Ramesh, G. Romain, C. Haymaker, M. Martinez-Paniagua, Y. Lu, L. G. Radvanyi, B. Roysam, and N. Varadarajan, «Single-cell profiling of dynamic cytokine secretion

and the phenotype of immune cells», PLOS ONE **12**, e0181904 (2017).

[58] Y. Lu, J. J. Chen, L. Mu, Q. Xue, Y. Wu, P.-H. Wu, J. Li, A. O. Vortmeyer, K. Miller-Jensen, D. Wirtz, and R. Fan, «High-throughput secretomic analysis of single cells to assess functional cellular heterogeneity», Analytical Chemistry **85**, 2548–2556 (2013).

[59] Y. Zhou, N. Shao, R. B. de Castro, P. Zhang, Y. Ma, X. Liu, F. Huang, R.-F. Wang, and L. Qin, «Evaluation of single-cell cytokine secretion and cell-cell interactions with a hierarchical loading microwell chip», Cell Reports **31**, 107574 (2020).

[60] M. Dhar, J. N. Lam, T. Walser, S. M. Dubinett, M. B. Rettig, and D. D. Carlo, «Functional profiling of circulating tumor cells with an integrated vortex capture and single-cell protease activity assay», Proceedings of the National Academy of Sciences **115**, 9986–9991 (2018).

[61] Y. Lu, Q. Xue, M. R. Eisele, E. S. Sulistijo, K. Brower, L. Han, E.-a. D. Amir, D. Pe'er, K. Miller-Jensen, and R. Fan, «Highly multiplexed profiling of single-cell effector functions reveals deep functional heterogeneity in response to pathogenic ligands», Proceedings of the National Academy of Sciences **112**, E607–E615 (2015).

[62] R. Fan, O. Vermesh, A. Srivastava, B. K. H. Yen, L. Qin, H. Ahmad, G. A. Kwong, C.-C. Liu, J. Gould, L. Hood, and J. R. Heath, «Integrated barcode chips for rapid, multiplexed analysis of proteins in microliter quantities of blood», Nature Biotechnology **26**, 1373–1378 (2008).

[63] T. Moragues, D. Arguijo, T. Beneyton, C. Modavi, K. Simutis, A. R. Abate, J.-C. Baret, A. J. deMello, D. Densmore, and A. D. Griffiths, «Droplet-based microfluidics», Nature Reviews Methods Primers **3**, 32 (2023).

[64] K. C. Lowe, «Perfluorochemical respiratory gas carriers: benefits to cell culture systems», Journal of Fluorine Chemistry **118**, 19–26 (2002).

[65] L. Mazutis, J. Gilbert, W. L. Ung, D. A. Weitz, A. D. Griffiths, and J. A. Heyman, «Single-cell analysis and sorting using droplet-based microfluidics», Nature Protocols **8**, 870–891 (2013).

[66] B. E. Debs, R. Utharala, I. V. Balyasnikova, A. D. Griffiths, and C. A. Merten, «Functional single-cell hybridoma screening using droplet-based microfluidics», Proceedings of the National Academy of Sciences **109**, 11570–11575 (2012).

[67] J. Rutkauskaite, S. Berger, S. Stavrakis, O. Dressler, J. Heyman, X. C. i Solvas, A. deMello, and L. Mazutis, «High-throughput single-cell antibody secretion quantification and enrichment using droplet microfluidics-based fret assay», iScience **25**, 104515 (2022).

[68] K. Portmann, A. Linder, N. Oelgarth, and K. Eyer, «Single-cell deep phenotyping of cytokine release unmasks stimulation-specific biological signatures and distinct secretion dynamics», Cell Reports Methods **3**, 100502 (2023).

[69] A. Gérard, A. Woolfe, G. Mottet, M. Reichen, C. Castrillon, V. Menrath, S. Ellouze, A. Poitou, R. Doineau, L. Briseno-Roa, P. Canales-Herrerias, P. Mary, G. Rose, C. Ortega, M. Delincé, S. Essono, B. Jia, B. Iannascoli, O. R.-L. Goff, R. Kumar, S. N. Stewart, Y. Pousse, B. Shen, K. Grosselin, B. Saudemont, A. Sautel-Caillé, A. Godina, S. McNamara, K. Eyer, G. A. Millot, J. Baudry, P. England, C. Nizak, A. Jensen, A. D. Griffiths, P. Bruhns, and C. Brenan, «High-throughput single-cell activity-based screening and sequencing of antibodies using droplet microfluidics», Nature Biotechnology **38**, 715–721 (2020).

[70] R. Dimatteo and D. D. Carlo, «Il-2 secretion-based sorting of single t cells using high-throughput microfluidic on-cell cytokine capture», Lab on a Chip **22**, 1576–1583 (2022).

[71] D. J. Sukovich, S. C. Kim, N. Ahmed, and A. R. Abate, «Bulk double emulsification for flow cytometric analysis of microfluidic droplets», The Analyst **142**, 4618–4622 (2017).

[72] M. N. Hsu, S.-C. Wei, S. Guo, D.-T. Phan, Y. Zhang, and C.-H. Chen, «Smart hydrogel microfluidics for single-cell multiplexed secretomic analysis with high sensitivity», Small **14**, 1802918 (2018).

[73] V. Chokkalingam, J. Tel, F. Wimmers, X. Liu, S. Semenov, J. Thiele, C. G. Figdor, and W. T. S. Huck, «Probing cellular heterogeneity in cytokine-secreting immune cells using droplet-based microfluidics», Lab on a Chip **13**, 4740 (2013).

[74] J. de Rutte, R. Dimatteo, M. M. Archang, M. van Zee, D. Koo, S. Lee, A. C. Sharrow, P. J. Krohl, M. Mellody, S. Zhu, J. V. Eichenbaum, M. Kizerwetter, S. Udani, K. Ha, R. C. Willson, A. L. Bertozzi, J. B. Spangler, R. Damoiseaux, and D. D. Carlo, «Suspendable hydrogel nanovials for massively parallel single-cell functional analysis and sorting», ACS Nano **16**, 7242–7257 (2022).

[75] S. Lee, J. de Rutte, R. Dimatteo, D. Koo, and D. D. Carlo, «Scalable fabrication and use of 3d structured microparticles spatially functionalized with biomolecules», ACS Nano **16**, 38–49 (2022).

[76] C. Ma, R. Fan, H. Ahmad, Q. Shi, B. Comin-Anduix, T. Chodon, R. C. Koya, C.-C. Liu, G. A. Kwong, C. G. Radu, A. Ribas, and J. R. Heath, «A clinical microchip for evaluation of single immune cells reveals high functional heterogeneity in phenotypically similar t cells», Nature Medicine **17**, 738–743 (2011).

[77] K. Eyer, S. Stratz, P. Kuhn, S. K. Küster, and P. S. Dittrich, «Implementing enzyme-linked immunosorbent assays on a microfluidic chip to quantify intracellular molecules in single cells», Analytical Chemistry **85**, 3280–3287 (2013).

[78] M. Junkin, A. J. Kaestli, Z. Cheng, C. Jordi, C. Albayrak, A. Hoffmann, and S. Tay, «High-content quantification of single-cell immune dynamics», Cell Reports **15**, 411–422 (2016).

[79] X. Li, M. Soler, C. Szydzik, K. Khoshmanesh, J. Schmidt, G. Coukos, A. Mitchell, and H. Altug, «Label-free optofluidic nanobiosensor enables real-time analysis of single-cell cytokine secretion», Small **14**, 1800698 (2018).

[80] J. C. Love, J. L. Ronan, G. M. Grotenbreg, A. G. van der Veen, and H. L. Ploegh, «A microengraving method for rapid selection of single cells producing antigen-specific antibodies», Nature Biotechnology **24**, 703–707 (2006).

[81] C. M. Story, E. Papa, C.-C. A. Hu, J. L. Ronan, K. Herlihy, H. L. Ploegh, and J. C. Love, «Profiling antibody responses by multiparametric analysis of primary b cells», Proceedings of the National Academy of Sciences **105**, 17902–17907 (2008).

[82] Q. Han, N. Bagheri, E. M. Bradshaw, D. A. Hafler, D. A. Lauffenburger, and J. C. Love, «Polyfunctional responses by human t cells result from sequential release of cytokines», Proceedings of the National Academy of Sciences **109**, 1607–1612 (2012).

[83] A. J. Torres, A. S. Hill, and J. C. Love, «Nanowell-based immunoassays for measuring single-cell secretion: characterization of transport and surface binding», Analytical Chemistry **86**, 11562–11569 (2014).

[84] G. Romain, V. Senyukov, N. Rey-Villamizar, A. Merouane, W. Kelton, I. Liadi, A. Mahendra, W. Charab, G. Georgiou, B. Roysam, D. A. Lee, and N. Varadarajan, «Antibody fc engineering improves frequency and promotes kinetic boosting of serial killing mediated by nk cells», Blood **124**, 3241–3249 (2014).

[85] A. M. Klein, L. Mazutis, I. Akartuna, N. Tallapragada, A. Veres, V. Li, L. Peshkin, D. A. Weitz, and M. W. Kirschner, «Droplet barcoding for single-cell transcriptomics applied to embryonic stem cells», Cell **161**, 1187–1201 (2015).

[86] E. Z. Macosko, A. Basu, R. Satija, J. Nemesh, K. Shekhar, M. Goldman, I. Tirosh, A. R. Bialas, N. Kamitaki, E. M. Martersteck, J. J. Trombetta, D. A. Weitz, J. R. Sanes, A. K. Shalek, A. Regev, and S. A. McCarroll, «Highly parallel genome-wide expression profiling of individual cells using nanoliter droplets», Cell **161**, 1202–1214 (2015).

[87] M. Stoeckius, C. Hafemeister, W. Stephenson, B. Houck-Loomis, P. K. Chattopadhyay, H. Swerdlow, R. Satija, and P. Smibert, «Simultaneous epitope and transcriptome measurement in single cells», Nature Methods **14**, 865–868 (2017).

[88] V. M. Peterson, K. X. Zhang, N. Kumar, J. Wong, L. Li, D. C. Wilson, R. Moore, T. K. McClanahan, S. Sadekova, and J. A. Klappenbach,

«Multiplexed quantification of proteins and transcripts in single cells», Nature Biotechnology **35**, 936–939 (2017).

Chapter 2

Recent advances in microfluidic technology for bioanalysis and diagnostics

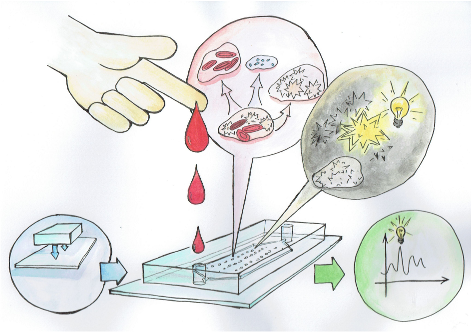

Authors: **Simon F. Berlanda**
Maximilian Breitfeld
Claudius L. Dietsche
Petra S. Dittrich
Journal: *Analytical Chemistry*
doi: 10.1021/acs.analchem.0c04366
Published: 10 November 2020

Reprinted with permission from S. F. Berlanda, M. Breitfeld, C. L. Dietsche, and P. S. Dittrich, «Recent advances in microfluidic technology for bioanalysis and diagnostics», Analytical Chemistry **93**, 311–331 (2021). Copyright 2021 American Chemical Society.

Recent Advances in Microfluidic Technology for Bioanalysis and Diagnostics

Simon F. Berlanda[1,†], Maximlian Breitfeld[1,†], Claudius L. Dietsche[1,†], and Petra S. Dittrich[1,*]

[1]Department of Biosystems Science and Engineering, Mattenstrasse 26, 4125 Basel, Switzerland
[†]S.F.B., M.B., and C.L.D. shared first authorship.
[*]petra.dittrich@bsse.ethz.ch

2.1 Introduction

Microfluidics has become a mature technology, providing an excellent toolbox for the handling and manipulation of fluid samples, suspended cells, and particles. About 30 years ago, the first microfluidic devices aimed mainly at miniaturizing analytical methods, particularly for improving the separation of analytes. Since then, fabrication protocols and operation of the devices have become more and more facile. The improved accessibility allowed increasing numbers of researchers to design, manufacture, and use microfluidic systems, which rapidly revealed the potential for widespread applications across the life sciences. Numerous novel microfluidic methods are reported every year for observation and manipulation of cells, mimicking organs, detection of biomarkers, and many other fields of study.

Microfluidic technology has multiple benefits for bioanalytical procedures. Obviously, the miniaturized devices facilitate processing and analyzing of small sample volumes, in the range of μL to pL. Correspondingly, the consumption of assay compounds is low, thereby reducing the cost of the analysis. In digital and droplet microfluidics, the sample is further segmented into droplets. In this way, thousands of discrete reaction compartments are created, which can be utilized for high-throughput screenings in the fields of drug discovery, drug testing, directed evolution, or single-cell analysis. Owing to the ease of use, droplet microfluidic platforms have been added to biologists' routine methods for single-cell sequencing, also referred to as droplet sequencing, which we do not further cover in this review.

Microfluidic devices made it possible to integrate different functional modules (or operational units) on a single platform and construct a micro total analysis system, as it was envisioned in the early days of microfluidics [1]. Excellent examples of integrated systems are reported for digital and droplet microfluidics, where several process steps were successfully realized on a single platform. Serial coupling of different separation methods before analysis, e.g., of cell suspensions, was likewise achieved.

The detection method is integral to the microfluidic platform to acquire a meaningful readout for the desired application. Microdevices can have either an integrated detection module or are coupled to an external instrument. While optical and fluorescence microscopy are commonly employed, interfaces to many other analytical methods were further advanced, opening multiple options for assays, with or without the need of (fluorescent) labels.

This review covers recent advances and developments in the field of microfluidic technology and selected articles published between August 2018 and September 2020. In tradition of previous review articles on micro total analysis systems [2, 3], we highlight new developments in manufacturing techniques and materials for microfluidic devices, operational units including droplet microfluidics, and detection methods. The field of applications are continuously growing. We selected here interesting studies for bioanalysis and diagnostics, with the focus on extracellular vesicles, detection of biomarkers, and cell studies. In the light of the pandemic in 2020 caused by the virus SARS-CoV-2, we also emphasize microfluidic methods for viral detection and related studies.

2.2 Materials and fabrication

2.2.1 Materials

Polymers

Many materials are suitable to build microfluidic devices. Most often, polymers are chosen due to their low price and established fabrication protocols. Among them, poly(dimethylsiloxane) (PDMS) is very common, since the production of prototypes by soft lithography is facile, and PDMS is biocompatible, gas permeable, and transparent. However, PDMS is not amenable for mass fabrication, suffers from alteration of surface properties over time, and absorbs hydrophobic substances at its surface. Auner et al. investigated the binding of 19 chemicals to the surface of PDMS. Based on the chemical affinity for PDMS, they implicate that the effective concentration of certain chemicals inside a PDMS device varies up to 1 order of magnitude [4]. Lenz et al. demonstrated that small organic molecules diffuse through PDMS, influenced further by swelling of PDMS when in contact to organic solvents [5]. Therefore, many research groups are working on alternative materials, which have the potential to overcome some of the shortcomings of PDMS.

Thiol-ene based materials, for example, possess an increased resistance to weak solvents. When strong solvents (e.g., chloroform) are introduced, significant swelling was reduced by a heat treatment of the thiol-ene material, as recently shown by Geczy et al. [6] Additionally, the polymer precursor of off-stoichiometric thiol-ene consists of hydrophobic and hydrophilic moieties, which self-assemble on the surface of the material. Shafagh et al. exploited this phenomenon to fabricate a hydrophilic-in-hydrophobic well array. This commercially appealing fabrication procedure generates surface properties, which are long-term stable [7].

Potential commercialization of microfluidic devices is often hindered by the limited capabilities for mass production. Hot embossing, the imprinting of the microfluidic structure under pressure and heat, is a promising manufacturing approach for the commercialization of microfluidic devices. Sun et al. utilized hot embossing to fabricate polypropylene (PP) microfluidic chips. These chips have superior chemical resistance and exceptional antifouling properties, which increases the consistency of bioassay readout compared to PDMS [8].

Silicon-glass devices

Si-glass chips are expensive to fabricate but exhibit excellent pressure and chemical resistance quality. Qi et al. presented a manifold for small Si-chips, which reduces the footprint of single devices to 50 mm^2. On a common 4 in. wafer, up to 80 single microfluidic chips can be produced. This reduces the cost per chip by 2 orders of magnitude, paving the way for single-use Si-glass microfluidics [9]. Si-glass devices are generally fabricated by wet or dry etching processes, which limit the microfluidic channel design to open 2D structures. Kotz et al. succeeded in producing complex 3D structures in fused silica glass. This is achieved by a sacrificial template, which leaves a cavity, the microfluidic channel, inside of the fused silica [10].

2.2.2 Alternative materials

In contrast to rigid materials, hydrogels are soft and, due to their similarity with the extracellular matrix, are far better suited for long-term on-chip cell culture experiments. One major drawback of hydrogel-based chips is the intrinsic swelling of the hydrogel, making it difficult to design and fabricate complex structures. Shen et al. overcame this problem by fabricating microfluidic devices with the nonswelling diacrylated Pluronic F127 (F127-DA). This copolymer is covalently cross-linked and retains its structure and mechanical properties after an equilibrium is established at 37 °C in aqueous solution [11]. Zhang et al. used a biodegradable polymer to fabricate a scaffold for a branched network of seeded cells. This multimaterial system is fabricated by a 3D stamping technique and it allows the integration of a complex 3D network [12].

A remarkable alternative material is wood, which is renewable and biodegradable. Point-of-care (POC) devices, which are generally single-use devices, could benefit from this environmentally friendly material. Andar et al. fabricated wooden microfluidic devices and showed rapid and sensitive protein detection with a POC device, which was fabricated by laser engraving plywood. This inexpensive method of fabricating microfluidic chips is suited for low-resource settings [13].

In common microfluidics, a fluid is in direct contact with the material or the surface coating of the microfluidic device. An alternate approach relies on the guidance of the microscale flows by liquid-liquid interfaces (LLI). The LLI have significant advantages such as their antifouling properties; however, they are restricted to pressures below 1 kPa, which limits their application drastically. A novel method was developed in which porous polytetrafluoroethylene (PTFE) was perfused with a transitional fluid, which enables high-pressure LLI. The dynamic infusion of the porous material guarantees a thin intermediate film of the transitional fluid between the sample solution and the solid matrix. Because the transitional fluid prevents the walls to be exposed to the sample solution, antifouling and molecule absorption is successfully avoided [14]. To complement the list further, widely used and cheap materials are filter paper or tissue paper, which were comprehensively described in previous reviews [15, 16].

2.2.3 Fabrication

Lithography

Optical and soft lithography are the gold standard in the fabrication of PDMS microfluidic devices. Paik et al. improved the resolution below the diffraction limit of the incident light by utilizing an elastic mask. The mask reliably contacts the photoresist due to its elasticity and enables near-field lithography with a significantly higher resolution. The group fabricated the mask by embedding chromium in the desired pattern in a PDMS substrate. It is compatible with common hardware used for soft lithography [17]. In contrast, Trantidou et al. sacrificed resolution ($\sim$200 μm) to reduce the cost per chip significantly. In their method, termed laser lithography, the microfluidic channels are laser cut inside an acrylic sheet and later sealed from both sides by two dry resist film sheets. The cleanroom-free process is straightforward, simple, and reduces the cost for microfluidic chips [18]. The main expenses in the production process of soft lithography originate from the fabrication of the photoresist master mold, which needs significant knowledge and expensive equipment. Additionally, the master mold is prone to damage and has a limited casting life. Therefore, Sonmez et al. developed a polycarbonate (PC) heat molding method to duplicate the photoresist master mold. No expensive equipment is needed to make a PC mold from the master mold. Furthermore, the footprint of the PC mold is unlimited, which makes the process suitable for mass production [19].

Direct laser writing

Multiphoton lithography is a versatile tool to produce 3D structures in the submicrometer range. Vanderpoorten et al. demonstrated that the highly precise process can be combined with standard soft lithography to integrate 3D submicron structures in a microfluidic device [20]. Alsharhan et al. integrated 3D nanostructures in cyclic olefin copolymer (COC) microchannels. The group showed the robustness of the nanostructure up to 500 kPa and printed an actively controllable valve [21]. A complex 3D structure with multiple materials inside a microfluidic channel was fabricated by Mayer et al [22]. The structure consisted of up to five different materials, which were printed by flushing the channel with the specific materials during the writing process.

3D printing

3D printing is a fast, cheap, and flexible fabrication method. The drawback of most commercially available 3D printer is their low printing resolution (>500 μm). Most microfluidic chips have dimensions below 500 μm, which prevents them to be 3D printed with a commercial 3D printer. Moreover, the printing protocol has a significant influence on the printing quality and the maximum resolution of the printer [23]. Recently, microfluidic channels with a 50 μm cross-section were 3D printed with a stereolithographic (SLA) 3D printer. This was achieved by using a specific photocurable ink and precisely controlling the exposure [24]. Polyjet 3D printing offers a superior resolution (<100 μm) than the commonly used SLA and fused deposition modeling (FDM) methods; however, the need for support material for hollow structures is the resolution-limiting factor. Castiaux et al. used liquid support to print microchannels, negating the need for photocurable support. With this method, they were able to print microfluidic channels below 150 μm [25]. In contrast, Li et al. printed channels bigger than 500 μm; however, they succeeded in printing a full microfluidic device with multiple materials in a single step. The device contains transparent acrylonitrile butadiene styrene (ABS), conductive ABS, and two integrated membranes. The simple fabrication method makes it commercially attractive (∼0.20 USD per chip) [26]. Zhu et al. mixed upconversion nanoparticles in the photoresist to achieve a uniform curability over a long exposure distance by a near-infrared laser. This powerful SLA method enables the printing of scalable and freestanding structures [27]. Multiscale 3D printing was also achieved by Li et al. They used a viscous filament in combination with an applied voltage to generate periodic coiling of the printed material. The coiling shape is correlated to the applied voltage. This method grants an incredible high printing speed of up to 10 $cm\ s^{-1}$ [28].

3D channel fabrication

Most microfluidic fabrication methods, such as soft lithography, dry or wet etching, produce planar channels with rectangular channel cross sections. The addition of the third dimension in the fabrication process could largely increase the number of possible applications. Yuan et al. fabricated microfluidic channels by heat drawing structured multimaterial fibers with the desired shape. The heat drawing reduces the macroscale fiber assembly to the desired size in microscale. Additionally, functional elements can be included in the fabrication process such as conductive materials for dielectrophoresis [29]. A different approach exploits elastic crack engineering to fabricate 3D structures. At certain curing conditions, an intentional and controlled crack in the PDMS mold is created. The crack allows the fabrication of closed-loop, 3D structures with a reusable PDMS mold. This method enables high-resolution, rapid, and multimaterial production of microfluidic devices to be produced at low cost [30]. Xiang et al. fabricated a 3D channel system by stacking multiple polymer-films together. The device consists of three layers with complex channel structures and three adhesive layers connecting the channel layers [31].

Well plate insert

The operation of microfluidic devices requires specific equipment and expertise, which is inaccessible for most laboratories. Therefore, researchers are looking for simpler and more easily accessible microfluidic interfaces. Standardized 96-well plates are broadly available. Thus, injection molded polystyrene insets were developed for 12- and 96-well plates to coculture cells separated by a hydrogel. The insets are fixed to the bottom of a well by either a pressure-sensitive adhesive [32, 33] or a springlike mechanism [34] (Fig. 2.1). The cell solutions are loaded by pipetting in combination with capillary forces into the specific compartments.

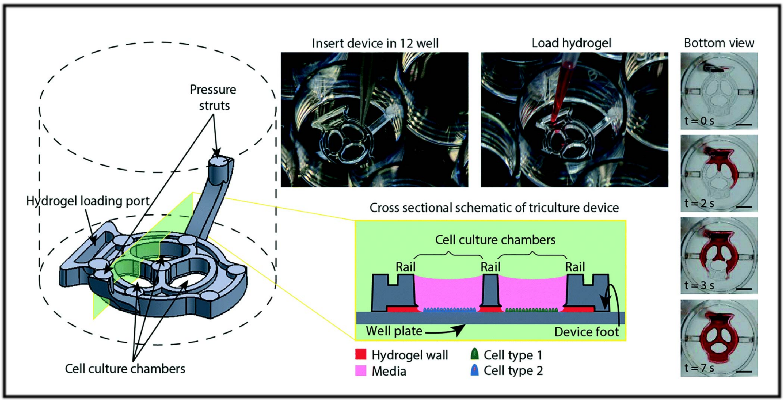

Figure 2.1: Well plate inserts were developed to coculture cells in 12- or 96-well plates. The injection molded inserts are designed for mass production and are easy to integrate into common culture protocols. Adapted from Day, J. H.; Nicholson, T. M.; Su, X.; Van Neel, T. L.; Clinton, I.; Kothandapani, A.; Lee, J.; Greenberg, M. H.; Amory, J. K.; Walsh, T. J.; et al. Lab Chip2020, 20, 107-119 (ref [34]), with permission of The Royal Society of Chemistry.

2.2.4 Coating

The intrinsic surface properties of various materials are well suited for simple devices but are not sufficient for more complex and highly specialized applications. Depending on the application of the microfluidic device, it is desired to have either superhydrophobic or superhydrophilic surfaces. Generally, this is accomplished by various coatings applied after the fabrication and bonding of the device.

Antifouling

Microfluidic devices are excellently suited to analyze minuscule biological samples such as blood or salvia. The samples are generally analyzed based on the activity of targeted molecules, which enables a fast and specific readout. However, the untargeted binding of biological molecules to the device material, called fouling, hinders the use of microfluidic devices in numerous applications. Sabaté del Río et al. reduced the fouling of electrodes by applying a matrix of bovine serum albumin intermixed with conductive nanomaterial. The coating prevented unspecific binding for 1 month in human blood serum effectively [35]. Liu et al. cross-linked titanium dioxide (TiO_2) nanoparticles with vinyl-terminated PDMS to fabricate a coating with superhydrophobic and antibacterial properties. The TiO_2 nanoparticles self-assemble into a thin layer on the surface of the substrate. The photocatalytic active property of the TiO_2 degrades biological debris exposed to UV light and gives rise to self-cleaning properties of the substrate. Furthermore, the superhydrophobicity leads to significant blood repellency, which has great potential in medical applications such as wound dressing or in microfluidic devices for whole blood sampling [36]. A similar effect was reached by lubricin-inspired triblock copolymers, which were designed to strongly adhere to a silica surface and, at the same time, expose antiadherent moieties toward the sample. These so-called bottlebrush polymer-coated surfaces are exceptionally stable and show extreme low fouling properties [37].

Cell adherence

Microfluidic devices are excellent tools to cultivate cells under highly defined conditions. A major drawback is the unpredictable cell adhesion and proliferation on the surface of synthetic materials of microfluidic devices. Piironen et al. showed that certified biocompatibility of 3D printed materials is not a good indicator of cell survival on the surface. The more important factor is the ability to autoclave the material previous to use [38]. To stabilize and promote cell adhesion in a PDMS device, poly-d-lysine-conjugated Pluronic F127 (F127-PDL) was used successfully. The simple one-step introduction and incubation technique was utilized in neuron differentiation and growth and showed significantly better results compared to uncoated PDMS [39]. In contrast, Liu et al. exploited the water solubility of amorphous silk proteins to functionalize micro- to nanoscale patterns on various substrates. The biocompatible process relies on inkjet-printed water droplets and its subtractive effect on the silk film. The silk film was functionalized with collagen (cell adherent) or Temozolomide (cell growth inhibitor) to increase or decrease cell adhesion on the substrate [40]. The bonding of PDMS to a glass substrate is generally attained by O_2 plasma activation of the surfaces and subsequent covalent bonding of the two materials via the generated hydroxyl groups. In contrast to O_2 plasma, CO_2 plasma generates carboxyl and hydroxyl groups on the glass substrates. Shakeri et al. used carboxyl groups, generated by CO_2 plasma, to micropattern antibodies on the glass surface. This straightforward technique enables the coating of the channel with fibronectin to precisely define the area in which cells adhere to the glass substrate [41].

2.3 Operational units

2.3.1 Pumping

Selecting the right pumping system for microfluidic devices is essential to generate specific fluid flows or decrease the footprint for applications such as point-of-care (POC) testing. Discovering new ways of self-sufficient and easy to integrate pumping devices has become more important in recent years. One such development employs a commercially available latex balloon to push liquid through microfluidic channels. The flow rate can be controlled by changing the size and thickness of the balloon and actively squeezing it leads to an instant pressure change. To show the applicability of this device, experiments were conducted under different liquid viscosities and temperatures, using various microfluidic structures [42].

Park and Park established finger-actuated microfluidic pumps and valves that operate as one unit, allowing on-demand flow control and constant volumes independent of user variation. In contrast to other types of finger-actuated devices, deflection of the polydimethylsiloxane (PDMS) membrane is induced by a pressure change in the pneumatic channels, allowing a simultaneous actuation of valves. Thus, sequential delivery of reagents, followed by a nucleic acid purification on-chip without any external equipment was demonstrated [43]. Furthermore, a modular finger-powered actuator was fabricated entirely by MultiJet 3D printing. In this way, fluid flow rates from 100 to 300 $\mu L\ min^{-1}$ were achieved with a significantly reduction in backflow [44]. Additionally, most microfluidic pumps require complicated fabrication techniques due to a variety of moving parts, microstructures, or electrical contacts. Therefore, another group introduced a micropump based on photoacoustic laser streaming. By exciting a quartz plate implanted with Au particles with a pulsed laser, an ultrasound wave was generated to drive the liquid flow via acoustic streaming [45].

The disadvantage of standard pumps is the requirement for power to achieve high and constant flow rates. However, Seo et al. demonstrated a suction pump made of sodium polyacrylate, a polymer with a high swelling ratio. This leads to an increased amount of absorbed liquid to generate flow rates of $\sim$80 $\mu L\ min^{-1}$ for more than 4 h. By integrating the pump with reverse electrodialysis, a portable battery was created, generating $\sim$70 $\mu W\ cm^{-2}$ for 1 h by using only saline solutions without any external power sources [46].

Numerous microfluidic devices are based on the passive principle of the capillary effect at microscales. The use of capillary forces as an actuation mode holds the advantage of being passive without any active part; however, it is slow and liquid transport is limited. Chen et al. investigated the directional and ultrafast water transport on the surface trichomes of pitcher plants (Sarracenia) and designed a microfluidic channel with a similar surface structure. They successfully increased the passive water transport in a hierarchical microfluidic channel by 3 orders of magnitude [47].

One unique example of pumping in microfluidics is the formation of a biohybrid valveless pumping device driven by engineered skeletal muscle cells. This device, reported by Li et al., is able to generate a unidirectional flow of 22.5 $\mu L\ min^{-1}$. The so-called pump-bot is made of a soft hydrogel tube, which is surrounded by a ring of muscle cells, connected to stiffer PDMS channels [48].

2.3.2 Valves

Traditional pneumatically controlled microfluidic valves are fabricated by using multilayer soft lithography and paved the way toward a variety of fluid handling operations on-chip. Since then, microfluidic architectures have become more complex and the requirements for newer devices have risen. Large arrays of valves have become to be the standard, but addressing each of them individually remains difficult. By creating an array of valves made of shape memory polymer (SMP), individual valves can be triggered by localized joule heating combined with a global pneumatic air supply. Cross-heating of neighboring valves was avoided by patterning the SMP membrane with stretchable carbon-silicone composite heaters. This concept allows more than 3000 cycle operations and enables a permanent latching for more than 15 h [49]. Furthermore, it was shown that SMP can be used to develop programmable microfluidic chips, which act as simple logic circuits [50].

Valves for centrifugal microfluidics were investigated as well, such as passive elastic reversible (ER) valves or active electromagnet-triggered pillar (ETP) valves. There are two different types of ER valves. Fixed ER valves that are easy to integrate into microfluidic discs by adding a small piece of PDMS acting as a seal. The sealing pressure can be adjusted during the fabrication process. Tunable ER valves that make use of an additional plastic screw to adjust the sealing pressure and, thus, increase the controllability of the system. These ER valves can retain liquids up to 420 kPa [51]. While passive valves are actuated solely by centrifugal forces, active valves, such as the ETP valves, have the advantage of releasing reagents on demand. ETP valves are composed of a metal pillar that is embedded in the microfluidic chip. The top of the chip is sealed with pressure-sensitive adhesive tape. By lifting the metal pin using an electromagnet, the adhesive tape separates from the substrate and the liquid can pass through [52].

Most valves operate in dimensions of micrometers. Developing valves for nanofluidic devices remains challenging but was achieved by Kitamori and coworkers on glass devices. The 10-1000 nm-sized nanochannels could be closed or opened by bending a thin glass plate using a piezoelectric driven actuator [53].

2.3.3 Gradient formation

The low Reynolds numbers in microfluidics predominantly result in a laminar flow, which is important for the generation of accurate biochemical concentration gradients for numerous biological applications. Usually, a variety of concentration conditions are tested in microtiter plates by using automation facilities. However, the formation of concentration gradients along a microarray on-chip is a time saving and inexpensive approach with the possibility of scaling down to a small colony-sized- [54], single-cell-, or even single-molecule-sized level [55].

Other groups generated multiple gradients on a chip, enabling certain biological applications. One team proposed a radial microfluidic device, in which chemotaxis studies of eight different cell types under different gradient conditions were performed in parallel [56]. Another group made use of two orthogonal gradients to expose bacteria, immobilized in an agarose gel, to a variety of antibiotic concentration combinations [57].

All of the previously described gradients were generated in the same direction as the flow. However, for some biological or analytical applications, it is advantageous to establish concentration gradients with different shapes or patterns. Recently, Perrodin et al. designed a microelectrode to form steady-state linear proton gradients perpendicular to the fluid stream in a microfluidic channel. Thus, parallel streams, splitting steps, and precise control of the microfluidic circuit are not required [58].

2.3.4 Mixing

Since microfluidic chips exhibit laminar flow profiles, the mixing of substances relies on molecular diffusion in passive mixing devices. This slow and passive process can be enhanced by additional serpentine-shaped channel structures. Enders et al. fabricated five different passive micromixers using multijet 3D-printing and compared the mixing efficiency under similar dimensions and by applying the same methods [59].

In contrast, active mixers can achieve significantly higher homogenization grades and allow for adjustments of the mixing performance independent of the flow rate. One such investigation employed nanoscale stir bars consisting of bioconjugated magnetic nanochains powered by magnetic fields integrated into a microfluidic chip. In addition to the mixing-function, the functionalized surface can be used to capture molecules for bioseparation (Fig. 2.2A) [60].

Another active mixing strategy, which became popular over the recent years, is conducted by acoustic-driven micromixers. Surface acoustic waves (SAW), bulk acoustic waves, or acoustically vibrating microstructures transfer acoustic energy into the fluid to homogenize it. By oscillating sharp edges and bubbles within the microfluidic channels using a piezoelectric transducer, acoustic microstreams were generated, reducing the mixing time to 0.8 ms at a flow rate of 116 $\mu L\ min^{-1}$ (Fig. 2.2B) [61]. Based on the same principle, an oscillating star-shaped acoustic-driven micromixer reached a mixing time of 4.1 ms at a flow rate of 8 $mL\ min^{-1}$ [62]. By inducing acoustic streaming in a valve controlled chamber using SAW, mixing times of 5 s for 153 nL and 1.5 s for 44.3 nL at a frequency of 70.9 MHz were achieved [63].

A different mixing approach was demonstrated by Zhang et al. using reactive inkjet printing to fabricate autonomously rotating biocompatible silk-based micro-

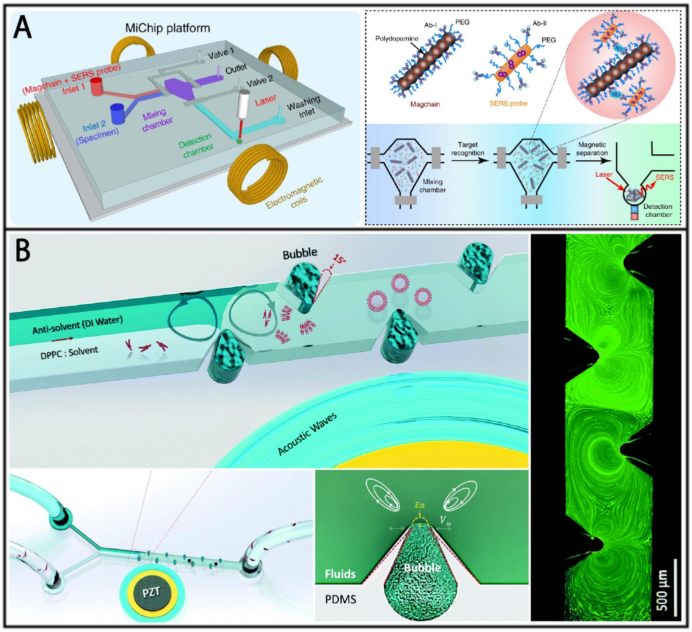

Figure 2.2: Active mixing techniques. (A) Bioconjugated magnetic nanochains powered by magnetic fields acting as nanoscale stir bars. The functionalized surface allows one to capture analytes for bioseparation. Adapted with permission from Macmillan Publishers Ltd.: NATURE, Xiong, Q.; Lim, C. Y.; Ren, J.; Zhou, J.; Pu, K.; Chan-Park, M. B.; Mao, H.; Lam, Y. C.; Duan, H., Nat. Commun.2018, 9, 1-11 (ref [60]). Copyright 2012 under a Creative Commons Attribution 4.0 International License (https://creativecommons.org/licenses/by/4.0/). (B) Acoustically vibrating sharp edges and bubbles transfer acoustic energy into the fluid to achieve mixing times of 0.8 *ms* at flow rates of 116 $\mu L\ min^{-1}$. Adapted from Rasouli, M. R.; Tabrizian, M. Lab Chip2019, 19, 3316-3325 (ref [61]), with permission of The Royal Society of Chemistry.

stirrers. The rotary movement is induced either by the release of surfactants and driven by the Marangoni effect or by catalytically driven bubble propulsion. Since these micromixers are not dependent on any external energy sources, they could find application in POC platforms where diffusion limits have to be overcome [64].

2.3.5 Filtration and separation

Filtration

Sample preparation methods are usually required to improve a subsequent detection. Enrichment of cells or particles by size can be accomplished by filtration. Since filter clogging is a major drawback, cross-flow filtration can be integrated in a microfluidic device, which takes advantage of the microfluidic streams. Recently, a microfluidic chip was reported which combines inertial forces and cross-flow filtration for volume reduction and, thus, up-concentration of a cell suspension. This device was characterized over a flow rate range of 3-6 $mL\ min^{-1}$. A 1'100-fold increase of white blood cell concentration was achieved by using a multistep serial concentrator [65]. Another group used the cross-flow filtration principle by integrating a nylon mesh membrane with a pore size of 5-50 μm into a microfluidic device to separate cell aggregates from tissue fragments. Further dissociation into single cells was possible due to hydrodynamic shear forces and physical interactions with the nylon mesh. Single-cell numbers of minced and digested murine kidney, liver, and tumor tissues were increased up to 10-fold [66].

Applying an electric field across a membrane enhances the extraction selectivity of molecules and provides high sample preconcentration and cleanup. By implementing nanoliter-scale electro-membrane extraction inside a microfluidic device, model analytes from a 70 μL blood, plasma, or urine sample were extracted into an acceptor solution. The enrichment capacity was 6- to 7-fold per minute, and after 1 h, 400-fold enrichment was achieved [67]. In a different approach, an electrochemical membrane made of a porous platinum electrode was used to remove dissolved oxygen from the surface of an electrochemical sensor to allow the detection of molecules that are usually not detectable in the presence of oxygen [68].

Separation

A variety of other techniques was applied in microfluidic devices to sort and concentrate molecules or particles based on properties other than size. Recent improvements have led to enhanced separation or purification of target cells and molecules. Electrophoresis and gel electrophoresis allow for the separation of analytes based on their charge and are routinely used to separate proteins. It usually lacks good separation resolution and, thus, is unable to identify variants of a single protein. Yet, Linz and co-workers demonstrated the separation and preconcentration of the fluorescently labeled model protein, ovalbumin, into its three variants by microfluidic thermal gel electrophoresis [69]. Electrophoretic separation of amino acids and preterm birth risk biomarkers was also achieved (peptide 1, CRF, ferritin) in a stereolithographic 3D printed microfluidic chip [24]. To enhance the separation resolution in immunoprobed isoelectric focusing, Jeeawoody et al. increased the pore sizes of a polyethylene glycol (PEG) polyacrylamide (PA) gel by utilizing lateral chain aggregation. Thus, the 2% PEG PA gel not only reached a higher resolution than unmodified PA gels but also a lower immunoassay background signal [70]. On the other hand, to reduce mass transport limitations in immunoassays, the same group developed a microarray-microparticle hybrid for single-cell immunoblotting. Roughly, 3500 microparticles were formed in an array for single-cell isolation and protein electrophoresis and subsequently mechanically released. Thus, a solution of microparticles is produced, in which each particle is encoded with a single-cell protein separation [71].

Another separation method was performed by applying magnetic fields on a magnetically labeled target. The advantage of labeling specific molecules or cells with antibody-functionalized magnetic particles is an increase in target selectivity. (e.g., high-purity sorted white blood cells) [72]. Others utilized the differences in magnetic moments of particles, allowing to sort a set of catalyst-particles based on their iron content in a 3D printed microfluidic chip [73]. For more specific separation techniques, fluidic streamlines or viscoelasticity can be used to separate particles not only based on shape and size but also on elasticity or diffusivity. One group demonstrated the separation of a mixture of spherical particles and worm-like micelles into four substreams by cross-streamline migration in a sinusoidal microchannel [74]. Another way to separate particles into different streams was performed by generating a bidirectional flow using an array of field-effect electrodes. Molecules with high diffusivity rapidly diffuse across the streamline whereas larger particles diffuse slower and maintain their stream trajectory [75]. By designing a reversed wavy channel structure in combination with a viscoelastic fluid, elasto-inertial focusing and separation of nanoscale particles were realized [76].

2.3.6 Droplet microfluidics and digital microfluidics

Droplet microfluidics allows for rapid and inexpensive compartmentalization of analytes and cells under controlled conditions and is a powerful tool for high-throughput screening. To adapt typical workflows to droplet microfluidics, further improvements were reported such as droplet generation, sorting, merging, trapping, and manipulation, realized by passive and active droplet-control methods.

Droplet generation

When a droplet needs to be released at a specific spatial or temporal resolution, on-demand production of droplets is a favorable technique. Gallium electrodes integrated within a microfluidic chip allowed to release droplets on-demand in three different ways. First, through a programmable DC potential, second, under short AC signals, and third, by AC trigger signals to increase the generation frequency [77]. By deforming an aqueous-oil interface inside a microchannel using a pulsed electric field, femtoliter droplets of different viscous solutions were produced on-demand [78]. Another approach employed two Laplace pressure barriers to generate droplets on-demand by first filling a reservoir before pinching off droplets into a main channel [79]. In addition to the time point when a droplet is released, the order and number of targets, e.g., cells or particles, to be encapsulated is also of importance. Delley and Abate designed a so-called particle zipper to co-encapsulate the desired number of particle types that originated from two different close-packed particle streams into one droplet [80]. Another interesting approach is the generation of all-aqueous double- and triple-emulsions with the advantage of being highly biocompatible [81]. After generation, droplets can be merged, which is interesting for temporal and spatial triggering of chemical reactions. Merging can be achieved passively by interfacial tension [82] or actively by acoustofluidics. The latter was used to merge two surfactant-stabilized droplets based on their fluorescent levels. A merging efficiency of 100% was reported with a maximum merging frequency of 10^5 droplets per hour [83].

Droplet sorting

Droplet cytometry and sorting is an attractive technique for single-cell analysis. In particular, the accumulation of cell-secreted factors in droplets is intriguing as it is not possible with commercial cytometers and cell-sorting instruments. The large demand for these methods has driven recent advancements in passive and active droplet sorting methods. For example, Pan et al. showed that the interfacial tension changes with the ph, when specific surfactants are chosen, which allows for passive and label-free sorting based on ph [84]. Passive high-throughput size-based sorting of hydrogel droplets was realized by inertial forces resulting in cross-streamline migration [85]. Fluorescence-activated droplet sorting is a well-established technique and can be found in many microfluidic devices. In contrast, droplet sorting based on fluorescence lifetime is rarely applied due to its low throughput. By implementing a customized field programmable gate array, the data processing rate for calculating the fluorescence lifetime enhanced the sorting throughput up to 2.5 kHz [86].

Droplet storage

Aligning droplets in an array is a powerful way to process and monitor thousands of distinct events at the same time and is usually conducted passively by specific trapping architectures. Thereby, the trapping efficiency and array-density is constantly improving [87] and tailored to the needs of droplet composition and application [88]. While passive techniques have the advantage of achieving very high throughputs, active storing systems, on the other hand, have the ability to precisely set the droplet to the desired location. This can be achieved by pregenerating droplets and placing them precisely using an XYZ-positioner onto a 2D-array-plate. Nelson et al. expanded this method to print 3D-arrays into a bath of yield stress fluid where droplets remain at the position they were printed [89]. Furthermore, a microcage-array chip was developed, where microcages are surrounded by multiple micropillars, allowing the creation of approximately 1’000’000 droplets within 90 s. The massive scale, rapid creation, and the ability to retrieve localized droplets makes this platform interesting for future high-throughput screening applications [90]. A complete opposite approach was performed by sorting droplets with electrodes into a 3-branch channel. Each channel leads to a rotation platform composed of 10 microtubes, which allow the fractionation and collection of the droplets into 30 subgroups [91].

Droplet interfaces

A major drawback of droplet microfluidics is the leakage of hydrophobic compounds from the aqueous-phase to the oil-phase. Instead of adding them directly to the aqueous phase, solubilizing hydrophobic substances in the oil compartment force a diffusion by partition back into the aqueous phase. Subsequently, the partition coefficient determines the concentration in the aqueous phase [92]. Another limitation is the transfer of substances between surfactant-stabilized droplets as well as the droplet coalescence at higher temperatures. Chowdhury et al. found that dendritic triglycerol-stabilized droplets are a robust solution and significantly better at preventing interdroplet transfer than polyethylene glycol-based surfactants [93].

In-droplet manipulation

Separation and enrichment of molecules or particles inside droplets can realize more sophisticated workflows and can be done by application of external forces, such as magnetic-, dielectric-, and acoustic forces. Recently, surface acoustic wave-driven acoustic radiation forces were added to the possibilities to focus particles inside of a droplet. The droplet was split into one daughter-droplet containing the particles and one without the particles. The daughter droplets with particles were subsequently merged with the next droplet in line, thereby transferring the particles into a new buffer [94]. To separate small molecules inside a droplet, Saucedo-Espinosa and Dittrich used two carbon composite membranes to apply a uniform electric field across a microchannel to migrate and accumulate molecules based on their net-charge. The droplet was split by a Y-junction into two portions, containing enriched and oppositely charged species (Fig. 2.3A) [95]. Utilizing cation-permselective membranes not only allowed the separation of charged species but also the exchange of cations. Thus, cations were exchanged with calcium-ions leading to an increased fluorescence level of a calcium-sensitive dye [96]. Another elegant solution for analyte enrichment in individual droplets was recently presented. Droplets were immobilized in cylindrical microwells within a PDMS device and experience significant shrinkage due to water diffusion into the PDMS. Consequently, protein oligomers dissolved in the droplets at femtomolar concentrations and were up-concentrated by a factor of 100’000 [97].

Wells and Kennedy introduced a method to bring aqueous droplets and droplets with organic solvents in contact, which allows rapid and simultaneous liquid-liquid extraction of multiple nanoliter droplets. Extracted analytes were later detected by electrospray-ionization mass spectrometry with an improved detection sensitivity [99].

Digital microfluidics

Digital microfluidics (DMF) is as an interesting and alternative technique for several applications such as assays, synthetic biology, or point-of-care diagnostics. Applying an electrical field across a 2D-array, forces a change in the shape and contact

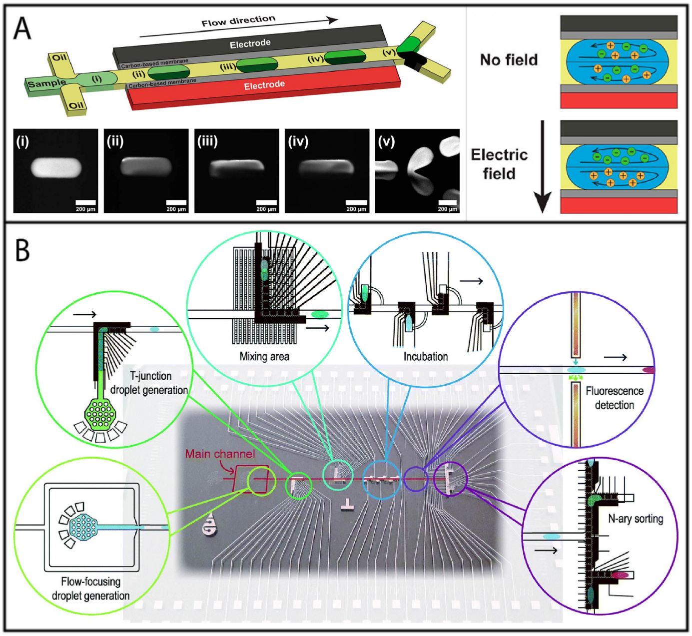

Figure 2.3: Process steps integrated in droplet and digital microfluidic platforms. (A) In-droplet separation of small molecules by applying a uniform electric field, realized by two carbon-composite membranes integrated alongside the channel. Further, the droplets were split into two portions containing the enriched and opposite charged species. Adapted from Saucedo-Espinosa, M. A.; Dittrich, P. S. Anal. Chem.2020, 92, 8414-8421 (ref [95]). Copyright 2011 American Chemical Society. (B) Integrated microfluidic platform combining the advantages of droplet and digital microfluidics to allow droplet generation in a flow-focusing module and manipulation by pressure- and electrical-based methods. Adapted from Ahmadi, F.; Samlali, K.; Vo, P. Q. N.; Shih, S. C. C. Lab Chip2019, 19, 524-535 (ref [98]), with permission of The Royal Society of Chemistry.

angle of a droplet, referred to as electro-wetting. In the recent years, several groups realized complex bioassays by means of DMF, often in combination with magnetic forces to further expand the process. For example, a fully automated CRISPR-Cas9 editing platform for cell culturing, transfection, gene editing, and analysis was established [100]. Additionally, an entire ELISA-like assay for influenza A H1N1 virus diagnosis on a DMF-device was performed in 40 *min* by using electromagnetic forces [101]. Another group developed a free-standing, DMF immunoassay platform to detect four different types of chemical and biological warfare agents from aerosols [102]. Furthermore, Dixon et al. presented a DMF device for blood-plasma separation with a subsequent diagnostic assay and direct sample loading capability of whole blood [103].

However, when a target compound is present in too low concentrations, a larger sample volume is required, which makes DMF no longer applicable as it is limited to sample volumes in the lower microliter range. For this reason, a sample preconcentration unit was designed, which can directly interfere with a DMF-device. With this setup, the DNA present in a 1 mL urine sample was preconcentrated into a 1 μL volume using magnetic particles, which made further processing on the DMF-chip possible [104]. A promising advancement is an integrated droplet microfluidics-DMF platform that combines the advantages of droplet generation in microchannels with manipulation methods based on electro-wetting to realize complex liquid-handling operations. Thus, droplet generation, -mixing, -incubation, -detection, and -sorting was performed on one device, here demonstrated for yeast culture grown under various conditions (Fig. 2.3B) [98]. Zhang et al. established digital acoustofluidics. With this method, droplets were manipulated on the surface of an immiscible oil layer via hydrodynamic traps induced by three-dimensional acoustic streaming [105].

2.4 Detection

2.4.1 Electroanalytical methods

Electroanalytical detection methods are very attractive for microfluidic devices since they can be integrated in miniaturized platforms. A new dual-marker biosensor chip demonstrated a robust measurement of glucose and insulin with a joint Ag/AgCl reference/counter electrode and two Au working electrodes [106]. It achieved a limit of detection (LOD) of glucose and insulin at 0.2 mM and 41 pM, respectively. Flexible electrodes with roll-to-roll slot-die coating were presented for the reproducible detection of dopamine with an LOD of 0.09 $\mu mol\ L^{-1}$ [107]. In another application, the electric resistance measured through four wires was used to monitor the bacterial cell growth in a parallel fashion to estimate antibiotic susceptibility [108]. A polyaniline nanofiber modified screen-printed electrode was utilized for the detection of circulating tumor cells [109]. Rajendran et al. developed a lab-on-a-disc platform to allow electrochemical detection of active compounds by voltammetry and amperometry while rotating [110]. Furthermore, a field-effect transistor array was utilized to quantify only captured cells with a positive correlation between current gain and the number of captured cells [111].

Electrical impedance spectroscopy (EIS) can be used to study and characterize cell membranes through their specific resistance. This can be achieved with commercially available chopstick-like electrodes. By changing the input signal from direct to alternating currents with varying frequencies, the cell layer capacitance was calculated [112]. While typical impedance measurements are carried out in well-plate formats, an integrated droplet microfluidic system coupled to a microelectrode array for single cells was reported [113]. This allowed the observation of dynamic changes with better controllability and the possibility to integrate additional analytical systems more easily. Another device was reported with the ability to monitor the physical properties of droplets in real-time through impedance measurements [114]. This provides a tool for fine-tuning and characterizing droplet generation. Recently, EIS was extended to single plant cells for studying primary cell wall regeneration [115].

2.4.2 Raman spectroscopy

Surface-enhanced Raman scattering (SERS) is attractive due to its low limit of detection and high spatial resolution. A new method of synthesizing multiple SERS substrates in a single microfluidic channel was reported. It achieved multiple detection capabilities and resulted in SERS barcodes at a detection limit of $10^{-14}\ M$ [116]. A strategy to detect two biomarkers at the same time was reported on a fully automated microfluidic device that features two parallel microfluidic channels for the SERS detection [117]. Through directly measuring chemically specific intracellular molecular vibrations, the need for labeling for cellular phenotyping is omitted. Nitta et al. reported label free real-time sorting of single live cells by coherent Raman scattering with of throughput up to $\sim$100 events per second [118].

Much effort has been invested into the design and regeneration of SERS substrates. While stationary substrates offer better reproducibility than colloidal ones, they suffer from the so-called memory effect caused by irreversible adsorption of analytes. This could be overcome by utilizing an electrically regenerable SERS substrate, i.e., a silver electrode, that strips off the adsorbed analytes, opening the possibility for quasi-real-time SERS detection in a continuous microflow [119]. Finally, SERS detection for single-cell analysis in droplet microfluidics was reported by Willner et al. Encapsulated single prostate cancer cells and wheat germ agglutinin functionalized SERS nanoprobes were locked into a droplet storage array for investigation [120]. Through the use of an automated tool, it was possible to acquire SERS maps without first using white-light imaging. This rapid detection and evaluation primes SERS for the rapid droplet-based screening.

2.4.3 Optical methods

Integration of optical detection is usually straightforward on transparent microfluidic devices and microscopes are widely accessible. Fluorescence measurements provide high selectivity and sensitivity, and a large number of fluorophores and fluorogenic assays are available. Through the combination of optical encoded and biomarker specific fluorescence, a new in situ phenotyping method of circulating tumor cells (CTCs) was reported (Fig. 2.4B). The employed magnetic nanospheres exhibited fluorescence emissions with minimal spectral overlay under simultaneous excitation, allowing a multiplexed detection of three biomarkers [121]. Single-cell protein profiling was reported for CTCs captured in 1026 microchambers through the coimmobilization of cells and barcoded magnetic beads [122]. Multiplexed detection of three potential cancer drug targets was demonstrated with LODs of 43.1 $ng\ mL^{-1}$, 19.6 $ng\ mL^{-1}$, and 1.2 $ng\ mL^{-1}$ for GAPDH, Gal-3, and Gal-3bp, respectively. Combination with ultrabright fluorescent nanoscale labels as recently presented may further improve the sensitivity of fluorescence methods [123]. A concentration step may also enhance the sensitivity and was achieved by trapping individual droplets in cylindrical microwells and shrinking them through water extraction (Fig. 2.4A). Kopp et al. demonstrated detection of soluble protein oligomers at femtomolar concentrations through an analyte up-concentration of up to 100’000-fold within the droplets [97].

Other more specialized optical methods can be combined with microfluidics. For example, thermoresponsive hydrogels with Prussian blue as an analyte-associated photothermal agent were employed, which was triggered by a near-infrared laser [124]. The thermal image- and distance-based readout was able to detect silver ions at a concentration as low as 0.25 μM. Infrared photodissociation

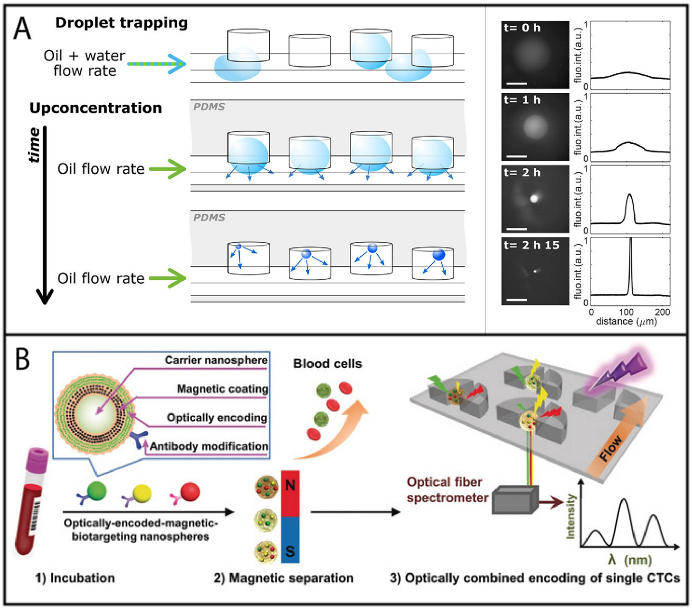

Figure 2.4: High-sensitivity analysis of proteins. (A) Up-concentration of molecules by droplet shrinkage. Droplets are trapped in wells on a PDMS device and shrink over time. The water-soluble analytes remain in the droplets and are up-concentrated, here visualized by increased fluorescence intensity. Adapted from Kopp, M. R. G.; Linsenmeier, M.; Hettich, B.; Prantl, S.; Stavrakis, S.; Leroux, J. C.; Arosio, P. Anal. Chem.2020, 92, 5803-5812 (ref [97]). Copyright 2011 American Chemical Society. (B) Workflow for isolation and phenotypic profiling of circulating tumor cells (CTCs), captured from a blood sample by using magnetic nanospheres. The optical barcode of the nanospheres allows for identification of three surface markers to differentiate CTC phenotypes. Adapted from Spectrally Combined Encoding for Profiling Heterogeneous Circulating Tumor Cells Using a Multifunctional Nanosphere-Mediated Microfluidic Platform, Wu, L. L.; Zhang, Z. L.; Tang, M.; Zhu, D. L.; Dong, X. J.; Hu, J.; Qi, C. B.; Tang, H. W.; Pang, D. W. Angew. Chem. Int. Ed. Engl., Vol. 59, Issue 28 (ref [121]). Copyright 2014 Wiley.

combined with mass spectrometry is gaining attention for its ability to distinguish isobaric compounds and to provide additional structural information. A cryogenic ion trap vibrational spectrometer was coupled to a microfluidic chip for the online monitoring of isomeric flow-reaction intermediates [125].

2.4.4 Mass spectrometry (MS)

Interfacing microfluidic devices with mass spectrometers, particularly for cellular analysis, is another interesting area of research. For example, a spiral microfluidic chip for single-cell sampling assisted by inertial forces was interfaced with inductively coupled plasma MS (Fig. 2.5B). By introducing an internal standard, real-time quantification of intracellular target elements was achieved [126]. A microfluidic surface extractor coupled to electrospray-ionization quadrupole time-of-flight MS was designed for the direct study of cell membranes (Fig. 2.5A). It was applied to discriminate three subpopulations of human tumors via principal component analysis [127]. Furthermore, Piendl et al. reported a heart-cutting 2D chip-HPLC with a monolithic electrospray emitter for the label-free analysis of demanding isobaric and biological sample mixtures [128]. Through this separation method, the detection of isobaric compounds in less than 4 *min* was demonstrated.

Moreover, a potent device for mass-activated droplet sorting was introduced by Holland-Moritz et al. [130] Enzymatic reactions in nanoliter droplets can be sorted at a throughput of 0.7 *Hz* based on the presence/absence of selected signals in the mass spectrum. This was possible by splitting droplets and analyzing the daughter droplets by ESI-MS, while putting the corresponding daughter droplets in a long channel on hold, before sorting them with a dielectrophoretic sorting module. Another strategy uses a fluorescence-activated cell sorter to deposit selected cells in a nanoliter sample processing chip, which enabled quantitative proteomic analysis of single mammalian cells [131] Recently, a parallel droplet splitting method was published, capable of splitting 6000 droplets in a few seconds (Fig. 2.5C) [129]. This has allowed the MS analysis of supernatant, while the cells are still viable and thus can be retrieved and cultivated afterward.

Open microfluidic systems with an array or a well-like design can be interfaced with matrix-assisted laser desorption/ionization (MALDI)-MS without much effort. For the discovery of antimicrobial resistance biomarkers, Zhang et al. coupled a microfluidic device to a MALDI-MS. From the MALDI-MS spectra, differential peaks were utilized to narrow potential biomarkers down for transcriptome conformation [132]. A new method of recording the lipid profile of cells and mem-

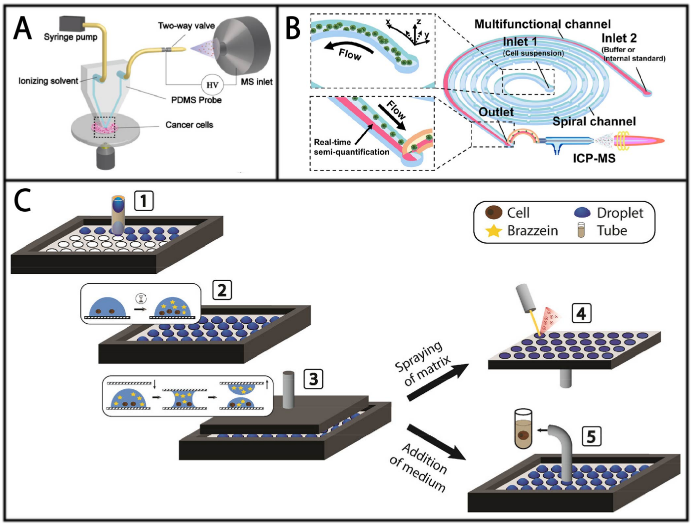

Figure 2.5: Interfaces for microfluidics and mass spectrometry. (A) Microfluidic probe for in situ extraction of lipids from adherent cancer cells, coupled to ESI-MS. Adapted from Liu, P.; Huang, Q.; Khan, M.; Xu, N.; Yao, H.; Lin, J. M. Anal. Chem.2020, 92, 7900-7906 (ref [127]). Copyright 2011 American Chemical Society. (B) Microfluidic device aiding the analysis of intracellular targets in single cells by time-resolved ICP-MS. Single-cell sampling is achieved by means of inertial forces in the spiral microchannel with 104 periodic dimensional confined micropillars. Adapted from Zhang, X.; Wei, X.; Men, X.; Jiang, Z.; Ye, W. Q.; Chen, M. L.; Yang, T.; Xu, Z. R.; Wang, J. H. Anal. Chem.2020, 92, 6604-6612 (ref [126]). Copyright 2011 American Chemical Society. (C) Parallel splitting of nanoliter droplet arrays for analysis of cell supernatant by MALDI-MS. Daughter droplets on the top plate are subjected to mass spectrometric analysis, while droplets on the bottom plate are used for continuous cell cultivation. Based on the mass spectra, individual droplets with cells can be transferred to large cultivation flasks. Adapted from Haidas, D.; Napiorkowska, M.; Schmitt, S.; Dittrich, P. S. Anal. Chem.2020, 92, 3810-3818 (ref [129]). Copyright 2011 American Chemical Society.

brane extracts by combining microarrays with MALDI-MS was presented [133]. This workflow improved reproducibility, a well-known issue in MALDI-MS, and can be easily implemented with microfluidics for, e.g., lipid biomarker discovery. By employing self-assembled monolayers inside a 3D microfluidic chip, enzyme kinetics were studied. These monolayers immobilized the product and posed as a matrix for ionization. A total of 2592 reactions were screened to map the reaction process, which required about 200 times less reagent volume than traditional multiwell plate tests [134].

2.4.5 Other methods

Calorimetry is now reaching subnanowatt sensitivity with low noise, making it accessible for single-cell studies. Three devices were recently reported using calorimetry for biological applications. One high-sensitivity microfluidic chip calorimeter reached a high calorimetric sensitivity of 0.2 nW for single-cell metabolic rate measurements, proven by the measurement of *Tetrahymena thermophila* [135]. The metabolic study of individual Caenorhabditis elegans worms was also reported recently [136]. The third platform focused on antimicrobial susceptibility testing, providing a better understanding of metabolic processes upon drug exposure [137].

A microfluidic chip was designed for nuclear magnetic resonance (NMR) measurements by deterministic electrode placements [138]. Chitosan electrodeposition was successfully detected, opening NMR to other electrochemical applications. Other papers reported the coupling of microfluidics to small-angle X-ray scattering or time-resolved cryo-EM [139, 140].

A continuously infused microfluidic radioassay was presented with a large 3D field of view mini-panel positron emission tomography (PET) scanner [141]. This improves existing tools in the field of pharmacokinetics by enabling parallel infusion allowing higher throughput. Lately, a platform for the detection of Escherichia coli whole-cells was published. The label-free interferometric reflectance imaging enhancement allowed for the sensitive detection of individual pathogens captured on the surface [142]. The extrapolated limit of detection was calculated as 2.2 $CFU\ mL^{-1}$, and no sample preparation was required. PET radiotracers are, due to their unstable nature, difficult to generate precisely, especially in a clinical setting. This bears the need for rapid and precise characterization of the generated labels before usage. To address this issue, two different microfluidic quality control platforms were reported. The first employed a pulsed amperometric detection of carbohydrate-based radiotracers, which was used to test [18F]2-fluoro-2-deoxy-d-glucose in a flow injection analysis [143]. The second combined a silicon photomultiplier light sensor with a microfluidic plastic scintillator for the detection of [18F]fluoride [144].

2.5 Selected applications in bioanalysis and diagnostics

2.5.1 Cell manipulation

Microfluidic platforms allow for effective capturing, positioning, and analysis of cells. Often, there occurs a problem in the first step of loading the cells into a channel due to cell aggregates and cell debris. To address this, Calistri et al. developed a microfluidic system that controlled the entry of individual cells into the channels through optical triggering. This can be particularly helpful in the context of analyzing tissues and tumors because it requires a step to fully dissociate the cells prior to the analysis of single cells [145]. Once supplied into the microfluidic device, cells can be captured and exposed to chemical gradients, which was exploited by Chen et al [146]. They performed dynamic single-cell studies on HeLa cells and investigated calcium signaling in response to three different agonists, supplied in a defined pattern. Moreover, it was shown that even larger organisms (e.g., the *worm C. elegans*) can be trapped and exposed to stimuli with spatial, temporal, and intensity control [147]. In another approach, tumor slices were placed within a bottomless 40-well plate, onto a porous membrane [148]. Multiplexed drug exposure was achieved through a microchannel network underneath the porous membrane, and fluorogenic live/dead cell assays were employed to determine the efficacy of treatment.

2.5.2 Cytometry and cell sorting

Analysis of a suspended cell population by sorting is a common task, and many miniaturized fluorescence-activated cell sorters have been introduced in the last decades. An experimentally interesting approach for analysis of circulating tumor cells (CTCs) from mouse blood is recently demonstrated by Hamza et al. They introduced mouse blood into a microfluidic fluorescence-activated cell sorter to withdraw and analyze the CTCs, while the CTC-depleted blood is reinjected into the mouse [149]. This facilitates long-term observation of tumor progression and treatment of the same mouse over weeks. In addition, Pritchard et al. introduced a vortex-actuated cell sorter, which combines inertial focusing of cells with thermal vapor bubbles for the sorting of fluorescently labeled cells [150]. A microsorter, where inertial focusing combined with highly accurate acoustic pulses was introduced by Zhou et al [151]. For single-cell reverse transcription loop-mediated isothermal amplification (RT-LAMP) mRNA detection, a integrated droplet sorting and merging platform was presented by Chung et al [152]. Instead of performing mRNA in a continuous droplet-based workflow, these platforms combined droplet generation/sorting with stationary droplet pairing to avoid the need for interdevice transfer or flow synchronization (Fig. 2.6B). Both sample and reagents are spotted onto a storage array and merged via electrohydrodynamic force, allowing an RT-LAMP reaction with a fluorescence readout. For a typical reaction volume of 25 μL, the possibility of performing simultaneous 676 scRT-LAMP reactions was reported. Other cytometry applications require the acquisition and analysis of images, which is not possible in commercial cytometers. This challenge of high-speed image analysis was addressed by Isozaki et al., who demonstrated rapid intelligent image-activated cell sorting [154], while Yalikun et al. emphasize the influence of deformable channel walls on image-based cytometry [155]. Image-based cell sorting in droplets was furthermore introduced by Sesen and Whyte [156].

2.5.3 Analysis of secreted compounds

Microfluidic methods also improved particularly the analysis of cell-secreted compounds since they can be accumulated in microfabricated compartments or droplets. Recently, a high-throughput single-cell platform for activity-based screening and sequencing of antibodies was introduced [157]. It aimed at IgG-secreting primary cells to characterize antibody-binding properties against soluble or membrane antigens. Two workflows were therefore required, both employ single-cell compartmentalization and sorting based on the spatial distribution of fluorescent signals within the droplets.

Chemical sensors can be harmful to cells and may induce phenotype changes, especially for stem cells. To overcome this bottleneck, a droplet-based platform was recently presented, which splits single-cell droplets for secretion analysis (Fig. 2.6A) [153]. Single stem cells were first encapsulated into droplets and produced albumin. After splitting the droplets, a cell-toxic albumin sensor was added to the daughter droplet without the cell and analyzed by fluorescence spectroscopy. Moreover, Hsu et al. embedded a hydrogel sensor together with the target cells in aqueous droplets. After the incubation and production of cytokines, droplets were de-emulsified, and the cytokine-loaded hydrogel sensors were analyzed by immunoassays. Further signal enhancement was achieved by heating and shrinkage

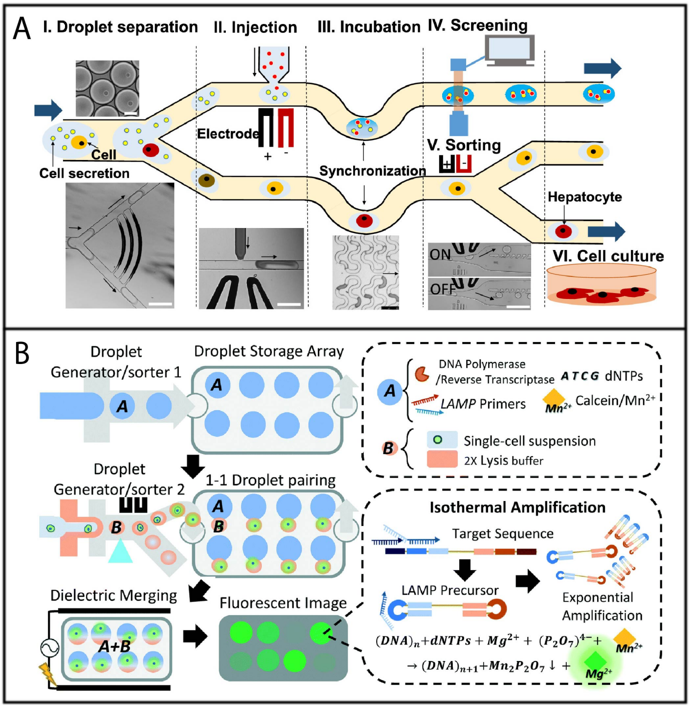

Figure 2.6: Droplet sorting platforms with multiple operational units. (A) Workflow for synchronized supernatant analysis and cell sorting. After splitting into two daughter droplets, a cell-toxic chemical sensor is injected and analyzed by fluorescence spectroscopy. The other synchronized droplet containing the cell can then be sorted according the fluorescence signal and cultivated afterward. Adapted from Sun, G.; Teng, Y.; Zhao, Z.; Cheow, L. F.; Yu, H.; Chen, C. H. Anal. Chem.2020, 92, 7915-7923 (ref [153]). Copyright 2011 American Chemical Society. (B) Schematics of a single-cell RT-LAMP assay using a Sort N' Merge platform. Droplets containing RT-LAMP reactants and single cells with lysis buffer are generated and sorted into the storage device and populate the pairing-merging wells. The paired droplets are merged by electrohydrodynamic forces allowing a RT-LAMP reaction followed by an imaging-based fluorescence measurement. Adapted from Chung, M. T.; Kurabayashi, K.; Cai, D. Lab Chip2019, 19, 2425-2434 (ref [152]), with permission of The Royal Society of Chemistry.

of the hydrogel sensors [158]. Instead of droplets, wells or valve-defined microcompartments can also be employed for secretion studies. Quantification of cytokines, aiding in assessing immune responses, was realized on a multiwell microfluidic platform with an integrated biosensor [159]. Recently, CTC isolation with efficiencies above 95% and quantification of their protein secretion was reported [160]. After the size-selective trapping of CTCs, the secretion level of granulocyte growth-stimulating factor was determined by a magnetic bead-based assay with a LOD of 1.5 $ng\ mL^{-1}$.

2.5.4 Blood cell separation

Many diagnostic methods use liquid biopsies, i.e., the sampling and analysis of blood. Microfluidic methods can be beneficial in the process, as they can be employed to separate the blood constituents, such as red and white blood cells, platelets, or lipid particles, or capture specific types of target cells such as CTCs. For example, deterministic lateral displacement (DLD) can be used to separate blood cells, platelets, and spiked rare cells by size [161]. An even more efficient separation was achieved in a two-step process, where the first separation step is based on spiral inertial microfluidics, and the second step uses DLD [162]. Sharp edges in a DLD array deform passing cells, which can be exploited for deformability studies [163], and separate by deformability [164]. Kim et al. introduced a one-step purification method for white blood cells (WBC) at high flow rates of 60 $\mu L\ min^{-1}$. It synergistically combines a slant array ridge-based WBC enrichment unit as a throughput enhancer and a slant, asymmetric lattice-based WBC washing unit as a purity enhancer [165]. In a similar context, Zhu et al. built a inertial microfluidics cube for fast extraction of white blood cells [166]. A highly integrated device for CTC capture from blood samples was recently reported by Tohner and co-workers [167]. It combines inertial focusing, microfluidic filter structures and magnetic sorting on a single platform.

A further approach for analyzing blood is performed on a rotating disc. It utilized density gradient centrifugation for complete blood counting and achieved an accuracy of >95% as compared to an automated hematology analyzer [168].

2.5.5 Point-of-care devices for the detection of biomarkers

Microfluidic systems are ideal for point-of-care applications or decentralized testing, benefiting from their footprint and portability. A wearable droplet microfluidic system was introduced for real-time sampling and measurement of tissue biochemistry [169]. A screw-driven peristaltic pump simultaneously feeds perfusate into a microdialysis probe and withdraws the resulting dialysate into the device (Fig. 2.7A). The sample-reagent mixture is immediately afterward segmented into droplets for an absorbance-based measurement of glucose and lactate. A 3D microporous hollow fiber membrane with gradient pore sizes was used to trap cells and allowed the diffusion of smaller molecules. Only a small sample amount of 5 μL was required and administered by capillary forces. By immobilizing different assay reagents to the membrane framework, biomolecules such as glucose were detected [170]. Furthermore, a three-layered hierarchically structured microchip was developed to quantify multiple biomarkers with a dynamic detection range [172]. The detection range was modulated by controlling the capture-antibodies concentration and therefore the intensity of the chemiluminescence readout signal. For the C-reactive protein, one of the three simultaneous analyzed targets, they report a dynamic range of 3.13-100 $mg\ L^{-1}$ with an LOD of 1.87 $\mu g\ mL^{-1}$. Moreover, an integrated microfluidic circuit for autonomous aptamer-based molecular detection was shown by Shin et al [173]. This device accepts whole blood samples, which are introduced into the chip together with reagents. Blood cells were removed by hydrophoresis to vacuum pillars. Only blood plasma reached the chamber, where the marker thrombin was detected. For the colorimetric analysis of biomarkers relevant to kidney disorders, a soft microfluidic system was presented (Fig. 2.7B) [171]. It is highly attractive because it passively collects sweat, which is noninvasive and easy for patient use. In addition, this epidermal applied device can detect creatinine and urea in physiologically relevant levels with adapted colorimetric assays. Moreover, viability assessment of donor-kidneys improves the outcome of transplantations. Therefore, a portable real-time analysis platform for microdialysate was developed to monitor tissue metabolites [174]. A needle-based biosensor detects glucose and lactate and transmits data via Bluetooth to a smartphone application.

Cunningham and co-workers developed an active capture and digital counting assays with a self-powered microfluidic cartridge for detection of protein biomarkers by immunoassays [175]. Besides portability, sensitivity of the method is important to detect low-concentrated biomarkers. Tokeshi and co-workers presented very sensitive immunoassays for disease biomarkers, where the capture antibodies are immobilized at the channel walls to improve the limit of the detection [176].

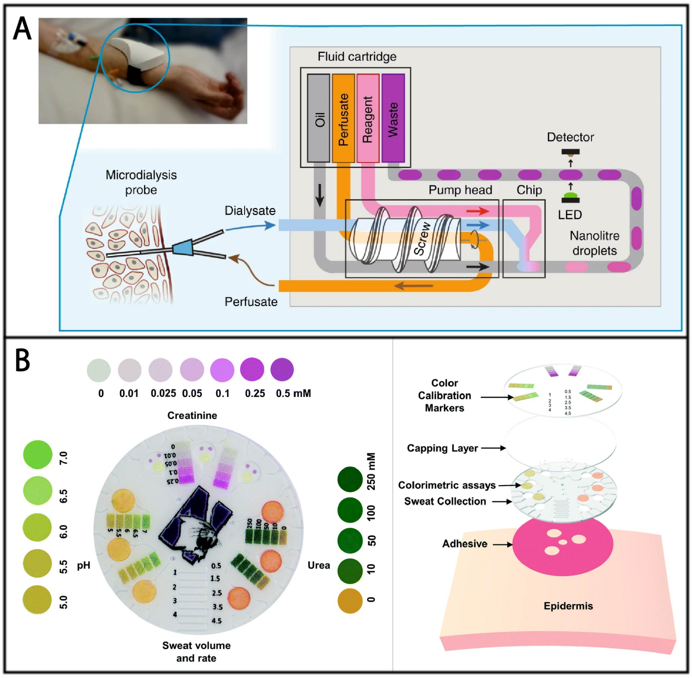

Figure 2.7: Portable microfluidic device for point-of-care diagnostics.(A) A screw-driven peristaltic pump simultaneously feeds perfusate into a microdialysis probe and withdraws the resulting dialysate into the device. The dialysate is then mixed with reagents before droplet formation and analysis, e.g., of glucose. The result is transferred via Bluetooth to an external device. Adapted with permission from Macmillan Publishers Ltd.: NATURE, Nightingale, A. M.; Leong, C. L.; Burnish, R. A.; Hassan, S. U.; Zhang, Y.; Clough, G. F.; Boutelle, M. G.; Voegeli, D.; Niu, X. Nat. Commun. 2019, 10, 1-11 (ref [169]). Copyright 2012 under a Creative Commons Attribution 4.0 International License (https://creativecommons.org/licenses/by/4.0/) (B) Overview of an epidermal microfluidic sweat sensor, allowing the quantitative colorimetric analysis of creatinine and urea, which are relevant biomarkers for kidney disorders. Adapted from Zhang, Y.; Guo, H.; Kim, S. B.; Wu, Y.; Ostojich, D.; Park, S. H.; Wang, X.; Weng, Z.; Li, R.; Bandodkar, A. J.; et al. Lab Chip2019, 19, 1545-1555 (ref [171]), with permission of The Royal Society of Chemistry.

2.5.6 Extracellular vesicles (EV)

Exosomes secreted by cells are considered as valuable biomarkers to diagnose various diseases, such as cancer, as well as potential drug delivery vehicles [177]. They contain surface markers, proteins, and RNAs of the cell of origin and are easily accessible, e.g., by liquid biopsy, since they are present in blood, urine, and saliva. However, EVs must be enriched and separated from these body fluids for further analysis. Nagrath and co-workers utilized a microdevice conjugated with two melanoma-specific antibodies, MCAM and MCSP, to capture melanoma cycling tumor cells and exosomes from whole blood [178]. By combining in situ enzymatic amplification of optical deposits and surface plasmon resonance, exosome populations were analyzed from blood samples of patients diagnosed with Alzheimer's disease. Compared to other such platforms, several parameters were optimized allowing a highly sensitive multiplexed detection [179]. Mathew et al. developed a prostate cancer cell-line EV assay in a microfluidic device with the ability to detect the same EV concentration range that occurs in whole blood by combining redox cycling on nanointerdigitated electrodes, an enzymatic reaction, and a sandwich immunoassay [180]. Another group presented a prostate cancer diagnosis technique by in situ detection of exosomal miRNAs and surface proteins using molecular beacons and antibodies [181].

Liu et al. enriched extracellular vesicles labeled with fluorescence aptamers using thermophoresis and classified them by a linear discriminant analysis algorithm. Thus, surface protein profiles of EVs in 232 serum samples were obtained and 6 cancer types at stage I to IV uncovered with a sensitivity of 95% for stage I cancers [182]. By labeling EVs with DNA-aptamers followed by λ-DNA mediated viscoelastic microfluidics, single EVs were analyzed in 2D based on size and marker expression in a microfluidic coflow device. Thus, EV subpopulations of breast cell lines and -cancer patients with different HER2 expression could be analyzed using a machine learning algorithm [183].

It has been a great challenge to separate particles with nanometer sizes. Several researchers developed microfluidic methods that effectively overcome the difficulties. For instance, Zhang and Lyden provided a detailed protocol for asymmetric-flow field-flow fractionation (AF4), suitable for the separation and further characterization of small extracellular vesicles such as exomeres and exosomes. A semipermissive membrane integrated into the bottom wall allows for the filtration of nanoparticles below the cutoff size. Samples with larger particle range can be separated solely due to differences in their diffusion coefficients. Therefore, AF4 provides a label-free, gentle, and rapid way to isolate extracellular nanoparticles at a resolution of 1 *nm* in 1 *h* [184]. Further, a nanoparticle tracking analysis was coupled to AF4 enabling online separation and counting of 50 to 200 *nm* sized polystyrene particles [185]. Another label-free method to separate exosome-like particles was accomplished by using a so-called FerroChip. The separation principle is based on the ferrohydrodynamics of nanoscale particles in a ferrofluid and allowed to separate 30-150 *nm* sized particles with a recovery rate of 94.3% and a purity of 87.9% [186]. Baba and co-workers employed electroosmotic flow-driven lateral displacement to separate extracellular vesicles in an array of micro- and nanopillars [187].

2.5.7 Identification of pathogens and antibiotic susceptibility testing

Rapid test on antibiotic susceptibility of pathogens can aid medical doctors to select the best drug mixture for bacterial infections. Increased throughput is achieved by parallelization of tests, as shown in a new device capable of screening four bacteria/drug combinations simultaneously [188]. After bacterial cell encapsulation, the droplets were transferred to four integrated microdroplet-arrays. Each array hosting over 8000 docking sites, in which proliferation was assessed. It offers a significantly faster assay time of 30 *min* compared to 16-24 *h* of conventional methods. Another microfluidic device allowed a rapid classification and susceptibility testing at the single-cell level, where pathogens were loaded into channels by capillary forces [189]. These capabilities were showcased with clinical samples, where pathogens are identified based on size and shape, before testing antibiotic response within approximately 30 *min*. Furthermore, Coudron et al. developed a digital microfluidic platform for automated immunoassays, taking advantage of a fully magnetic separation process for rapid detection [190]. The device is compatible with electrowetting-coupled air samplers and performs automatic immunoassays completed in between 6 to 10 *min*. For studying the interspecies interactions and environmental dependencies of microbial communities, a droplet microfluidic chip was presented, where color-coded species droplets are randomly merged in microwells [191]. Phenotyping was performed via fluorescent protein expression and respiration driven reduction of resazurin. This so-called kChip was employed to screen 100'000 multispecies communities comprising of up to 19 soil isolates to identify sets for the growth promotion of a model plant symbionts (Fig. 2.8B).

A new promising class of antimicrobials are polypeptides, which possess mem-

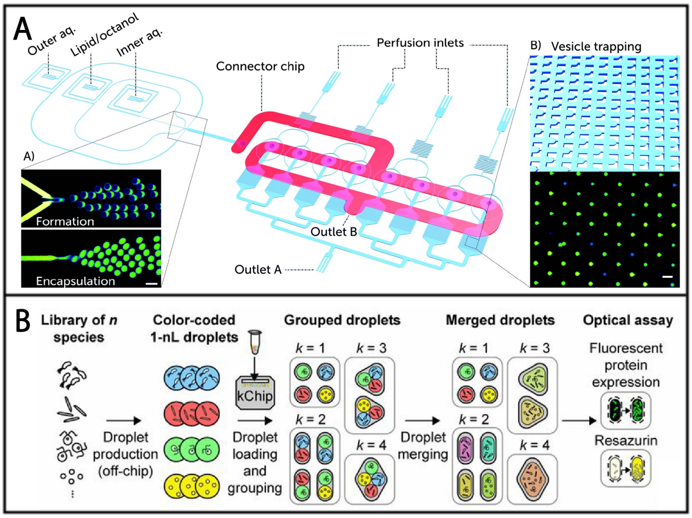

Figure 2.8: Highly parallel analysis of vesicles and droplets. (A) Microfluidic platform for testing the efficacy of membrane-active drugs on individual lipid vesicles. The platform consists of a vesicle formation module and 8 separate chambers each encompassing an array of 372 vesicle traps. Evaluation was carried out by fluorescence imaging. Adapted from Al Nahas, K.; Cama, J.; Schaich, M.; Hammond, K.; Deshpande, S.; Dekker, C.; Ryadnov, M. G.; Keyser, U. F. A Lab Chip2019, 19, 837-844 (ref [192]), published by the Royal Society of Chemistry under a Creative Commons Attribution 3.0 Unported License (https://creativecommons.org/licenses/by/3.0/). (B) Massive parallel construction and screening of microbial communities by merging droplet. The content of the droplets is characterized by color codes. Community phenotypes can be tracked via optical assays, including fluorescent protein expression and respiration-driven reduction of resazurin to the fluorescent product resorufin. Adapted with permission from Proceedings of the National Academy of Sciences USA Kehe, J.; Kulesa, A.; Ortiz, A.; Ackerman, C. M.; Thakku, S. G.; Sellers, D.; Kuehn, S.; Gore, J.; Friedman, J.; Blainey, P. C. Proc. Natl. Acad. Sci. U.S.A.2019, 116, 12804-12809 (ref [191]).

branolytic properties. To estimate these properties, a platform for producing and trapping of lipid vesicles in separated chambers was developed [192]. The dye-filled vesicles were continuously exposed to different concentrations of Cecropin B, an antimicrobial agent, and the time dependent effect could be estimated via a decrease in fluorescence intensity (Fig. 2.8A).

2.5.8 Virus detection

The recent pandemic caused by the severe acute respiratory syndrome coronavirus 2 (SARS-CoV-2) showed the importance for sensitive, rapid, and cheap viral testing methods and their availability especially during a pandemic. Microfluidic technology can make a significant contribution to the needs, as demonstrated by several recent studies. Ackerman et al. developed a CRISPR-based multiplexed platform for the detection of up to 169 human associated viruses [193]. The miniaturization of the platform reduces reagent cost by up to 300 times, which makes it affordable for high-throughput and wide coverage testing of patients' samples. Alternatively, a highly sensitive and rapid CRISPR-based platform was established, which has a turnaround time of approximately 50 *min* from sample-to-answer [194]. In contrast, Lin et al. used antigens combined with a fluorescent readout to achieve a turnaround time of less than 15 *min* [195]. The PRESCIENT platform is in an integrated microfluidic platform for the rapid testing of virus neutralizing antibodies [196]. The susceptibility of the virus to the antibody is performed at the single-cell level. A different approach to inhibit virus spread is the disruption of its life cycle. Virus capsids, the protein shell encapsulating its genetic material, were studied by a multicycle resistive-pulse sensing platform [197]. The viral particle is driven back and forth through four serial nanopores, each time giving a detection signal. The time between the nanopores is correlated to the size of the viral particle. This method discriminates viral particle sized up to a one time difference and provides a strong tool to study the viral self-assembly process.

Especially in a global pandemic, it is important that viral detection can be performed rapidly on site, preferentially on a POC device. Therefore, Hedde et al. developed a modular microarray imaging platform for the highly selective and specific detection of viruses such as SARS-CoV-2 [198]. Their developed platform shows a similar sensitivity than commonly used plate readers but is 100 times less expensive. An alternative point-of-care device, developed by McRae et al., is able to define the severity of the patient's disease course facilitating decision making in clinical settings [199]. Jiang et al. developed a microfluidic POC platform for the virus detection offering both the storage and delivery of reagents for virus lysis as well as RNA extraction. The system achieved a similar level of sensitivity in RNA enrichment compared to commercially available extraction kits without any laboratory equipment needed [200]. Additionally, more and more POC devices use a smartphone as a user interface. A passive and self-driven microfluidic platform was developed which enables the highly sensitive readout with integrated colorimetric sensors [201]. The results are automatically sent to the connected smartphone. Moreover, Minagawa et al. developed an imaging platform for the digital detection of the influenza virus [202]. The optical readout is based on evanescent field illumination, and single viral particles can be detected with a simple smartphone camera. Lately, an autonomous POC device was reported for rapid HIV detection in whole blood [203]. It utilized a novel RT-LAMP assay whose reagents can be dried and stored for 3 weeks at room temperature. After amplification, the products were visualized by a lateral flow immunoassay, with a sensitivity of 3×10^5 virus copies per reaction.

2.6 Conclusion and outlook

Research in microfluidics has various aspects; it requires development of the technology, such as fabrication or investigation of suitable materials and coatings, invention of methods to manipulate fluids and samples, adaptation of microscale systems to analytical detection methods, as well as development of assays suitable for application in small volumes. All these fields have further advanced in the last 2 years and resulted in exciting studies and findings.

For example, numerous available methods to capture individual cells, by passive modules or external forces, e.g., acoustic, electric, or magnetic forces, have opened new opportunities for single-cell analysis beyond just complementing standard methods. The immobilization of selected single cells combined with precise manipulation of the microenvironment and the possibility to keep cells in a small observation volume allowed for monitoring of single-cell response, analysis of single-cell lysates, or quantification of secreted compounds at a large throughput. Analytically challenging areas such as the analysis of ultrarare circulating tumor cells in blood samples, or single cells derived from solid tumors, are benefiting greatly from these new methods.

Due to their small footprint and possibilities of integration, microfluidic platforms are valuable tools for diagnostic measurements at the point of care. This can substitute the need for fully equipped laboratories and provide rapid test results that support the selection of a therapy for a patient, e.g., choice of antibiotics to treat an infection, as well as disease monitoring to evaluate the chosen therapy. Point-of-care devices should be extremely robust and easy to use, so that user-errors can be excluded. Likewise, the result should be clear and interpretable and based on a simple analytical method, e.g., a colorimetric assay or smartphone-assisted detection. However, significant optimization is still needed before widespread commercialization and use in low-resource settings becomes feasible. The urgent need for rapid tests of viral infections will positively stimulate research toward improved robustness and reproducibility as well as simple, user-friendly operation.

The interdisciplinary nature of microfluidics requires synergistic efforts of researchers from different backgrounds and with different expertise. Such collaborations have become more and more successful in recent years, and the increasing acceptance of microfluidics in the life sciences (i.e., beyond engineering and method development) will certainly push the current trend forward in near future.

2.7 Acknowledgments

We thank Dr. Darius Rackus (ETH Zurich, Switzerland) for proofreading. Financial support by the Swiss National Science Foundation (NCCR Molecular Systems Engineering) and the ERANet-RUS Program (Project TARQUS) is gratefully acknowledged.

2.8 References

[1] A. Manz, N. Graber, and H. Widmer, «Miniaturized total chemical analysis systems: a novel concept for chemical sensing», Sensors and Actuators B: Chemical **1**, 244–248 (1990).

[2] C. T. Culbertson, T. G. Mickleburgh, S. A. Stewart-James, K. A. Sellens, and M. Pressnall, «Micro total analysis systems: fundamental advances and biological applications», Analytical Chemistry **86**, 95–118 (2014).

[3] D. E. Patabadige, S. Jia, J. Sibbitts, J. Sadeghi, K. Sellens, and C. T. Culbertson, «Micro total analysis systems: fundamental advances and applications», Analytical Chemistry **88**, 320–338 (2016).

[4] A. W. Auner, K. M. Tasneem, D. A. Markov, L. J. McCawley, and M. S. Hutson, «Chemical-pdms binding kinetics and implications for bioavailability in microfluidic devices», Lab on a Chip **19**, 864–874 (2019).

[5] M. Lenz, B. Sebastian, and P. S. Dittrich, «Formation of single micro- and nanowires with extreme aspect ratios in microfluidic channels», Small **15**, 1901547 (2019).

[6] R. Geczy, D. Sticker, N. Bovet, U. O. Häfeli, and J. P. Kutter, «Chloroform compatible, thiol-ene based replica molded micro chemical devices as an alternative to glass microfluidic chips», Lab on a Chip **19**, 798–806 (2019).

[7] R. Z. Shafagh, D. Decrop, K. Ven, A. Vanderbeke, R. Hanusa, J. Breukers, G. Pardon, T. Haraldsson, J. Lammertyn, and W. van der Wijngaart, «Reaction injection molding of hydrophilic-in-hydrophobic femtolitre-well arrays», Microsystems and Nanoengineering **5**, 25 (2019).

[8] H. Sun, C. W. Chan, Y. Wang, X. Yao, X. Mu, X. Lu, J. Zhou, Z. Cai, and K. Ren, «Reliable and reusable whole polypropylene plastic microfluidic devices for a rapid, low-cost antimicrobial susceptibility test», Lab on a Chip **19**, 2915–2924 (2019).

[9] Z. B. Qi, L. Xu, Y. Xu, J. Zhong, A. Abedini, X. Cheng, and D. Sinton, «Disposable silicon-glass microfluidic devices: precise, robust and cheap», Lab on a Chip **18**, 3872–3880 (2018).

[10] F. Kotz, P. Risch, K. Arnold, S. Sevim, J. Puigmartí-Luis, A. Quick, M. Thiel, A. Hrynevich, P. D. Dalton, D. Helmer, and B. E. Rapp, «Fabrication of arbitrary three-dimensional suspended hollow microstructures in transparent fused silica glass», Nature Communications **10**, 1439 (2019).

[11] C. Shen, Y. Li, Y. Wang, and Q. Meng, «Non-swelling hydrogel-based microfluidic chips», Lab on a Chip **19**, 3962–3973 (2019).

[12] B. Zhang, B. F. L. Lai, R. Xie, L. D. Huyer, M. Montgomery, and M. Radisic, «Microfabrication of angiochip, a biodegradable polymer scaffold with microfluidic vasculature», Nature Protocols **13**, 1793–1813 (2018).

[13] A. Andar, M. S. Hasan, V. Srinivasan, M. Al-Adhami, E. Gutierrez, D. Burgenson, X. Ge, L. Tolosa, Y. Kostov, and G. Rao, «Wood microfluidics», Analytical Chemistry **91**, 11004–11012 (2019).

[14] X. Hou, J. Li, A. B. Tesler, Y. Yao, M. Wang, L. Min, Z. Sheng, and J. Aizenberg, «Dynamic air/liquid pockets for guiding microscale flow», Nature Communications **9**, 733 (2018).

[15] S. M. Cramer, T. S. Larson, and M. R. Lockett, «Tissue papers: leveraging paper-based microfluidics for the next generation of 3d tissue models», Analytical Chemistry **91**, 10916–10926 (2019).

[16] T. Ozer, C. McMahon, and C. S. Henry, «Advances in paper-based analytical devices», Annual Review of Analytical Chemistry **13**, 1–25 (2020).

[17] S. Paik, G. Kim, S. Chang, S. Lee, D. Jin, K. Y. Jeong, I. S. Lee, J. Lee, H. Moon, J. Lee, K. Chang, S. S. Choi, J. Moon, S. Jung, S. Kang, W. Lee, H. J. Choi, H. Choi, H. J. Kim, J. H. Lee, J. Cheon, M. Kim, J. Myoung, H. G. Park, and W. Shim, «Near-field sub-diffraction photolithography with an elastomeric photomask», Nature Communications **11**, 805 (2020).

[18] T. Trantidou, M. S. Friddin, K. B. Gan, L. Han, G. Bolognesi, N. J. Brooks, and O. Ces, «Mask-free laser lithography for rapid and low-cost microfluidic device fabrication», Analytical Chemistry **90**, 13915–13921 (2018).

[19] U. M. Sonmez, S. Coyle, R. E. Taylor, and P. R. LeDuc, «Polycarbonate heat molding for soft lithography», Small **16**, 2000241 (2020).

[20] O. Vanderpoorten, Q. Peter, P. K. Challa, U. F. Keyser, J. Baumberg, C. F. Kaminski, and T. P. Knowles, «Scalable integration of nano-, and microfluidics with hybrid two-photon lithography», Microsystems and Nanoengineering **5**, 40 (2019).

[21] A. T. Alsharhan, R. Acevedo, R. Warren, and R. D. Sochol, «3d microfluidics: via cyclic olefin polymer-based in situ direct laser writing», Lab on a Chip **19**, 2799–2810 (2019).

[22] F. Mayer, S. Richter, J. Westhauser, E. Blasco, C. Barner-Kowollik, and M. Wegener, «Multimaterial 3d laser microprinting using an integrated microfluidic system», Science Advances **5**, 1–8 (2019).

[23] V. Romanov, R. Samuel, M. Chaharlang, A. R. Jafek, A. Frost, and B. K. Gale, «Fdm 3d printing of high-pressure, heat-resistant, transparent microfluidic devices», Analytical Chemistry **90**, 10450–10456 (2018).

[24] M. J. Beauchamp, A. V. Nielsen, H. Gong, G. P. Nordin, and A. T. Woolley, «3d printed microfluidic devices for microchip electrophoresis of preterm birth biomarkers», Analytical Chemistry **91**, 7418–7425 (2019).

[25] A. D. Castiaux, C. W. Pinger, E. A. Hayter, M. E. Bunn, R. S. Martin, and D. M. Spence, «Polyjet 3d-printed enclosed microfluidic channels without photocurable supports», Analytical Chemistry **91**, 6910–6917 (2019).

[26] F. Li, N. P. MacDonald, R. M. Guijt, and M. C. Breadmore, «Multimaterial 3d printed fluidic device for measuring pharmaceuticals in biological fluids», Analytical Chemistry **91**, 1758–1763 (2019).

[27] J. Zhu, Q. Zhang, T. Yang, Y. Liu, and R. Liu, «3d printing of multiscalable structures via high penetration near-infrared photopolymerization», Nature Communications **11**, 3462 (2020).

[28] J. Li, T. Kong, J. Yu, K. H. Lee, Y. H. Tang, K. W. Kwok, J. T. Kim, and H. C. Shum, «Electrocoiling-guided printing of multiscale architectures at single-wavelength resolution», Lab on a Chip **19**, 1953–1960 (2019).

[29] R. Yuan, J. Lee, H. W. Su, E. Levy, T. Khudiyev, J. Voldman, and Y. Fink, «Microfluidics in structured multimaterial fibers», Proceedings of the National Academy of Sciences of the United States of America **115**, E10830–E10838 (2018).

[30] W. Li, M. Yu, J. Sun, K. Mochizuki, S. Chen, H. Zheng, J. Li, S. Yao, H. Wu, B. S. Ong, S. Kawata, Z. Wang, and K. Ren, «Crack engineering for the construction of arbitrary hierarchical architectures», Proceedings of the National Academy of Sciences of the United States of America **116**, 23909–23914 (2019).

[31] N. Xiang, R. Zhang, Y. Han, and Z. Ni, «A multilayer polymer-film inertial microfluidic device for high-throughput cell concentration», Analytical Chemistry **91**, 5461–5468 (2019).

[32] Y. Lee, J. W. Choi, J. Yu, D. Park, J. Ha, K. Son, S. Lee, M. Chung, H. Y. Kim, and N. L. Jeon, «Microfluidics within a well: an injection-molded plastic array 3d culture platform», Lab on a Chip **18**, 2433–2440 (2018).

[33] S. Lee, J. Lim, J. Yu, J. Ahn, Y. Lee, and N. L. Jeon, «Engineering tumor vasculature on an injection-molded plastic array 3d culture (impact) platform», Lab on a Chip **19**, 2071–2080 (2019).

[34] J. H. Day, T. M. Nicholson, X. Su, T. L. V. Neel, I. Clinton, A. Kothandapani, J. Lee, M. H. Greenberg, J. K. Amory, T. J. Walsh, C. H. Muller, O. E. Franco, C. R. Jefcoate, S. E. Crawford, J. S. Jorgensen, and A. B. Theberge, «Injection molded open microfluidic well plate inserts for user-friendly coculture and microscopy», Lab on a Chip **20**, 107–119 (2020).

[35] J. S. del Río, O. Y. Henry, P. Jolly, and D. E. Ingber, «An antifouling coating that enables affinity-based electrochemical biosensing in complex biological fluids», Nature Nanotechnology **14**, 1143–1149 (2019).

[36] J. Liu, L. Ye, Y. Sun, M. Hu, F. Chen, S. Wegner, V. Mailänder, W. Steffen, M. Kappl, and H. J. Butt, «Elastic superhydrophobic and photocatalytic active films used as blood repellent dressing», Advanced Materials **32**, 1908008 (2020).

[37] Y. Xia, V. Adibnia, R. Huang, F. Murschel, J. Faivre, G. Xie, M. Olszewski, G. D. Crescenzo, W. Qi, Z. He, R. Su, K. Matyjaszewski, and X. Banquy, «Biomimetic bottlebrush polymer coatings for fabrication of ultralow fouling surfaces», Angewandte Chemie - International Edition **58**, 1308–1314 (2019).

[38] K. Piironen, M. Haapala, V. Talman, P. Järvinen, and T. Sikanen, «Cell adhesion and proliferation on common 3d printing materials used in stereolithography of microfluidic devices», Lab on a Chip **20**, 2372–2382 (2020).

[39] W. Liu, K. Han, M. Sun, and J. Wang, «Enhancement and control of neuron adhesion on polydimethylsiloxane for cell microengineering using a functionalized triblock polymer», Lab on a Chip **19**, 3162–3167 (2019).

[40] Z. Liu, Z. Zhou, S. Zhang, L. Sun, Z. Shi, Y. Mao, K. Liu, and T. H. Tao, «'print-to-pattern': silk-based water lithography», Small **14**, 1802953 (2018).

[41] A. Shakeri, S. M. Imani, E. Chen, H. Yousefi, R. Shabbir, and T. F. Didar, «Plasma-induced covalent immobilization and patterning of bioactive species in microfluidic devices», Lab on a Chip **19**, 3104–3115 (2019).

[42] P. Thurgood, J. Y. Zhu, N. Nguyen, S. Nahavandi, A. R. Jex, E. Pirogova, S. Baratchi, and K. Khoshmanesh, «A self-sufficient pressure pump using latex balloons for microfluidic applications», Lab on a Chip **18**, 2730–2740 (2018).

[43] J. Park and J. K. Park, «Integrated microfluidic pumps and valves operated by finger actuation», Lab on a Chip **19**, 2973–2977 (2019).

[44] E. Sweet, R. Mehta, Y. Xu, R. Jew, R. Lin, and L. Lin, «Finger-powered fluidic actuation and mixing: via multijet 3d printing», Lab on a Chip **20**, 3375–3385 (2020).

[45] S. Yue, F. Lin, Q. Zhang, N. Epie, S. Dong, X. Shan, D. Liu, W. K. Chu, Z. Wang, and J. Bao, «Gold-implanted plasmonic quartz plate as a launch pad for laser-driven photoacoustic microfluidic pumps», Proceedings of the National Academy of Sciences of the United States of America **116**, 6580–6585 (2019).

[46] J. Seo, C. Wang, S. Chang, J. Park, and W. Kim, «A hydrogel-driven microfluidic suction pump with a high flow rate», Lab on a Chip **19**, 1790–1796 (2019).

[47] H. Chen, T. Ran, Y. Gan, J. Zhou, Y. Zhang, L. Zhang, D. Zhang, and L. Jiang, «Ultrafast water harvesting and transport in hierarchical microchannels», Nature Materials **17**, 935–942 (2018).

[48] Z. Li, Y. Seo, O. Aydin, M. Elhebeary, R. D. Kamm, H. Kong, and M. A. T. Saif, «Biohybrid valveless pump-bot powered by engineered skeletal muscle», Proceedings of the National Academy of Sciences of the United States of America **116**, 1543–1548 (2019).

[49] B. Aksoy, N. Besse, R. J. Boom, B. J. Hoogenberg, M. Blom, and H. Shea, «Latchable microfluidic valve arrays based on shape memory polymer actuators», Lab on a Chip **19**, 608–617 (2019).

[50] S. H. Yang, J. Park, J. R. Youn, and Y. S. Song, «Programmable microfluidic logic device fabricated with a shape memory polymer», Lab on a Chip **18**, 2865–2872 (2018).

[51] M. M. Aeinehvand, L. Weber, M. Jiménez, A. Palermo, M. Bauer, F. F. Loeffler, F. Ibrahim, F. Breitling, J. Korvink, M. Madou, D. Mager, and S. O. Martínez-Chapa, «Elastic reversible valves on centrifugal microfluidic platforms», Lab on a Chip **19**, 1090–1100 (2019).

[52] Y. Chen, M. Shen, Y. Zhu, and Y. Xu, «A novel electromagnet-triggered pillar valve and its application in immunoassay on a centrifugal platform», Lab on a Chip **19**, 1728–1735 (2019).

[53] Y. Kazoe, Y. Pihosh, H. Takahashi, T. Ohyama, H. Sano, K. Morikawa, K. Mawatari, and T. Kitamori, «Femtoliter nanofluidic valve utilizing glass deformation», Lab on a Chip **19**, 1686–1694 (2019).

[54] J. Avesar, Y. Blinder, H. Aktin, A. Szklanny, D. Rosenfeld, Y. Savir, M. Bercovici, and S. Levenberg, «Nanoliter cell culture array with tunable chemical gradients», Analytical Chemistry **90**, 7480–7488 (2018).

[55] R. Watanabe, T. Komatsu, S. Sakamoto, Y. Urano, and H. Noji, «High-throughput single-molecule bioassay using micro-reactor arrays with a concentration gradient of target molecules», Lab on a Chip **18**, 2849–2853 (2018).

[56] J. Wu, A. Kumar-Kanojia, S. Hombach-Klonisch, T. Klonisch, and F. Lin, «A radial microfluidic platform for higher throughput chemotaxis studies with individual gradient control», Lab on a Chip **18**, 3855–3864 (2018).

[57] S. Kim, F. Masum, J. K. Kim, H. J. Chung, and J. S. Jeon, «On-chip phenotypic investigation of combinatory antibiotic effects by generating orthogonal concentration gradients», Lab on a Chip **19**, 959–973 (2019).

[58] P. Perrodin, C. Sella, and L. Thouin, «Electrochemical generation of steady-state linear concentration gradients within microfluidic

channels perpendicular to the flow field», Analytical Chemistry **92**, 7699–7707 (2020).

[59] A. Enders, I. G. Siller, K. Urmann, M. R. Hoffmann, and J. Bahnemann, «3d printed microfluidic mixers-a comparative study on mixing unit performances», Small **15**, 1804326 (2019).

[60] Q. Xiong, C. Y. Lim, J. Ren, J. Zhou, K. Pu, M. B. Chan-Park, H. Mao, Y. C. Lam, and H. Duan, «Magnetic nanochain integrated microfluidic biochips», Nature Communications **9**, 1743 (2018).

[61] M. R. Rasouli and M. Tabrizian, «An ultra-rapid acoustic micromixer for synthesis of organic nanoparticles», Lab on a Chip **19**, 3316–3325 (2019).

[62] N. H. A. Le, H. Deng, C. Devendran, N. Akhtar, X. Ma, C. Pouton, H. K. Chan, A. Neild, and T. Alan, «Ultrafast star-shaped acoustic micromixer for high throughput nanoparticle synthesis», Lab on a Chip **20**, 582–591 (2020).

[63] Y. Zhang, C. Devendran, C. Lupton, A. D. Marco, and A. Neild, «Versatile platform for performing protocols on a chip utilizing surface acoustic wave (saw) driven mixing», Lab on a Chip **19**, 262–271 (2019).

[64] Y. Y. Zhang, D. A. Gregory, Y. Y. Zhang, P. J. Smith, S. J. Ebbens, and X. Zhao, «Reactive inkjet printing of functional silk stirrers for enhanced mixing and sensing», Small **15**, 1804213 (2019).

[65] N. Xiang, Q. Li, and Z. Ni, «Combining inertial microfluidics with cross-flow filtration for high-fold and high-throughput passive volume reduction», Analytical Chemistry **92**, 6770–6776 (2020).

[66] X. Qiu, J. A. Lombardo, T. M. Westerhof, M. Pennell, A. Ng, H. Alshetaiwi, B. M. Luna, E. L. Nelson, K. Kessenbrock, E. E. Hui, and J. B. Haun, «Microfluidic filter device with nylon mesh membranes efficiently dissociates cell aggregates and digested tissue into single cells», Lab on a Chip **18**, 2776–2786 (2018).

[67] F. A. Hansen, D. Sticker, J. P. Kutter, N. J. Petersen, and S. Pedersen-Bjergaard, «Nanoliter-scale electromembrane extraction and enrichment in a microfluidic chip», Analytical Chemistry **90**, 9322–9329 (2018).

[68] M. Etienne, T. X. H. Le, T. Nasir, and G. Herzog, «Electrochemical filter to remove oxygen interference locally, rapidly, and temporarily for sensing applications», Analytical Chemistry **92**, 7425–7429 (2020).

[69] S. H. P. Thanthri, C. L. Ward, M. A. Cornejo, and T. H. Linz, «Simultaneous preconcentration and separation of native protein variants using thermal gel electrophoresis», Analytical Chemistry **92**, 6741–6747 (2020).

[70] S. Jeeawoody, K. A. Yamauchi, A. Su, and A. E. Herr, «Laterally aggregated polyacrylamide gels for immunoprobed isoelectric focusing», Analytical Chemistry **92**, 3180–3188 (2020).

[71] B. Gumuscu and A. E. Herr, «Separation-encoded microparticles for single-cell western blotting», Lab on a Chip **20**, 64–73 (2020).

[72] S. Lin, X. Zhi, D. Chen, F. Xia, Y. Shen, J. Niu, S. Huang, J. Song, J. Miao, D. Cui, and X. Ding, «A flyover style microfluidic chip for highly purified magnetic cell separation», Biosensors and Bioelectronics **129**, 175–181 (2019).

[73] M. Solsona, A. E. Nieuwelink, F. Meirer, L. Abelmann, M. Odijk, W. Olthuis, B. M. Weckhuysen, and A. van den Berg, «Magnetophoretic sorting of single catalyst particles», Angewandte Chemie - International Edition **57**, 10589–10594 (2018).

[74] M. Schlenk, M. Drechsler, M. Karg, W. Zimmermann, M. Trebbin, and S. Förster, «Splitting and separation of colloidal streams in sinusoidal microchannels», Lab on a Chip **18**, 3163–3171 (2018).

[75] V. Bacheva, F. Paratore, S. Rubin, G. V. Kaigala, and M. Bercovici, «Tunable bidirectional electroosmotic flow for diffusion-based separations», Angewandte Chemie - International Edition **59**, 12894–12899 (2020).

[76] Y. Zhou, Z. Ma, M. Tayebi, and Y. Ai, «Submicron particle focusing and exosome sorting by wavy microchannel structures within viscoelastic fluids», Analytical Chemistry **91**, 4577–4584 (2019).

[77] D. Kim, A. Echelmeier, J. C. Villarreal, S. Gandhi, S. Quintana, A. Egatz-Gomez, and A. Ros, «Electric triggering for enhanced control of droplet generation», Analytical Chemistry **91**, 9792–9799 (2019).

[78] M. Shojaeian, F. X. Lehr, H. U. Göringer, and S. Hardt, «On-demand production of femtoliter drops in microchannels and their use as biological reaction compartments», Analytical Chemistry **91**, 3484–3491 (2019).

[79] K. Totlani, J. W. Hurkmans, W. M. V. Gulik, M. T. Kreutzer, and V. V. Steijn, «Scalable microfluidic droplet on-demand generator for non-steady operation of droplet-based assays», Lab on a Chip **20**, 1398–1409 (2020).

[80] C. L. Delley and A. R. Abate, «Microfluidic particle zipper enables controlled loading of droplets with distinct particle types», Lab on a Chip **20**, 2465–2472 (2020).

[81] M. Jeyhani, R. Thevakumaran, N. Abbasi, D. K. Hwang, and S. S. Tsai, «Microfluidic generation of all-aqueous double and triple emulsions», Small **16**, 1906565 (2020).

[82] D. Ferraro, M. Serra, D. Filippi, L. Zago, E. Guglielmin, M. Pierno, S. Descroix, J. L. Viovy, and G. Mistura, «Controlling the distance of highly confined droplets in a capillary by interfacial tension for merging on-demand», Lab on a Chip **19**, 136–146 (2019).

[83] V. Bussiere, A. Vigne, A. Link, J. McGrath, A. Srivastav, J. C. Baret, and T. Franke, «High-throughput triggered merging of surfactant-stabilized droplet pairs using traveling surface acoustic waves», Analytical Chemistry **91**, 13978–13985 (2019).

[84] C. W. Pan, D. G. Horvath, S. Braza, T. Moore, A. Lynch, C. Feit, and P. Abbyad, «Sorting by interfacial tension (sift): label-free selection of live cells based on single-cell metabolism», Lab on a Chip **19**, 1344–1351 (2019).

[85] M. Li, M. V. Zee, K. Goda, and D. D. Carlo, «Size-based sorting of hydrogel droplets using inertial microfluidics», Lab on a Chip **18**, 2575–2582 (2018).

[86] S. T. Hung, S. Mukherjee, and R. Jimenez, «Enrichment of rare events using a multi-parameter high throughput microfluidic droplet sorter», Lab on a Chip **20**, 834–843 (2020).

[87] Z. Toprakcioglu, P. K. Challa, A. Levin, and T. P. Knowles, «Observation of molecular self-assembly events in massively parallel microdroplet arrays», Lab on a Chip **18**, 3303–3309 (2018).

[88] C. M. O'Keefe, A. M. Kaushik, and T. H. Wang, «Highly efficient real-time droplet analysis platform for high-throughput interrogation of dna sequences by melt», Analytical Chemistry **91**, 11275–11282 (2019).

[89] A. Z. Nelson, B. Kundukad, W. K. Wong, S. A. Khan, and P. S. Doyle, «Embedded droplet printing in yield-stress fluids», Proceedings of the National Academy of Sciences of the United States of America **117**, 5671–5679 (2020).

[90] J. G. Xu, M. S. Huang, H. F. Wang, and Q. Fang, «Forming a large-scale droplet array in a microcage array chip for high-throughput screening», Analytical Chemistry **91**, 10757–10763 (2019).

[91] L. Nan, M. Y. A. Lai, M. Y. H. Tang, Y. K. Chan, L. L. M. Poon, and H. C. Shum, «On-demand droplet collection for capturing single cells», Small **16**, 1902889 (2020).

[92] T. Buryska, M. Vasina, F. Gielen, P. Vanacek, L. V. Vliet, J. Jezek, Z. Pilat, P. Zemanek, J. Damborsky, F. Hollfelder, and Z. Prokop, «Controlled oil/water partitioning of hydrophobic substrates extending the bioanalytical applications of droplet-based microfluidics», Analytical Chemistry **91**, 10008–10015 (2019).

[93] M. S. Chowdhury, W. Zheng, S. Kumari, J. Heyman, X. Zhang, P. Dey, D. A. Weitz, and R. Haag, «Dendronized fluorosurfactant for highly stable water-in-fluorinated oil emulsions with minimal inter-droplet transfer of small molecules», Nature Communications **10**, 4546 (2019).

[94] J. Park, G. Destgeer, H. Kim, Y. Cho, and H. J. Sung, «In-droplet microparticle washing and enrichment using surface acoustic wave-driven acoustic radiation force», Lab on a Chip **18**, 2936–2945 (2018).

[95] M. A. Saucedo-Espinosa and P. S. Dittrich, «In-droplet electrophoretic separation and enrichment of biomolecules», Analytical Chemistry **92**, 8414–8421 (2020).

[96] S. Kim, B. Ganapathysubramanian, and R. K. Anand, «Concentration enrichment, separation, and cation exchange in nanoliter-scale water-in-oil droplets», Journal of the American Chemical Society **142**, 3196–3204 (2020).

[97] M. R. Kopp, M. Linsenmeier, B. Hettich, S. Prantl, S. Stavrakis, J. C. Leroux, and P. Arosio, «Microfluidic shrinking droplet concentrator for analyte detection and phase separation of protein solutions», Analytical Chemistry **92**, 5803–5812 (2020).

[98] F. Ahmadi, K. Samlali, P. Q. Vo, and S. C. Shih, «An integrated droplet-digital microfluidic system for on-demand droplet creation, mixing, incubation, and sorting», Lab on a Chip **19**, 524–535 (2019).

[99] S. S. Wells and R. T. Kennedy, «High-throughput liquid-liquid extractions with nanoliter volumes», Analytical Chemistry **92**, 3189–3197 (2020).

[100] H. Sinha, A. B. Quach, P. Q. Vo, and S. C. Shih, «An automated microfluidic gene-editing platform for deciphering cancer genes», Lab on a Chip **18**, 2300–2312 (2018).

[101] P. H. Lu, Y. D. Ma, C. Y. Fu, and G. B. Lee, «A structure-free digital microfluidic platform for detection of influenza a virus by using magnetic beads and electromagnetic forces», Lab on a Chip **20**, 789–797 (2020).

[102] L. Coudron, M. B. McDonnell, I. Munro, D. K. McCluskey, I. D. Johnston, C. K. Tan, and M. C. Tracey, «Fully integrated digital microfluidics platform for automated immunoassay; a versatile tool for rapid, specific detection of a wide range of pathogens», Biosensors and Bioelectronics **128**, 52–60 (2019).

[103] C. Dixon, J. Lamanna, and A. R. Wheeler, «Direct loading of blood for plasma separation and diagnostic assays on a digital microfluidic device», Lab on a Chip **20**, 1845–1855 (2020).

[104] S. Kalsi, M. Valiadi, C. Turner, M. Sutton, and H. Morgan, «Sample pre-concentration on a digital microfluidic platform for rapid amr detection in urine», Lab on a Chip **19**, 168–177 (2019).

[105] S. P. Zhang, J. Lata, C. Chen, J. Mai, F. Guo, Z. Tian, L. Ren, Z. Mao, P. H. Huang, P. Li, S. Yang, and T. J. Huang, «Digital acoustofluidics enables contactless and programmable liquid handling», Nature Communications **9**, 2928 (2018).

[106] E. Vargas, H. Teymourian, F. Tehrani, E. Eksin, E. Sánchez-Tirado, P. Warren, A. Erdem, E. Dassau, and J. Wang, «Enzymatic/immunoassay dual-biomarker sensing chip: towards decentralized insulin/glucose detection», Angewandte Chemie - International Edition **58**, 6376–6379 (2019).

[107] G. R. Cagnani, G. Ibáñez-Redín, B. Tirich, D. Gonçalves, D. T. Balogh, and O. N. Oliveira, «Fully-printed electrochemical sensors made with flexible screen-printed electrodes modified by roll-to-roll slot-die coating», Biosensors and Bioelectronics **165**, 112428 (2020).

[108] Y. Yang, K. Gupta, and K. L. Ekinci, «All-electrical monitoring of bacterial antibiotic susceptibility in a microfluidic device», Proceedings of the National Academy of Sciences of the United States of America **117**, 10639–10644 (2020).

[109] M. U. A. Prathap, E. Castro-Pérez, J. A. Jiménez-Torres, V. Setaluri, and S. Gunasekaran, «A flow-through microfluidic system for the detection of circulating melanoma cells», Biosensors and Bioelectronics **142**, 111522 (2019).

[110] S. T. Rajendran, E. Scarano, M. H. Bergkamp, A. M. Capria, C. H. Cheng, K. Sanger, G. Ferrari, L. H. Nielsen, E. T. Hwu, K. Zór, and A. Boisen, «Modular, lightweight, wireless potentiostat-on-a-disc for electrochemical detection in centrifugal microfluidics», Analytical Chemistry **91**, 11620–11628 (2019).

[111] Y. H. Chen, A. K. Pulikkathodi, Y. D. Ma, Y. L. Wang, and G. B. Lee, «A microfluidic platform integrated with field-effect transistors for enumeration of circulating tumor cells», Lab on a Chip **19**, 618–625 (2019).

[112] G. Linz, S. Djeljadini, L. Steinbeck, G. Köse, F. Kiessling, and M. Wessling, «Cell barrier characterization in transwell inserts by elec-

trical impedance spectroscopy», Biosensors and Bioelectronics **165**, 112345 (2020).

[113] W. Fan, X. Chen, Y. Ge, Y. Jin, Q. Jin, and J. Zhao, «Single-cell impedance analysis of osteogenic differentiation by droplet-based microfluidics», Biosensors and Bioelectronics **145**, 111730 (2019).

[114] A. Saateh, A. Kalantarifard, O. T. Celik, M. Asghari, M. Serhatlioglu, and C. Elbuken, «Real-time impedimetric droplet measurement (idm)», Lab on a Chip **19**, 3815–3824 (2019).

[115] L. Chen, Z. Han, X. Fan, S. Zhang, J. Wang, and X. Duan, «An impedance-coupled microfluidic device for single-cell analysis of primary cell wall regeneration», Biosensors and Bioelectronics **165**, 112374 (2020).

[116] S. Sevim, C. Franco, X. Z. Chen, A. Sorrenti, D. Rodríguez-San-Miguel, S. Pané, A. J. deMello, and J. Puigmartí-Luis, «Sers barcode libraries: a microfluidic approach», Advanced Science **7**, 1903172 (2020).

[117] R. Gao, Z. Cheng, X. Wang, L. Yu, Z. Guo, G. Zhao, and J. Choo, «Simultaneous immunoassays of dual prostate cancer markers using a sers-based microdroplet channel», Biosensors and Bioelectronics **119**, 126–133 (2018).

[118] N. Nitta, T. Iino, A. Isozaki, M. Yamagishi, Y. Kitahama, S. Sakuma, Y. Suzuki, H. Tezuka, M. Oikawa, F. Arai, T. Asai, D. Deng, H. Fukuzawa, M. Hase, T. Hasunuma, T. Hayakawa, K. Hiraki, K. Hiramatsu, Y. Hoshino, M. Inaba, Y. Inoue, T. Ito, M. Kajikawa, H. Karakawa, Y. Kasai, Y. Kato, H. Kobayashi, C. Lei, S. Matsusaka, H. Mikami, A. Nakagawa, K. Numata, T. Ota, T. Sekiya, K. Shiba, Y. Shirasaki, N. Suzuki, S. Tanaka, S. Ueno, H. Watarai, T. Yamano, M. Yazawa, Y. Yonamine, D. D. Carlo, Y. Hosokawa, S. Uemura, T. Sugimura, Y. Ozeki, and K. Goda, «Raman image-activated cell sorting», Nature Communications **11**, 3452 (2020).

[119] E. M. Höhn, R. Panneerselvam, A. Das, and D. Belder, «Raman spectroscopic detection in continuous microflow using a chip-integrated silver electrode as an electrically regenerable surface-

enhanced raman spectroscopy substrate», Analytical Chemistry **91**, 9844–9851 (2019).

[120] M. R. Willner, K. S. McMillan, D. Graham, P. J. Vikesland, and M. Zagnoni, «Surface-enhanced raman scattering based microfluidics for single-cell analysis», Analytical Chemistry **90**, 12004–12010 (2018).

[121] L. L. Wu, Z. L. Zhang, M. Tang, D. L. Zhu, X. J. Dong, J. Hu, C. B. Qi, H. W. Tang, and D. W. Pang, «Spectrally combined encoding for profiling heterogeneous circulating tumor cells using a multifunctional nanosphere-mediated microfluidic platform», Angewandte Chemie - International Edition **59**, 11240–11244 (2020).

[122] L. Armbrecht, R. S. Müller, J. Nikoloff, and P. S. Dittrich, «Single-cell protein profiling in microchambers with barcoded beads», Microsystems and Nanoengineering **5**, 55 (2019).

[123] J. Luan, A. Seth, R. Gupta, Z. Wang, P. Rathi, S. Cao, H. G. Derami, R. Tang, B. Xu, S. Achilefu, J. J. Morrissey, and S. Singamaneni, «Ultrabright fluorescent nanoscale labels for the femtomolar detection of analytes with standard bioassays», Nature Biomedical Engineering **4**, 518–530 (2020).

[124] G. Fu, Y. Zhu, K. Xu, W. Wang, R. Hou, and X. Li, «Photothermal microfluidic sensing platform using near-infrared laser-driven multiplexed dual-mode visual quantitative readout», Analytical Chemistry **91**, 13290–13296 (2019).

[125] M. Pahl, M. Mayer, M. Schneider, D. Belder, and K. R. Asmis, «Joining microfluidics with infrared photodissociation: online monitoring of isomeric flow-reaction intermediates», Analytical Chemistry **91**, 3199–3203 (2019).

[126] X. Zhang, X. Wei, X. Men, Z. Jiang, W. Q. Ye, M. L. Chen, T. Yang, Z. R. Xu, and J. H. Wang, «Inertial-force-assisted, high-throughput, droplet-free, single-cell sampling coupled with icp-ms for real-time cell analysis», Analytical Chemistry **92**, 6604–6612 (2020).

[127] P. Liu, Q. Huang, M. Khan, N. Xu, H. Yao, and J. M. Lin, «Microfluidic probe for in-situ extraction of adherent cancer cells to detect

heterogeneity difference by electrospray ionization mass spectrometry», Analytical Chemistry **92**, 7900–7906 (2020).

[128] S. K. Piendl, D. Geissler, L. Weigelt, and D. Belder, «Multiple heart-cutting two-dimensional chip-hplc combined with deep-uv fluorescence and mass spectrometric detection», Analytical Chemistry **92**, 3795–3803 (2020).

[129] D. Haidas, M. Napiorkowska, S. Schmitt, and P. S. Dittrich, «Parallel sampling of nanoliter droplet arrays for noninvasive protein analysis in discrete yeast cultivations by maldi-ms», Analytical Chemistry **92**, 3810–3818 (2020).

[130] D. A. Holland-Moritz, M. K. Wismer, B. F. Mann, I. Farasat, P. Devine, E. D. Guetschow, I. Mangion, C. J. Welch, J. C. Moore, S. Sun, and R. T. Kennedy, «Mass activated droplet sorting (mads) enables high-throughput screening of enzymatic reactions at nanoliter scale», Angewandte Chemie - International Edition **59**, 4470–4477 (2020).

[131] Y. Zhu, G. Clair, W. B. Chrisler, Y. Shen, R. Zhao, A. K. Shukla, R. J. Moore, R. S. Misra, G. S. Pryhuber, R. D. Smith, C. Ansong, and R. T. Kelly, «Proteomic analysis of single mammalian cells enabled by microfluidic nanodroplet sample preparation and ultrasensitive nanolc-ms», Angewandte Chemie - International Edition **57**, 12370–12374 (2018).

[132] D. Zhang, Y. Yang, Q. Qin, J. Xu, B. Wang, J. Chen, B. Liu, W. Zhang, and L. Qiao, «Maldi-tof characterization of protein expression mutation during morphological changes of bacteria under the impact of antibiotics», Analytical Chemistry **91**, 2352–2359 (2019).

[133] R. Fernández, J. Garate, T. Tolentino-Cortez, A. Herraiz, L. Lombardero, F. Ducrocq, R. Rodríguez-Puertas, P. Trifilieff, E. Astigarraga, G. Barreda-Gómez, and J. A. Fernández, «Microarray and mass spectrometry-based methodology for lipid profiling of tissues and cell cultures», Analytical Chemistry **91**, 15967–15973 (2019).

[134] J. Grant, S. H. Goudarzi, and M. Mrksich, «High-throughput enzyme kinetics with 3d microfluidics and imaging samdi mass spectrometry», Analytical Chemistry **90**, 13096–13103 (2018).

[135] S. Hong, E. Dechaumphai, C. R. Green, R. Lal, A. N. Murphy, C. M. Metallo, and R. Chen, «Sub-nanowatt microfluidic single-cell calorimetry», Nature Communications **11**, 2982 (2020).

[136] S. Hur, R. Mittapally, S. Yadlapalli, P. Reddy, and E. Meyhofer, «Sub-nanowatt resolution direct calorimetry for probing real-time metabolic activity of individual c. elegans worms», Nature Communications **11**, 2983 (2020).

[137] Y. Liu, T. Lehnert, and M. A. Gijs, «Fast antimicrobial susceptibility testing on escherichia coli by metabolic heat nanocalorimetry», Lab on a chip **20**, 3144–3157 (2020).

[138] H. Davoodi, N. Nordin, L. Bordonali, J. G. Korvink, N. MacKinnon, and V. Badilita, «An nmr-compatible microfluidic platform enabling: in situ electrochemistry», Lab on a Chip **20**, 3202–3212 (2020).

[139] T. Lange, S. Charton, T. Bizien, F. Testard, and F. Malloggi, «Oste+ for: in situ saxs analysis with droplet microfluidic devices», Lab on a Chip **20**, 2990–3000 (2020).

[140] M. E. Mäeots, B. Lee, A. Nans, S. G. Jeong, M. M. Esfahani, S. Ding, D. J. Smith, C. S. Lee, S. S. Lee, M. Peter, and R. I. Enchev, «Modular microfluidics enables kinetic insight from time-resolved cryo-em», Nature Communications **11**, 3465 (2020).

[141] Z. Liu, P. Zhang, H. Ji, Y. Long, B. Jing, L. Wan, D. Xi, R. An, and X. Lan, «A mini-panel pet scanner-based microfluidic radiobioassay system allowing high-throughput imaging of real-time cellular pharmacokinetics», Lab on a Chip **20**, 1110–1123 (2020).

[142] N. Zaraee, F. E. kanik, A. M. Bhuiya, E. S. Gong, M. T. Geib, N. L. Ünlü, A. Y. Ozkumur, J. R. Dupuis, and M. S. Ünlü, «Highly sensitive and label-free digital detection of whole cell e. coli with interferometric reflectance imaging», Biosensors and Bioelectronics **162**, 112258 (2020).

[143] L. Patinglag, M. M. Esfahani, K. Ragunathan, P. He, N. J. Brown, S. J. Archibald, N. Pamme, and M. D. Tarn, «On-chip electrochemical detection of glucose towards the miniaturised quality control of carbohydrate-based radiotracers», The Analyst **145**, 4920–4930 (2020).

[144] M. D. Tarn, N. Y. Kzlyer, M. M. Esfahani, P. Joshi, N. J. Brown, N. Pamme, D. G. Jenkins, and S. J. Archibald, «Plastic scintillator-based microfluidic devices for miniaturized detection of positron emission tomography radiopharmaceuticals», Chemistry - A European Journal **24**, 13749–13753 (2018).

[145] N. L. Calistri, R. J. Kimmerling, S. W. Malinowski, M. Touat, M. M. Stevens, S. Olcum, K. L. Ligon, and S. R. Manalis, «Microfluidic active loading of single cells enables analysis of complex clinical specimens», Nature Communications **9**, 4784 (2018).

[146] P. Chen, S. Yan, J. Wang, Y. Guo, Y. Dong, X. Feng, X. Zeng, Y. Li, W. Du, and B. F. Liu, «Dynamic microfluidic cytometry for single-cell cellomics: high-throughput probing single-cell-resolution signaling», Analytical Chemistry **91**, 1619–1626 (2019).

[147] Y. Cho, S. A. Lee, Y. L. Chew, K. Broderick, W. R. Schafer, and H. Lu, «Multimodal stimulation in a microfluidic device facilitates studies of interneurons in sensory integration in c. elegans», Small **16**, 1905852 (2020).

[148] A. D. Rodriguez, L. F. Horowitz, K. Castro, H. Kenerson, N. Bhattacharjee, G. Gandhe, A. Raman, R. J. Monnat, R. Yeung, R. C. Rostomily, and A. Folch, «A microfluidic platform for functional testing of cancer drugs on intact tumor slices», Lab on a Chip **20**, 1658–1675 (2020).

[149] B. Hamza, S. R. Ng, S. M. Prakadan, F. F. Delgado, C. R. Chin, E. M. King, L. F. Yang, S. M. Davidson, K. L. DeGouveia, N. Cermak, A. W. Navia, P. S. Winter, R. S. Drake, T. Tammela, C. M. C. Li, T. Papagiannakopoulos, A. J. Gupta, J. S. Bagnall, S. M. Knudsen, M. G. V. Heiden, S. C. Wasserman, T. Jacks, A. K. Shalek, and S. R. Manalis, «Optofluidic real-time cell sorter for longitudinal ctc

studies in mouse models of cancer», Proceedings of the National Academy of Sciences **116**, 2232–2236 (2019).

[150] R. H. Pritchard, A. A. Zhukov, J. N. Fullerton, A. J. Want, F. Hussain, M. F. L. Cour, M. E. Bashtanov, R. D. Gold, A. Hailes, E. Banham-Hall, and S. S. Rogers, «Cell sorting actuated by a microfluidic inertial vortex», Lab on a Chip **19**, 2456–2465 (2019).

[151] Y. Zhou, Z. Ma, and Y. Ai, «Hybrid microfluidic sorting of rare cells based on high throughput inertial focusing and high accuracy acoustic manipulation», RSC Advances **9**, 31186–31195 (2019).

[152] M. T. Chung, K. Kurabayashi, and D. Cai, «Single-cell rt-lamp mrna detection by integrated droplet sorting and merging», Lab on a Chip **19**, 2425–2434 (2019).

[153] G. Sun, Y. Teng, Z. Zhao, L. F. Cheow, H. Yu, H. Yu, H. Yu, H. Yu, and C. H. Chen, «Functional stem cell sorting via integrative droplet synchronization», Analytical Chemistry **92**, 7915–7923 (2020).

[154] A. Isozaki, H. Mikami, H. Tezuka, H. Matsumura, K. Huang, M. Akamine, K. Hiramatsu, T. Iino, T. Ito, H. Karakawa, Y. Kasai, Y. Li, Y. Nakagawa, S. Ohnuki, T. Ota, Y. Qian, S. Sakuma, T. Sekiya, Y. Shirasaki, N. Suzuki, E. Tayyabi, T. Wakamiya, M. Xu, M. Yamagishi, H. Yan, Q. Yu, S. Yan, D. Yuan, W. Zhang, Y. Zhao, F. Arai, R. E. Campbell, C. Danelon, D. D. Carlo, K. Hiraki, Y. Hoshino, Y. Hosokawa, M. Inaba, A. Nakagawa, Y. Ohya, M. Oikawa, S. Uemura, Y. Ozeki, T. Sugimura, N. Nitta, and K. Goda, «Intelligent image-activated cell sorting 2.0», Lab on a Chip **20**, 2263–2273 (2020).

[155] Y. Yalikun, N. Ota, B. Guo, T. Tang, Y. Zhou, C. Lei, H. Kobayashi, Y. Hosokawa, M. Li, H. E. Muñoz, D. D. Carlo, K. Goda, and Y. Tanaka, «Effects of flow-induced microfluidic chip wall deformation on imaging flow cytometry», Cytometry Part A **97**, 909–920 (2020).

[156] M. Sesen and G. Whyte, «Image-based single cell sorting automation in droplet microfluidics», Scientific Reports **10**, 8736 (2020).

[157] A. Gérard, A. Woolfe, G. Mottet, M. Reichen, C. Castrillon, V. Menrath, S. Ellouze, A. Poitou, R. Doineau, L. Briseno-Roa, P. Canales-Herrerias, P. Mary, G. Rose, C. Ortega, M. Delincé, S. Essono, B. Jia, B. Iannascoli, O. R.-L. Goff, R. Kumar, S. N. Stewart, Y. Pousse, B. Shen, K. Grosselin, B. Saudemont, A. Sautel-Caillé, A. Godina, S. McNamara, K. Eyer, G. A. Millot, J. Baudry, P. England, C. Nizak, A. Jensen, A. D. Griffiths, P. Bruhns, and C. Brenan, «High-throughput single-cell activity-based screening and sequencing of antibodies using droplet microfluidics», Nature Biotechnology **38**, 715–721 (2020).

[158] M. N. Hsu, S. C. Wei, S. Guo, D. T. Phan, Y. Zhang, and C. H. Chen, «Smart hydrogel microfluidics for single-cell multiplexed secretomic analysis with high sensitivity», Small **14**, 1802918 (2018).

[159] R. Rodriguez-Moncayo, R. J. Jimenez-Valdes, A. M. Gonzalez-Suarez, and J. L. Garcia-Cordero, «Integrated microfluidic device for functional secretory immunophenotyping of immune cells», ACS Sensors **5**, 353–361 (2020).

[160] L. Armbrecht, O. Rutschmann, B. M. Szczerba, J. Nikoloff, N. Aceto, and P. S. Dittrich, «Quantification of protein secretion from circulating tumor cells in microfluidic chambers», Advanced Science **7**, 1903237 (2020).

[161] J. F. Edd, A. Mishra, T. D. Dubash, S. Herrera, R. Mohammad, E. K. Williams, X. Hong, B. R. Mutlu, J. R. Walsh, F. M. D. Carvalho, B. Aldikacti, L. T. Nieman, S. L. Stott, R. Kapur, S. Maheswaran, D. A. Haber, and M. Toner, «Microfluidic concentration and separation of circulating tumor cell clusters from large blood volumes», Lab on a Chip **20**, 558–567 (2020).

[162] N. Xiang, J. Wang, Q. Li, Y. Han, D. Huang, and Z. Ni, «Precise size-based cell separation via the coupling of inertial microfluidics and deterministic lateral displacement», Analytical Chemistry **91**, 10328–10334 (2019).

[163] Z. Zhang, W. Chien, E. Henry, D. A. Fedosov, and G. Gompper, «Sharp-edged geometric obstacles in microfluidics promote

deformability-based sorting of cells», Physical Review Fluids **4**, 24201 (2019).

[164] E. Islamzada, K. Matthews, Q. Guo, A. T. Santoso, S. P. Duffy, M. D. Scott, and H. Ma, «Deformability based sorting of stored red blood cells reveals donor-dependent aging curves», Lab on a Chip **20**, 226–235 (2020).

[165] B. Kim, K. H. Kim, Y. Chang, S. Shin, E. C. Shin, and S. Choi, «One-step microfluidic purification of white blood cells from whole blood for immunophenotyping», Analytical Chemistry **91**, 13230–13236 (2019).

[166] S. Zhu, D. Wu, Y. Han, C. Wang, N. Xiang, and Z. Ni, «Inertial microfluidic cube for automatic and fast extraction of white blood cells from whole blood», Lab on a Chip **20**, 244–252 (2020).

[167] A. Mishra, T. D. Dubash, J. F. Edd, M. K. Jewett, S. G. Garre, N. M. Karabacak, D. C. Rabe, B. R. Mutlu, J. R. Walsh, R. Kapur, S. L. Stott, S. Maheswaran, D. A. Haber, and M. Toner, «Ultrahigh-throughput magnetic sorting of large blood volumes for epitope-agnostic isolation of circulating tumor cells», Proceedings of the National Academy of Sciences of the United States of America **117**, 16839–16847 (2020).

[168] R. Agarwal, A. Sarkar, A. Bhowmik, D. Mukherjee, and S. Chakraborty, «A portable spinning disc for complete blood count (cbc)», Biosensors and Bioelectronics **150**, 111935 (2020).

[169] A. M. Nightingale, C. L. Leong, R. A. Burnish, S. ul Hassan, Y. Zhang, G. F. Clough, M. G. Boutelle, D. Voegeli, and X. Niu, «Monitoring biomolecule concentrations in tissue using a wearable droplet microfluidic-based sensor», Nature Communications **10**, 2741 (2019).

[170] H. Wu, Z. Ma, C. Wei, M. Jiang, X. Hong, Y. Li, D. Chen, and X. Huang, «Three-dimensional microporous hollow fiber membrane microfluidic device integrated with selective separation and capillary self-driven for point-of-care testing», Analytical Chemistry **92**, 6358–6365 (2020).

[171] Y. Zhang, H. Guo, S. B. Kim, Y. Wu, D. Ostojich, S. H. Park, X. Wang, Z. Weng, R. Li, A. J. Bandodkar, Y. Sekine, J. Choi, S. Xu, S. Quaggin, R. Ghaffari, and J. A. Rogers, «Passive sweat collection and colorimetric analysis of biomarkers relevant to kidney disorders using a soft microfluidic system», Lab on a Chip **19**, 1545–1555 (2019).

[172] L. Mou, R. Dong, B. Hu, Z. Li, J. Zhang, and X. Jiang, «Hierarchically structured microchip for point-of-care immunoassays with dynamic detection ranges», Lab on a Chip **19**, 2750–2757 (2019).

[173] S. Shin, B. Kim, Y. J. Kim, and S. Choi, «Integrated microfluidic pneumatic circuit for point-of-care molecular diagnostics», Biosensors and Bioelectronics **133**, 169–176 (2019).

[174] I. C. Samper, S. A. Gowers, M. A. Booth, C. Wang, T. Watts, T. Phairatana, N. Vallant, B. Sandhu, V. Papalois, and M. G. Boutelle, «Portable microfluidic biosensing system for real-time analysis of microdialysate in transplant kidneys», Analytical Chemistry **91**, 14631–14638 (2019).

[175] C. Che, N. Li, K. D. Long, M. Á. Aguirre, T. D. Canady, Q. Huang, U. Demirci, and B. T. Cunningham, «Activate capture and digital counting (ac + dc) assay for protein biomarker detection integrated with a self-powered microfluidic cartridge», Lab on a Chip **19**, 3943–3953 (2019).

[176] K. Nishiyama, T. Kasama, S. Nakamata, K. Ishikawa, D. Onoshima, H. Yukawa, M. Maeki, A. Ishida, H. Tani, Y. Baba, and M. Tokeshi, «Ultrasensitive detection of disease biomarkers using an immunowall device with enzymatic amplification», Analyst **144**, 4589–4595 (2019).

[177] G. Morad, C. V. Carman, E. J. Hagedorn, J. R. Perlin, L. I. Zon, N. Mustafaoglu, T. E. Park, D. E. Ingber, C. C. Daisy, and M. A. Moses, «Tumor-derived extracellular vesicles breach the intact blood-brain barrier via transcytosis», ACS Nano **13**, 13853–13865 (2019).

[178] Y. T. Kang, T. Hadlock, T. W. Lo, E. Purcell, A. Mutukuri, S. Fouladdel, M. D. S. Raguera, H. Fairbairn, V. Murlidhar, A. Durham, S. A. McLean, and S. Nagrath, «Dual-isolation and profiling of circu-

lating tumor cells and cancer exosomes from blood samples with melanoma using immunoaffinity-based microfluidic interfaces», Advanced Science **7**, 2001581 (2020).

[179] C. Z. Lim, Y. Zhang, Y. Chen, H. Zhao, M. C. Stephenson, N. R. Ho, Y. Chen, J. Chung, A. Reilhac, T. P. Loh, C. L. Chen, and H. Shao, «Subtyping of circulating exosome-bound amyloid b reflects brain plaque deposition», Nature Communications **10**, 1–11 (2019).

[180] D. G. Mathew, P. Beekman, S. G. Lemay, H. Zuilhof, S. L. Gac, and W. G. V. D. Wiel, «Electrochemical detection of tumor-derived extracellular vesicles on nanointerdigitated electrodes», Nano Letters **20**, 820–828 (2020).

[181] S. Cho, H. C. Yang, and W. J. Rhee, «Simultaneous multiplexed detection of exosomal micrornas and surface proteins for prostate cancer diagnosis», Biosensors and Bioelectronics **146**, 111749 (2019).

[182] C. Liu, J. Zhao, F. Tian, L. Cai, W. Zhang, Q. Feng, J. Chang, F. Wan, Y. Yang, B. Dai, Y. Cong, B. Ding, J. Sun, and W. Tan, «Low-cost thermophoretic profiling of extracellular-vesicle surface proteins for the early detection and classification of cancers», Nature Biomedical Engineering **3**, 183–193 (2019).

[183] C. Liu, J. Zhao, F. Tian, J. Chang, W. Zhang, and J. Sun, «I-dna- and aptamer-mediated sorting and analysis of extracellular vesicles», Journal of the American Chemical Society **141**, 3817–3821 (2019).

[184] H. Zhang and D. Lyden, «Asymmetric-flow field-flow fractionation technology for exomere and small extracellular vesicle separation and characterization», Nature Protocols **14**, 1027–1053 (2019).

[185] G. B. Adkins, E. Sun, R. Coreas, and W. Zhong, «Asymmetrical flow field flow fractionation coupled to nanoparticle tracking analysis for rapid online characterization of nanomaterials», Analytical Chemistry **92**, 7071–7078 (2020).

[186] Y. Liu, W. Zhao, R. Cheng, M. Logun, M. D. M. Zayas-Viera, L. Karumbaiah, and L. Mao, «Label-free ferrohydrodynamic separation of exosome-like nanoparticles», Lab on a Chip **20**, 3187–3201 (2020).

[187] Y. Hattori, T. Shimada, T. Yasui, N. Kaji, and Y. Baba, «Micro- and nanopillar chips for continuous separation of extracellular vesicles», Analytical chemistry **91**, 6514–6521 (2019).

[188] W. Kang, S. Sarkar, Z. S. Lin, S. McKenney, and T. Konry, «Ultrafast parallelized microfluidic platform for antimicrobial susceptibility testing of gram positive and negative bacteria», Analytical Chemistry **91**, 6242–6249 (2019).

[189] H. Li, P. Torab, K. E. Mach, C. Surrette, M. R. England, D. W. Craft, N. J. Thomas, J. C. Liao, C. Puleo, and P. K. Wong, «Adaptable microfluidic system for single-cell pathogen classification and antimicrobial susceptibility testing», Proceedings of the National Academy of Sciences of the United States of America **116**, 10270–10279 (2019).

[190] L. Coudron, M. B. McDonnell, I. Munro, D. K. McCluskey, I. D. Johnston, C. K. Tan, and M. C. Tracey, «Fully integrated digital microfluidics platform for automated immunoassay; a versatile tool for rapid, specific detection of a wide range of pathogens», Biosensors and Bioelectronics **128**, 52–60 (2019).

[191] J. Kehe, A. Kulesa, A. Ortiz, C. M. Ackerman, S. G. Thakku, D. Sellers, S. Kuehn, J. Gore, J. Friedman, and P. C. Blainey, «Massively parallel screening of synthetic microbial communities», Proceedings of the National Academy of Sciences of the United States of America **116**, 12804–12809 (2019).

[192] K. A. Nahas, J. Cama, M. Schaich, K. Hammond, S. Deshpande, C. Dekker, M. G. Ryadnov, and U. F. Keyser, «A microfluidic platform for the characterisation of membrane active antimicrobials», Lab on a Chip **19**, 837–844 (2019).

[193] «Massively multiplexed nucleic acid detection with cas13», Nature **582**, 277–282 (2020).

[194] Z. Huang, D. Tian, Y. Liu, Z. Lin, C. J. Lyon, W. Lai, D. Fusco, A. Drouin, X. Yin, T. Hu, and B. Ning, «Ultra-sensitive and high-throughput crispr-p owered covid-19 diagnosis», Biosensors and Bioelectronics **164**, 112316 (2020).

[195] Q. Lin, D. Wen, J. Wu, L. Liu, W. Wu, X. Fang, and J. Kong, «Microfluidic immunoassays for sensitive and simultaneous detection of igg/igm/antigen of sars-cov-2 within 15 min», Analytical Chemistry **92**, 9454–9458 (2020).

[196] J. A. Wippold, H. Wang, J. Tingling, J. L. Leibowitz, P. de Figueiredo, and A. Han, «Prescient: platform for the rapid evaluation of antibody success using integrated microfluidics enabled technology», Lab on a Chip **20**, 1628–1638 (2020).

[197] J. Zhou, P. Kondylis, D. G. Haywood, Z. D. Harms, Lye, S. Lee, A. Zlotnick, and S. C. Jacobson, «Characterization of virus capsids and their assembly intermediates by multicycle resistive-pulse sensing with four pores in series», Anal. Chem **90**, 33 (2018).

[198] P. N. Hedde, T. J. Abram, A. Jain, R. Nakajima, R. R. de Assis, T. Pearce, A. Jasinskas, M. N. Toosky, S. Khan, P. L. Felgner, E. Gratton, and W. Zhao, «A modular microarray imaging system for highly specific covid-19 antibody testing», Lab on a chip **20**, 3302–3309 (2020).

[199] M. P. McRae, G. W. Simmons, N. J. Christodoulides, Z. Lu, S. K. Kang, D. Fenyo, T. Alcorn, I. P. Dapkins, I. Sharif, D. Vurmaz, S. S. Modak, K. Srinivasan, S. Warhadpande, R. Shrivastav, and J. T. McDevitt, «Clinical decision support tool and rapid point-of-care platform for determining disease severity in patients with covid-19», Lab on a Chip **20**, 2075–2085 (2020).

[200] X. Jiang, J. C. Loeb, C. Manzanas, J. A. Lednicky, and Z. H. Fan, «Valve-enabled sample preparation and rna amplification in a coffee mug for zika virus detection», Angewandte Chemie - International Edition **57**, 17211–17214 (2018).

[201] Y. D. Ma, K. H. Li, Y. H. Chen, Y. M. Lee, S. T. Chou, Y. Y. Lai, P. C. Huang, H. P. Ma, and G. B. Lee, «A sample-to-answer, portable platform for rapid detection of pathogens with a smartphone interface», Lab on a Chip **19**, 3804–3814 (2019).

[202] Y. Minagawa, H. Ueno, K. V. Tabata, and H. Noji, «Mobile imaging platform for digital influenza virus counting», Lab on a Chip **19**, 2678–2687 (2019).

[203] E. A. Phillips, T. J. Moehling, K. F. Ejendal, O. S. Hoilett, K. M. Byers, L. A. Basing, L. A. Jankowski, J. B. Bennett, L. K. Lin, L. A. Stanciu, and J. C. Linnes, «Microfluidic rapid and autonomous analytical device (microraad) to detect hiv from whole blood samples», Lab on a Chip **19**, 3375–3386 (2019).

Chapter 3

Multiplexed analysis of signalling proteins at the single-immune cell level

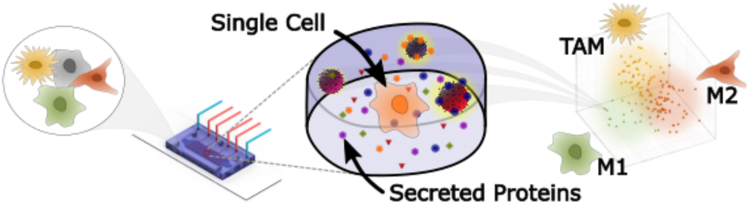

Authors: **Claudius L. Dietsche**
Elisabeth Hirth
Petra S. Dittrich
Journal: *Lab on a Chip*
doi: 10.1039/D2LC00891B
Published: 15 December 2022

Reproduced from C. L. Dietsche, E. Hirth, and P. S. Dittrich, «Multiplexed analysis of signalling proteins at the single-immune cell level», Lab on a Chip **23**, 362–371 (2022) with permission from the Royal Society of Chemistry.

Multiplexed analysis of signalling proteins at the single-immune cell level

Claudius L. Dietsche[1], Elisabeth Hirth[1], and Petra S. Dittrich[1*]

[1]Department of Biosystems Science and Engineering, Mattenstrasse 26, 4125 Basel, Switzerland
*petra.dittrich@bsse.ethz.ch

High numbers of tumour-associated macrophages (TAMs) in the tumour microenvironment are associated with a poor prognosis. However, the effect of TAMs on tumour progression depends on the proteins secreted by individual TAMs. Here, we developed a microfluidic platform to quantitatively measure the secreted proteins of individual macrophages as well as macrophages polarized by the culture medium derived from breast cancer cells. The macrophages were captured in hydrodynamic traps and isolated with pneumatically activated valves for single-cell analysis. Barcoded and functionalized magnetic beads were captured in specially designed traps to determine the secreted proteins by immunoassay. Individual bead trapping facilitated the recording of the protein concentration since all beads were geometrically constrained in the same focal plane, which is an important requirement for rapid and automated image analysis. By determining three signaling proteins, namely interleuking 10 (IL-10), vascular endothelial growth factor (VEGF), and tumour necrosis factor alpha (TNF-α), we successfully distinguished between differently polarized macrophages. The results indicate a heterogeneous pattern, with M2 macrophages characterized by a higher secretion of IL-10, while M1 macrophages secrete high levels of the inflammatory cytokine TNF-α. The macrophages treated with the supernatant from cancer cells show a similar signalling pattern to M2 macrophages with an increased secretion of the pro-tumoural cytokine VEGF. This microfluidic method resolves correlations in signaling protein expression at the single-cell level. Ultimately, single-macrophage analysis can contribute to the development of novel therapies aimed at reversing M2-like TAMs into M1-like TAMs.

3.1 Introduction

Cytokine signalling is an important process for cell-to-cell communication, enabling complex interactions between cells in a highly heterogeneous population [1, 2].

However, cell-to-cell signalling not only plays a critical role in the development, survival, and proliferation of its own population but also has a profound impact on the surrounding microenvironment [3]. Tissue-resident macrophages are immune cells that reside throughout the body and influence the course of diseases based on cell-to-cell signaling [4]. Of particular interest are the effects of macrophages on the tumour microenvironment (TME), as they can account for up to 50% of tumour mass and are important regulators of cell proliferation and the apoptosis cycle [2, 5, 6]. Several studies have shown that tumour-associated macrophages (TAMs) have the potential to affect tumour growth in a positive as well as negative way depending on the dominating phenotype [7–9]. Macrophages are highly plastic and within the TME can change their phenotype, a process known as polarization, in response to stimuli such as interferon gamma (INF-γ), interleukin 4 (IL-4) and interleukin 13 (IL-13) [10, 11]. Polarized macrophages can be classified as classically activated (M1) macrophages and alternatively activated (M2) macrophages. The polarization of macrophages can be determined by the combination of cytokines that each individual macrophage produces and secretes. Tumour necrosis factor alpha (TNF-α) is associated with tumour suppressive properties, whereas interleukin 10 (IL-10) and vascular endothelial growth factor (VEGF) are associated with tumour proliferation [12, 13]. Novel treatment approaches focus on the repolarization of tumour-promoting (M2-like) macrophages to tumour-suppressing (M1-like) macrophages [14–16]. Therefore, due to the heterogeneity of the TME and TAMs in particular, it is critical to deepen the understanding of the underlying mechanisms at the single-cell level to eventually find an effective and reliable treatment.

In microfluidic systems, fluids are confined and manipulated in sub-millimetre structures, making them ideal for studying protein secretion at the single-cell level. The dimensions of these engineered systems are in the low micrometre range (i.e., the same order of magnitude as living cells), allowing precise and rapid manipulation of biological samples [17–21]. The capture and isolation of single cells at this microscale has enabled the development of high-throughput single-cell analysis techniques in recent years. In particular, single-cell RNAseq has attracted considerable interest due to its sensitivity, throughput, and multiplexing capabilities [22]. Knowledge of the cell's transcriptome provides an extensive insight into the up- and downregulation of gene expression but cannot reflect the cell state at the protein level, e.g., RNAseq is not suitable for assessing the secretion of proteins.

Droplet microfluidics is particularly well suited for high-throughput single-cell analysis due to the compartmentalization of single cells in droplets [22–26]. However, droplet microfluidics is hampered by the inability to replace reagents which can affect the detection of secreted proteins with high sensitivity. Alternatively, open nano wells have been utilized for the purpose of highly sensitive detection of single-cell secreted proteins [27, 28]. The shortcoming with this technology is that the secreted proteins are not contained in the well but can diffuse out of them [27]. In contrast, microchambers have been developed for isolation of single cells with the flexibility of conventional 96-well plates [29, 30]. Due to their flexibility in reagent exchange, the sensitivity of microchamber bioassays far exceeds that of droplet microfluidics. Precisely positioned and designed mechanical columns, known as hydrodynamic traps, within the microchambers enable efficient and label-free immobilization and isolation of single cells [21]. Due to their micrometre scale, microfluidic systems allow high parallelization of the microchambers and simultaneous readout of hundreds to thousands of individual cells [20].

Immunoassays allow quantification of proteins on the cell membrane or those secreted by the cell. Multiplexed quantification of proteins in single cells has been achieved by coating different sections of a microchamber with different antibodies [31–33]. This method requires immobilization of capture antibodies during microfluidic device fabrication, which increases the fabrication complexity. In addition, this fabrication method results in high background noise due to nonspecific binding of antibodies during the fabrication process. Recently, in Armbrecht et al., we presented a new method in which multiplexed quantification of intracellular proteins was enabled by introducing barcoded magnetic beads with specifically coated antibodies [30]. Due to commercially available beads with more than 300 target proteins, this method can be easily adapted to proteins of interest and has a higher sensitivity compared to previous methods. However, in our previous approach, the cells were captured in the same traps as the magnetic beads, which necessitated cell tagging. Furthermore, the relatively large magnetic traps led to bead aggregation and overlap, which caused signal diminution and difficulties in automation.

In this work we have significantly improved the microfluidic platform for the quantitative measurement of secreted proteins at the single-cell level. We use hydrodynamic traps to capture single cells by size without tags (i.e., without the need of attaching beads to the cells) and magnetic traps to immobilize barcoded, functionalized magnetic beads in the same microchambers. The magnetic traps are implemented using small cavities enforcing single-bead occupancy at a specific location in the chamber. This design greatly improves automated imaging and image analysis, which is a prerequisite for a further increase in throughput. Based on an on-bead immunoassay, the secretion profile of differentially polarized macrophages is investigated and analysed.

3.2 Experimental

3.2.1 Wafer fabrication

The silicon master moulds for the PDMS microfluidic chip were fabricated using soft lithography. One layer was required for the cell suspension and analysis (fluid layer), and a second layer was required for defining the valves (pressure layer). Each layer required a mould, prepared by optical lithography. Briefly, a thin layer of negative photoresist (SU-8 from micro resist technology, Germany) was spun onto a 100 mm silicon wafer. The speed of the spin coating determined the height of the photoresist. After a bake prior to exposure, SU-8 was exposed in a specific pattern to allow crosslinking of SU-8 at the exposed areas. The pattern was defined by a high-resolution mask previously designed in CAD software and printed by Selba S.A. (Switzerland). The mould for the fluid layer with the hydrodynamic and magnetic traps was a SU-8 wafer comprising two heights. The first layer consists of the fluid layer containing the hydrodynamic traps and SU-8 3025 was spin-coated at 3000 rpm to a height of 25 μm. After exposure and post-exposure bake, a second layer of SU-8 3010 was spin-coated onto the liquid layer at 4000 rpm ($\sim$8 μm). After exposure and post-exposure bake, SU-8 was developed in an mr-Dev 600 developer for 5 minutes. The same procedure was used for the preparation of the master mould for the pressure layer. However, it was spun with SU-8 3010 at a speed of 1500 rpm to achieve a final height of 15 μm. The developing time was reduced to 3 minutes. The features on the pressure wafer were designed 1.6% smaller than the fluid layer to account for the shrinking of PDMS during the curing procedure.

3.2.2 Device fabrication

PDMS was prepared by mixing the oligomer and the crosslinking agent (Sylgard 184 silicone elastomer kit, Dow) in a 10:1 ratio. After thoroughly mixing the solution, it was degassed in a vacuum chamber for 15 minutes. The PDMS was poured onto the moulds and cured at 80 °C for a specified time as indicated below. For the fluid layer, 35 g of PDMS was poured onto the wafer to reach a height of about 4 mm. PDMS was then cured for 1.5 hours. The two inlets of the fluid layer were punched with a biopsy punch and the device was cut into the final shape of 4×2 cm with a scalpel. For the pressure layer, 5 g of PDMS was spun onto the second wafer at 2500 rpm. This resulted in a PDMS layer height of approximately 35 μm.

The wafer was then cured for 30 minutes. A plain wafer was used to spin coat a thin layer of crosslinking agent at 6000 rpm. The cured and cut-out fluid devices were dipped into the thin layer of crosslinking agent. A microscope was used to align the fluid device on the pressure layer. After alignment, the fluid device was surrounded by PDMS on the pressure layer to seal it completely. After curing for another 1.5 hours, the device was cut into the desired shape with a scalpel and the four valve inlets of the pressure layer were punched out with a biopsy puncher. The finished devices were then bonded to a microscope slide #3. To prepare for this, the device and slide were cleaned with IPA and a tape, and placed in a plasma oven for 30 seconds. After bonding, the finished device was heated to 100 $^{\circ}C$ for 15 minutes.

3.2.3 Magnet holder

Simulations for the magnetic field were performed using COMSOL Multiphysics 5.3a (COMSOL, Inc). A magnetic field strength of 1 $mA\ m^{-1}$ was assumed for each simulated magnet. All magnets face the same orientation towards the microfluidic chip. The magnet holder was designed in SOLIDWORKS 2018 (Dassault Systèmes) according to the dimensions obtained in the simulation. The CAD design was then 3D printed on an Ultimaker 3 (Ultimaker) using polylactic acid (PLA, Ultimaker).

3.2.4 Cell culture

THP-1 cells, a human leukaemia monocytic cell line, were cultivated at 37 $^{\circ}C$, 5% CO_2, and 95% humidity until confluency was reached. The medium used was Roswell Park Memorial Institute (RPMI) 1640 (Gibco), supplemented with 10% fetal bovine serum (FBS, Gibco), 1× GlutaMAX (Gibco) and 1000 $U\ ml^{-1}$ penicillin/streptomycin (Gibco). 100 $ng\ ml^{-1}$ phorbol 12-myristate 13-acetate (PMA, Merck) was added to the culture for 48 hours to facilitate cell adherence. Then, the medium was switched to serum-free Dulbecco's modified Eagle's medium (DMEM, Gibco) to polarize the cells. DMEM supplemented with 100 $ng\ ml^{-1}$ PMA was added to generate an M0 phenotype, 50 $U\ ml^{-1}$ interferon gamma (INF-γ, Merck) with 1 $\mu g\ ml^{-1}$ lipopolysaccharide (LPS, Sigma Aldrich) generated the M1 phenotype, and 50 $ng\ ml^{-1}$ interleukin-4 (IL-4, Peprotech) with 50 $ng\ ml^{-1}$ interleukin-13 (IL-13, Peprotech) polarized the cells towards the M2 phenotype. The cells were incubated overnight with the individual activation reagents.

Cells were detached by addition of phosphate buffer saline without magnesium and calcium (PBS, Gibco) for 30 minutes and 1× TrypLE^{TM} Express (Gibco) for 10 minutes. After addition of full media and centrifugation for 5 minutes at 500 g, the detached cells were then stained with reagents such as CellTrace^{TM} calcein violet AM and CellROX^{TM} Green (both from Thermo Fisher Scientific) with incubation and concentration ranges as provided by the manufacturer at 37 $°C$. After washing the cells once with PBS, detached cells were supplied into the microfluidic device.

Adhered THP-1 cells were incubated for 72 hours with an upconcentrated MCF-7 derived cell culture supernatant to generate TAM-like cells (M$_{treated}$). MCF-7 cells, which are breast cancer cells, were cultivated on cell culture dishes that were coated with 0.1 $mg\ ml^{-1}$ fibronectin (Merck) in PBS, in DMEM, supplemented with 10% FBS (37 $°C$, 5% CO_2, 95% humidity). Upon confluency, the medium was switched to serum-free DMEM for at least 72 hours. This cell culture supernatant was collected and further upconcentrated from 5 ml to 1 ml using Vivaspin 20, 3000 MWCO PES (Sartorius) for 4 hours at 6000 g. Detachment and staining were done as with the other polarized macrophages.

3.2.5 Optical setup

The fully automated microscope used for the experimental setup was a Ti2 Eclipse (Nikon) with a SOLA SE II (Lumencor) light source and a DIQ2 camera (Nikon) for fluorescence measurements. A temperature box around the microscope provided a stable temperature of 37 $°C$ and an atmosphere chamber provided an atmosphere of 5% CO_2 with a humidity of at least 70%. The objective used for all measurements was a CFI Plan Apochromat Lambda 20× (Nikon). We used filter sets for DAPI and GFP from Nikon. For PE and the two barcode fluorophores, we used custom cubes with filter sets 532/10-552-575/35, 635/10-649-670/30, and 635/10-649-711/25 (emission filter, dichroic mirror, and excitation filter), respectively. The illuminance values for DAPI, GFP, barcode 1, and barcode 2 were set to 2%, 25%, 33%, and 33%, respectively. The exposure times for DAPI, GFP, barcode 1, and barcode 2 were 100 ms, 250 ms, 100 ms, and 100 ms, respectively. The exposure time for PE illumination varied depending on the experiment. For the alamarBlue^{TM} assay, the exposure time was set to 100 ms and the light intensity was set to 15% of the maximum power. For the bead evaluation, the light intensity was set to 50% and the exposure time to 500 ms.

3.2.6 Bulk assay

The protein secreted by the macrophages in the bulk culture was established with ProcartaPlex^{TM} immunoassays (Thermo Fisher Scientific) according to the protocol provided. The fluorescence readout was conducted with the same optical setup used for the evaluation of the ProcartaPlex^{TM} assay on-chip.

3.2.7 Statistical analysis

All statistical evaluations were performed with MATLAB. The boxplots represent the 25th ($q1$) and 75th ($q3$) percentile of the sample with the median in the middle. The whiskers are calculated according to the definitions $q3$ + 1.5 × ($q3$ - $q1$) and $q1$ - 1.5 × ($q3$ - $q1$). The significant difference between distributions was evaluated with the non-parametric Mann-Whitney U test which is used for two independent distributions.

3.2.8 Experimental procedure

The pressure in the pressure layer was controlled by four separately adjustable Flow EZ^{TM} pressure regulators (Fluigent) delivering pressures up to 7 *bar*. The fluid was pressurized using 2 *ml* P-CAPs (Fluigent). In addition, the fluid flow inside the fluid layer was controlled by a high-precision syringe pump (Nemesys, Cetoni) with a 500 μL glass syringe (Agilent). The syringe was connected to the microfluidic chip by 60 *cm* Tygon tubing (Cole Parmer).

The pressure layer was initially filled with DI water by applying a pressure of 500 *mbar* for 5 minutes. Before starting an experiment, the fluid layer was filled and coated with a 4% BSA solution (Sigma Aldrich). The solution was introduced at 200 *mbar* until all bubbles were forced out through the gas permeable PDMS. After degassing, the device was incubated in the BSA solution for 30 minutes.

The magnetic beads with antibodies binding IL-10, TNF-α, and VEGF (Thermo Fisher Scientific, ProcartaPlex^{TM}), respectively, were pooled at stock concentrations before being introduced into the device. The 7.5 μL bead suspension was pipetted into a 200 μL pipette tip and placed on the inlet of the device. The other side of the device (outlet) was connected via tubing to a syringe containing cell media. By withdrawing 7.5 μL at 3 $\mu L\ min^{-1}$ with the syringe, the bead suspension was drawn into the interior of the microfluidic device. After all the beads had been introduced into the chip, the magnetic holder was placed on top of the device and the bead suspension was slowly squeezed out of the chip at 1 $\mu L\ min^{-1}$ for 20 μL. The bead capture is defined by a random process; however, due to the continuous flow, the probability of capturing a bead in a trap was significantly improved. The device was then washed at a flow rate of 100 $\mu L\ min^{-1}$ for 200 μL to remove all beads not captured in the magnetic traps.

Approximately 20 μL of the stained cells were pipetted into a 200 μL pipette tip and placed on the inlet of the device. By withdrawing 20 μL at a rate of 2 $\mu L\ min^{-1}$, the cells were introduced into the device and trapped in the hydrodynamic traps. After 19 μL of the cell suspension was introduced, the pressure valves were slowly closed with a final pressure of 2000 $mbar$. The remaining cells outside the traps were flushed out at 5 $\mu L\ min^{-1}$ for 100 μL. Cells were incubated for 5 hours at 37 °C, 5% CO_2, and a humidity of at least 70%. Cells were imaged immediately after trapping to assess the chamber occupancy and cell integrity. After incubation, the valves were slowly opened with a constant flow of 10 $\mu L\ min^{-1}$.

The syringe containing cell media was replaced with a syringe containing 1× washing buffer of the ProcartaPlex^{TM} assay (Thermo Fisher Scientific). Remaining cells and media were washed out at 100 $\mu L\ min^{-1}$ for 100 μL. Secondary antibodies of the ProcartaPlex^{TM} assay (5×) were added at 3 $\mu L\ min^{-1}$ for 15 μL, and the beads were incubated with the antibodies for 30 minutes. The beads were washed for 100 μL at 5 $\mu L\ min^{-1}$. The SAPE at the stock concentration was added and washed in the same manner as the secondary antibodies. Prior to imaging, the ProcartaPlex^{TM} assay reading buffer was aspirated into the device. Finally, the beads and the chambers were imaged again.

3.3 Results and discussion

3.3.1 Development and optimization of the microfluidic platform

The developed microfluidic platform for quantitative protein detection at the single-cell level consists of 1084 individual microchambers, which can be isolated by the activation of pneumatic valves and contain magnetic as well as hydrodynamic traps (Fig. 3.1a). The method operates as follows: inside each microchamber, specifically designed cavities in the ceiling and a homogenous magnetic field gradient throughout the entire device allow the retention of magnetic beads at predefined positions inside the microchamber (Fig. 3.1b and c,I). The centrally placed hydrodynamic trap captures single cells between two pillars, which are designed for capture of cells with diameters in the range of 20 μm to 40 μm (Fig. 3.1c,II). The cell, the barcoded beads, and its secreted proteins are isolated from other cells by pneumatic valves (green). The pneumatic valves are controlled by applying a pressure of up to

2 *bar* to the lower microchannel system, which closes the fluid layer and, therefore, separates each microchamber from its surrounding (Fig. 3.1c,III). After cell isolation and incubation, the valves are opened, and a standard sandwich immunoassay can be conducted on the beads (Fig. 3.1c,IV). Subsequently, secondary antibodies tagged with a detection fluorophore bind to the protein of interest, which enables the quantitative measurements of the protein based on the fluorescence intensity. Additionally, the beads are fluorescently barcoded, which enables the measurement of multiple proteins at the same time.

To enable brightfield microscopy, we further optimized the placement of the magnets to obtain a homogeneous magnetic field across the microdevice (Fig. 3.2). We simulated various arrangements of magnet geometries and positions to optimize the magnetic flux density in the area of the microfluidic chip (Fig. 3.2c). Based on these simulations, we designed and 3D printed an optimized magnet frame, which mounts 14 neodymium magnets above and around the microfluidic chip, while the central area is left open to enable illumination of the microchamber array (Fig. 3.2b). Additionally, we added five pins to the magnet frame which connect to five holes on the microfluidic platform. This guaranteed an exact placement of the magnets in regard to the microchambers inside the microfluidic device in all three dimensions. We characterized the bead capture efficiency at the concentration provided by the manufacturer and at a volume flow rate of 1 $\mu L\ min^{-1}$. Here we defined the bead capture efficiency as the percentage of the number of traps containing at least one bead. The bead capture efficiency varied in the range of 82% to 91% with an average of 88% (Fig. 3.2d). The cells were introduced into the chip after the beads were captured with a flow rate of 2 $\mu L\ min^{-1}$. The capture efficiency of at least one cell inside a microchamber varied in the range of 40% to 71% with an average of 61% (Fig. 3.2e). The single-cell capture efficiency was lower at an average of 35%, which is primarily due to the propensity of macrophages to cluster in the hydrodynamic traps. Although the probability of having all bead types and exactly one cell in a chamber was low (∼3.4%), the platform provided results from ∼54% (∼585) of all chambers, since chambers with cells co-captured with one or two types of beads are still useful for single-cell analysis.

3.3.2 Characterization of the bead-based assay

To calibrate the fluorescence signal to the protein level, we established the barcode region and the standard dilution curve of various proteins with functionalized beads. Every microchamber was imaged in bright field and epifluorescence

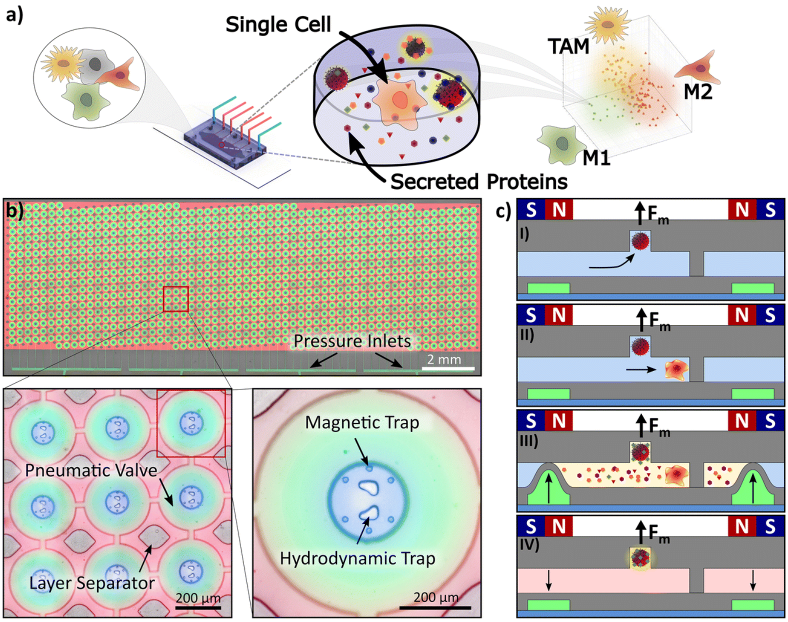

Figure 3.1: Microfluidic platform and procedure for single-immune cell analysis. a) Schematic abstract depicting the microdevice with microchambers to isolate single cells. We determine selected proteins secreted from macrophages treated with the supernatant from cancer cells ($M_{treated}$), and M1- and M2-polarized macrophages. b) Image of the microfluidic platform with 1084 microchambers filled with fluorescent dyes for visualization. Four separate pressure inlets, visible at the bottom of the image as green lines, parallelizing four different experimental conditions on one platform. Left zoomed-in image: Every microchamber has a volume of 0.2 nL (ø = 110 μm) and can be isolated by pneumatically activated valves. The two-layer microfluidic PDMS chip is stabilized by pillars (layer separators). Right zoomed-in image: Inside each microchamber one centrally located hydrodynamic trap is surrounded by six magnetic traps, i.e., six round indents in the ceiling of the chamber. c) Side view of a microchamber to illustrate the procedure; I) each magnetic trap captures exactly one magnetic bead and retains it even if the microfluidic valves are opened. II) The hydrodynamic traps capture single cells depending on their size. III) The hydraulic pressure valves isolate every chamber from surrounding media by deflecting a thin PDMS membrane to the ceiling of the microchannel when pressure is applied. The secreted proteins are captured by the primary antibody immobilized on the bead's surface. IV) After washing and adding secondary antibodies and a detection fluorophore, proteins are quantified based on the fluorescence intensity of the bead.

using an automated microscope (Fig. 3.3a and b). Image analysis was conducted in an automated fashion with MATLAB. The fluorescence intensities in the far-red spectrum were used to determine the barcode of the beads (Fig. 3.3c). For protein quantification based on fluorescence intensity, we conducted experiments with various protein concentrations to obtain calibration curves (Fig. 3.3d). The limit of detection (LOD) was determined by adding the average bead intensities with three

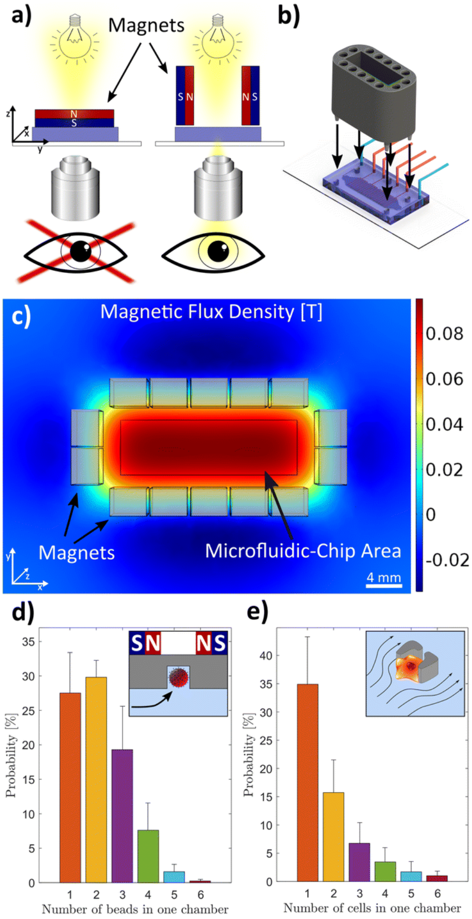

Figure 3.2: Magnet mount and platform characterization. a) The magnets are placed around the microfluidic chip with the same magnetic pole directed towards the centre to increase the magnetic flux density in the region of the chip. b) A 3D-printed magnet mount holds the magnets 4.5 *mm* above the microfluidic chip. Five pins are used to place the mount precisely on the microfluidic chip in reference to the microchambers inside the chip. c) The magnetic flux density in the z-direction is depicted 4.5 *mm* below the magnets. It shows a homogeneous magnetic flux density in the area of the microchambers (black rectangle) which is 4.5 *mm* below the magnets. Each light grey rectangle represents a magnet with dimensions of 3 × 4 × 20 *mm*. d) Occupancy of microchambers with magnetic beads of 6.5 μm diameter. The inset shows a schematic of a magnetic bead trap. e) Occupancy of cells in the microchambers. The inset shows a schematic of a hydrodynamic cell trap.

times their standard deviation at 0 $ng\ mL^{-1}$. The LOD for TNF-α was 0.2 $ng\ mL^{-1}$ which converts into ~1250 molecules per single chamber, and the LODs were 1.5 $ng\ mL^{-1}$ and 0.5 $ng\ mL^{-1}$ for VEGF and IL-10, respectively.

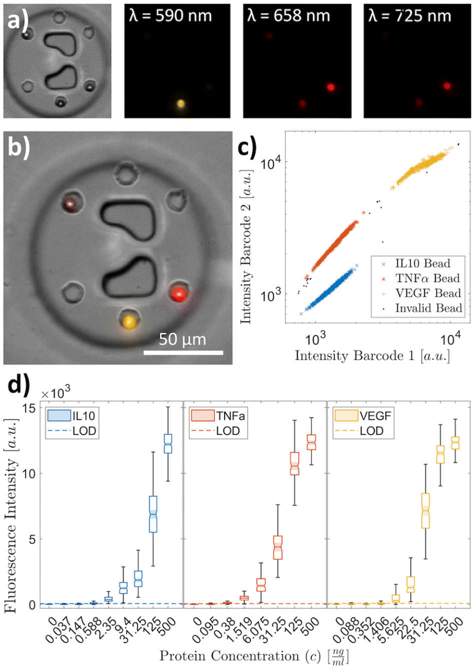

Figure 3.3: Barcoded magnetic beads and calibration curves. a) Microscopy images of a microchamber containing three magnetic beads with different barcodes. Every image is taken at different wavelengths to distinguish between the fluorophores inside the beads as well as the fluorescently tagged detection antibody. The barcode is encoded with fluorophores emitting in the far-red spectrum (658 nm and 725 nm) whereas the readout fluorophore emits in the yellow spectrum (590 nm). b) Overlayed images of a microchamber. c) The barcode of a bead is represented by different intensity ratios in the far-red spectrum. Each region in the 2D plot can be correlated to a primary antibody on the bead. d) On-chip calibration curves for the three investigated proteins. The dashed line indicates the limit of detection (LOD).

The ratio between the volumes of the analyte per functionalized bead is drastically different in our microchambers (~0.2 nL per bead) compared to the bulk assay (~8 nL per bead). Therefore, at the same protein concentration, the number of analytes per bead is 40 times less than in the 96 well plate, resulting in a 40 times lower LOD. Taking this factor into account, the LOD reached on-chip is comparable to the LOD provided by the supplier. The results demonstrate that detection at low concentrations is possible, and we can reliably distinguish between different protein levels up to a concentration of several hundred $ng\ mL^{-1}$. Based on the calibration curves, we can quantify the number of proteins the cell secretes by correlating the fluorescence intensity to the protein concentration.

3.3.3 Confirmation of the cell viability

The metabolic activity of entrapped cells on-chip was tested by adding alamarBlue^{TM} to the media shortly before introducing them into the microfluidic device (Fig. 3.4a). The cells inside the microchamber reduced the resazurin of the alamarBlue^{TM} to resorufin which is brightly fluorescent in the yellow spectrum. Resorufin was contained in the microchamber and up-concentrated because of the isolation of the cells and their secretion product. The images were taken 30 minutes after capturing and isolating the cells, which yielded a clear difference between chambers containing a cell or no cell (Fig. 3.4a). This implied that the cells were alive and still metabolically active after capture and isolation. Furthermore, this result showed that the microchambers isolated the cells and prevented the leakage of alamarBlue^{TM} from one chamber to the next. This was additionally confirmed by secretion measurements of chambers containing at least one cell and chambers without any cell (Fig. 3.7). The chambers without cells showed readouts below the detection limit of the assay implying no cross contamination of the pneumatically activated valves from the highly secreting cells in neighbouring chambers.

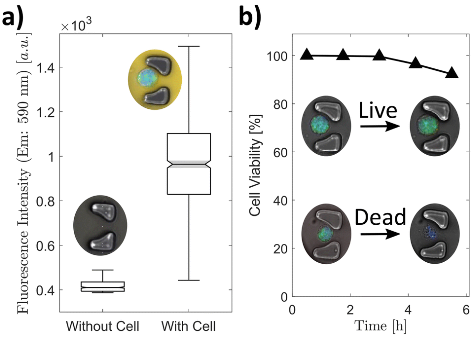

Figure 3.4: On-chip metabolic activity and cell viability. a) alamarBlue^{TM}, a fluorogenic assay, was used to visualize the metabolic activity of the cell on-chip. b) The cell viability on-chip was established by observing the membrane permeability with a live cell stain (blue) and a stain for ROS (green), n = 663.

We measured the intracellular reactive oxygen species (ROS) of macrophages in bulk culture (off-chip) and isolated them in microchambers (on-chip) to analyse the stress response of the cell after capturing and compartmentalization (Fig. 3.8). The ROS level of the cell in the bulk culture is slightly higher than in the cells captured in the microchambers. This is largely due to unspecific ROS contained in the media which increases the overall readout signal. For automatic cell recognition, we added a viability stain to brightly stain living and membrane-intact cells. Both stains were utilized to establish the membrane permeability of the cells over an extended period (Fig. 3.4b). The cells with a permeable, leaky membrane showed no fluorescence after more than 5 hours whereas the cells with an intact membrane showed a still high fluorescence signal. After this incubation time, 92% of the cells had an intact membrane.

3.3.4 Polarization of the macrophages

Unpolarized macrophages were derived from the THP-1 cell line and further activated to the M1 phenotype and the M2 phenotype by adding INF-γ/LPS and IL-4/IL-13 for 12 h, respectively (Fig. 3.5a). We were able to distinguish the differently polarized macrophages based on their secretion profile measured in the bulk culture media (Fig. 3.5b, Fig. 3.9 and Fig. 3.10). As expected, the M1 macrophages show an increased secretion of TNF-α ($p < 0.001$) whereas the M2 macrophages secrete more IL-10 ($p < 0.001$) compared to the unpolarized macrophages (control). All three phenotypes secreted VEGF, with secretion highest in the M1 macrophages. This is interesting, as VEGF promotes angiogenesis and hence tumour growth. Our observation is in accordance with prior findings. The use of LPS for polarization has been shown to lead to increased VEGF secretion (see also Fig. 3.10 depicting the results for alternative polarization conditions)[34].

3.3.5 On-chip secretion studies

Next, we captured, isolated, and incubated the polarized macrophages on the microfluidic platform and measured the secreted signalling proteins from single cells (Fig. 3.6a and b). Due to the extreme sensitivity of the platform, we were able to characterize the macrophages according to their polarization. The M1 macrophages show a high TNF-α secretion (median: 2.23 $ng\ mL^{-1}$) as in the bulk culture and are clearly distinguishable from the M2 macrophages based on this secretion. In contrast, the secretion of IL-10 by the M2 macrophages (median: 0.78 $ng\ mL^{-1}$) is not significantly higher than that of the M1 macrophages (median: 0.75 $ng\ mL^{-1}$). The

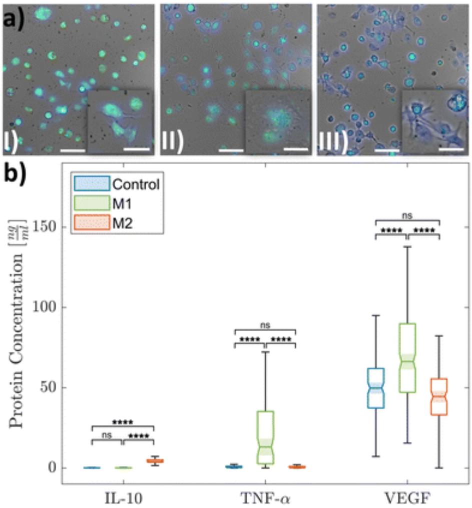

Figure 3.5: Macrophage differentiation. a) Microscopy images of unpolarized macrophages (control) (I), M1 macrophages (II), and M2 macrophages (III) (green: ROS stain, blue: live cell stain). The scale bars in the images are 100 μm and in the insets 50 μm. b) Protein secretion of the differentiated macrophages evaluated with an on-bead immunoassay from the bulk culture supernatant (N = 3, pooled).

reduced IL-10 secretion of the M2 macrophages can be explained by the isolation of single cells, preventing the effect of paracrine signalling from the bulk population, which can impact the secretion of signalling proteins [35].

Additionally, we incubated unpolarized macrophages in the up-concentrated supernatant of breast cancer cells (MCF-7 cell line) to simulate the impact of the TME on the polarization of macrophages [36]. These macrophages show a protein pattern similar to M2 macrophages with a significantly increased expression of all measured proteins (median IL-10: 1,12 $ng\ mL^{-1}$, TNF-α: 1.43 $ng\ mL^{-1}$, VEGF: 4.81 $ng\ mL^{-1}$). Notably, the MCF-7 secretome is missing the factors commonly used to polarize macrophages (i.e., INF-γ, IL-4, and IL-13) [3]; however, it contains a high level of VEGF (Fig. 3.11). In the TME, VEGF secreted from the cancer cells supports the recruitment of macrophages, which are subsequently polarized towards M2-like macrophages (TAMs) [37, 38]. Therefore, we hypothesize that the VEGF from MCF-7 cells is a factor that is involved in the polarization of the macrophages towards TAMs. In addition, and in line with previous observations [36], TAMs secrete in turn higher amounts of VEGF when polarized in VEGF-containing media compared to polarization in VEGF-depleted media.

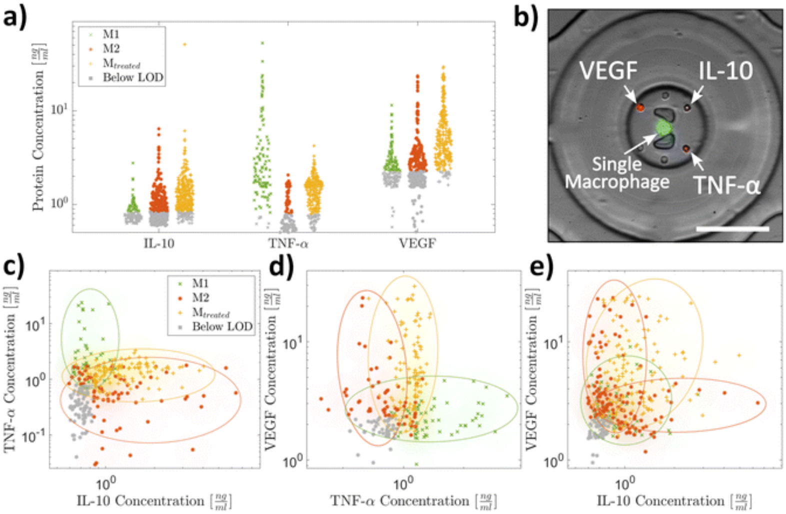

Figure 3.6: The macrophage characterization based on single-cell protein secretion. a) The proteins secreted by captured and isolated macrophages were measured with an immunoassay. The grey datapoints show secretion values below the detection limit ($n \geq 114$). M1 macrophages and M2 macrophages are polarized by the addition of defined signalling factors, whereas macrophages polarized by the culture medium from cancer cells are denoted as $M_{treated}$. b) A microscopy image of an example microchamber containing one macrophage with three different bead types. c)-e) show the multiplex expression of the proteins from single macrophages ($n \geq 47$, $n \geq 74$, and $n \geq 66$). The colour overlays are the regions in which most of the datapoints of the corresponding cells are located. Outliers are not depicted (Fig. 3.12 includes all datapoints).

Multiplexed analysis highlights the correlations between signalling molecules in individual cells, which is only possible by single-cell analysis. (Fig. 3.6c-e and 3D plot in Fig. 3.13). Secretion of the tumour suppressive protein TNF-α is upregulated when the tumour-promoting proteins IL-10 and VEGF are low (Fig. 3.6c and d). Conversely, the tumour-promoting proteins IL-10 and VEGF are more highly expressed in cells that do not express the tumour-suppressive protein TNF-α. The M2 macrophages mostly secrete either IL-10 or VEGF at higher amounts but not at the same time which indicates that there are at least two subpopulations of M2 macrophages. This contrasts with the macrophages treated with the breast cancer supernatant ($M_{treated}$) which mostly secreted both at the same time (Fig. 3.6e).

These results demonstrate that our system is well suited to analyse low-abundance secreted proteins at the single-cell level, which we showed by distinguishing between polarized macrophages. The hydrodynamic traps enabled the tag free capture of single cells whereas the optimized magnet mount permitted the simultaneous retention and observation of the beads and cells. The capturing of magnetic beads in small cavities facilitated the automation of imaging and improved signal acquisition. The developed platform showed its capability to study macrophages subjected to cancer cell-derived signalling factors which will deepen the understanding of cell-to-cell signalling and the role of macrophages in tumour progression. However, the limitation of the platform was the random trapping of beads in the small magnetic traps, which can be improved by increasing the number of magnetic traps per chamber or increasing the bead concentration.

3.4 Conclusion

Macrophage polarization towards TAMs as well as the resulting changes in the signalling proteins is a highly complex process. It is well-known that macrophages are not a uniform population, and detection of subpopulations requires analysis at the single-cell level. Here, we introduce a microfluidic method for capturing polarized macrophages and the analysis of selected signalling proteins. As we isolate cells, paracrine signalling is prevented at the time of accumulation of the signalling proteins. We confirm that M1, M2, and macrophages treated with the supernatant from cancer cells can be distinguished by their secretion profile, but we also find a very heterogeneous population on the individual cell level with cells secreting at high levels and others without detectable signalling proteins. Besides the analysis of macrophages, the microfluidic device is very versatile and can be used for other cell types and the analysis of other secreted factors or exosomes at the single-cell level. The combination of hydrodynamic traps for size-based cell capturing and magnetic traps for immobilization of beads enables efficient co-encapsulation of cells and functionalized beads. The high sensitivity of immunoassays in a pL chamber allows for accumulation and quantification of proteins secreted at very low levels. There is a growing library of commercially available magnetic beads with many different barcodes for numerous targets. Coupled to the method presented herein, this will allow for multiplexed and quantitative measurement of a variety of different signalling proteins at the single-cell resolution.

3.5 Author contributions

C. D. designed and fabricated the device, performed all experiments on-chip and evaluated all data. E. H. provided the macrophages and performed the off-chip characterization. P. S. D. conceptualized and supervised the work. C. D. and P. S. D. wrote the manuscript.

3.6 Acknowledgements

We thank R. Strutt for proofreading the manuscript. We thank the cleanroom facility (ETH Zurich) for access and support. Financial support of the European Research Council (ERC CoG No. 681587) and Personalized Medicine Basel (Grant No. PMB-02-19) is gratefully acknowledged.

3.7 Supplementary information

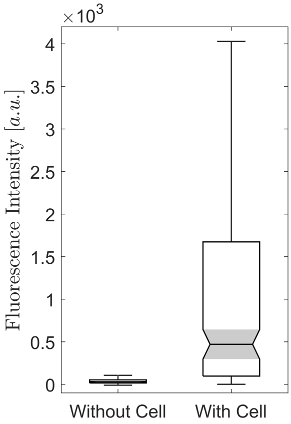

Figure 3.7: Protein secretion measured in chambers containing at least one cell compared to chambers containing no cell in the same microfluidic chip. The signal in chambers without a cell is very low. We also do not observe diffusion of analytes from a cell-occupied chamber to an adjacent empty chamber, when the pneumatic valves are closed.

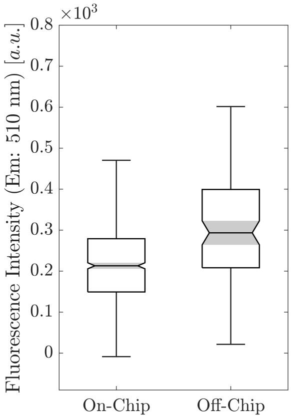

Figure 3.8: The ROS level in the cells was measured in bulk (off-chip) and in the microchambers (onchip) with CellROX^{T}M Green.

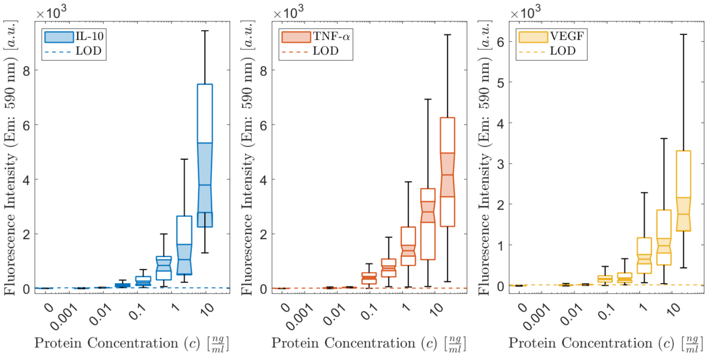

Figure 3.9: Calibration curves of the three target proteins measured in a volume of 50 μL on a plate reader. The LODs of the proteins are 0.015 $ng\ mL^{-1}$, 0.01 $ng\ mL^{-1}$, and 0.015 $ng\ mL^{-1}$ for IL-10, TNF-α, and VEGF, respectively

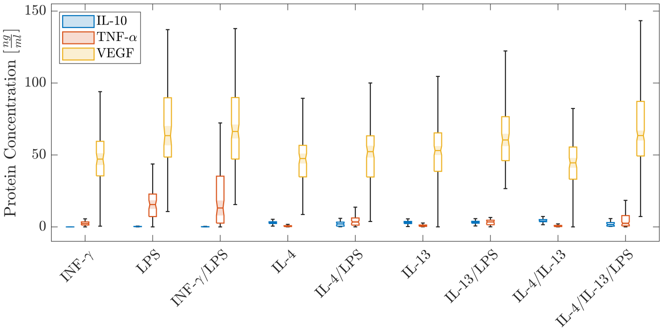

Figure 3.10: Secretion of IL-10, TNF-α, and VEGF from macrophages polarized with different compounds according to the protocol in the main manuscript.

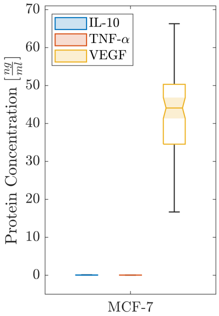

Figure 3.11: Off-chip secretome analysis of the breast cancer cell line MCF-7.

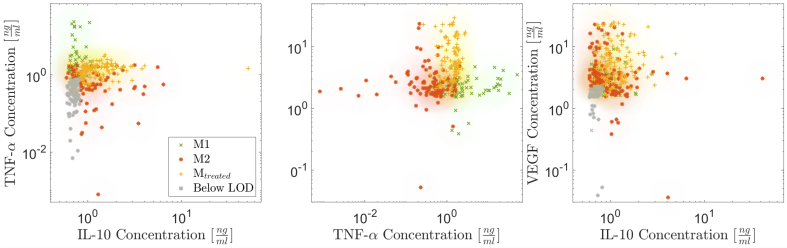

Figure 3.12: Multiplex expression of the proteins from single macrophages. The plotted data is the same data as in Figure 6c-e including all the outliers.

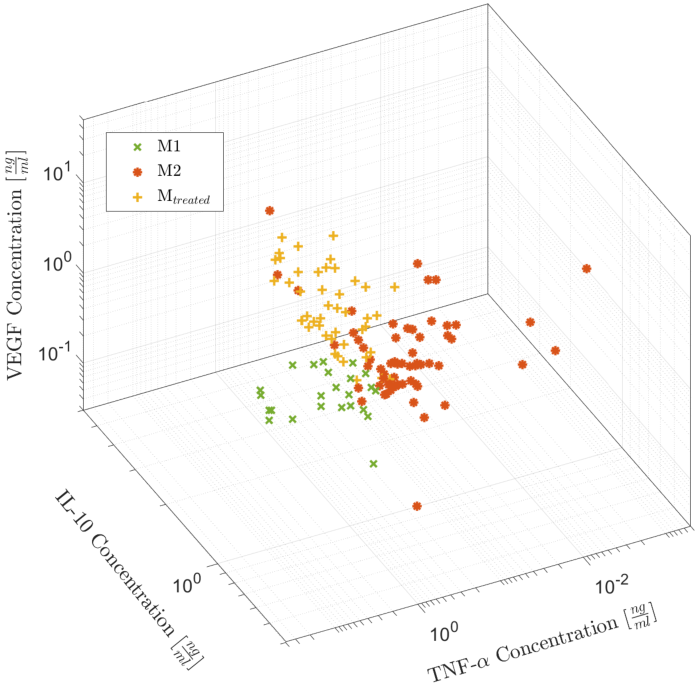

Figure 3.13: Single-cell secretion profile of polarized macrophages and macrophages treated with supernatant from cancer cells ($M_{treated}$). The secretion levels of macrophages are depicted for microchambers, where a single cell was co-encapsulated with all three types of beads. Green symbols: M1-polarized macrophages (n=24), red symbols: M2-polarized macrophages (n=68), yellow symbols: $M_{treated}$ (n=45).

3.8 References

[1] G. Altan-Bonnet and R. Mukherjee, «Cytokine-mediated communication: a quantitative appraisal of immune complexity», Nature Reviews Immunology **19**, 205–217 (2019).

[2] P. Jiang, Y. Zhang, B. Ru, Y. Yang, T. Vu, R. Paul, A. Mirza, G. Altan-Bonnet, L. Liu, E. Ruppin, L. Wakefield, and K. W. Wucherpfennig, «Systematic investigation of cytokine signaling activity at the tissue and single-cell levels», Nature Methods **18**, 1181–1191 (2021).

[3] K. Chen, L. Satlof, G. Stoffels, U. Kothapalli, N. Ziluck, M. Lema, L. Poretsky, and D. Avtanski, «Cytokine secretion in breast cancer cells - milliplex assay data», Data in Brief **28**, 104798 (2020).

[4] C. Varol, A. Mildner, and S. Jung, «Macrophages: development and tissue specialization», Annual Review of Immunology **33**, 643–675 (2015).

[5] M. Gerlinger, A. J. Rowan, S. Horswell, J. Larkin, D. Endesfelder, E. Gronroos, P. Martinez, N. Matthews, A. Stewart, P. Tarpey, I. Varela, B. Phillimore, S. Begum, N. Q. McDonald, A. Butler, D. Jones, K. Raine, C. Latimer, C. R. Santos, M. Nohadani, A. C. Eklund, B. Spencer-Dene, G. Clark, L. Pickering, G. Stamp, M. Gore, Z. Szallasi, J. Downward, P. A. Futreal, and C. Swanton, «Intratumor heterogeneity and branched evolution revealed by multiregion sequencing», New England Journal of Medicine **366**, 883–892 (2012).

[6] A. P. Patel, I. Tirosh, J. J. Trombetta, A. K. Shalek, S. M. Gillespie, H. Wakimoto, D. P. Cahill, B. V. Nahed, W. T. Curry, R. L. Martuza, D. N. Louis, O. Rozenblatt-Rosen, M. L. Suvà, A. Regev, and B. E. Bernstein, «Single-cell rna-seq highlights intratumoral heterogeneity in primary glioblastoma», Science **344**, 1396–1401 (2014).

[7] X. Geeraerts, E. Bolli, S.-M. Fendt, and J. A. V. Ginderachter, «Macrophage metabolism as therapeutic target for cancer, atherosclerosis, and obesity», Frontiers in Immunology **8**, 289 (2017).

[8] T. Hourani, J. A. Holden, W. Li, J. C. Lenzo, S. Hadjigol, and N. M. O'Brien-Simpson, «Tumor associated macrophages: origin, recruitment, phenotypic diversity, and targeting», Frontiers in Oncology **11**, 788365 (2021).

[9] Y. Pan, Y. Yu, X. Wang, and T. Zhang, «Tumor-associated macrophages in tumor immunity», Frontiers in Immunology **11**, 583084 (2020).

[10] P. J. Murray, J. E. Allen, S. K. Biswas, E. A. Fisher, D. W. Gilroy, S. Goerdt, S. Gordon, J. A. Hamilton, L. B. Ivashkiv, T. Lawrence, M. Locati, A. Mantovani, F. O. Martinez, J.-L. Mege, D. M. Mosser, G. Natoli, J. P. Saeij, J. L. Schultze, K. A. Shirey, A. Sica, J. Suttles, I. Udalova, J. A. van Ginderachter, S. N. Vogel, and T. A. Wynn, «Macrophage activation and polarization: nomenclature and experimental guidelines», Immunity **41**, 14–20 (2014).

[11] L.-x. Wang, S.-x. Zhang, H.-j. Wu, X.-l. Rong, and J. Guo, «M2b macrophage polarization and its roles in diseases», Journal of Leukocyte Biology **106**, 345–358 (2019).

[12] B. Ruffell, D. Chang-Strachan, V. Chan, A. Rosenbusch, C. M. Ho, N. Pryer, D. Daniel, E. S. Hwang, H. S. Rugo, and L. M. Coussens, «Macrophage il-10 blocks cd8+ t cell-dependent responses to chemotherapy by suppressing il-12 expression in intratumoral dendritic cells», Cancer Cell **26**, 623–637 (2014).

[13] J. Zhou, Z. Tang, S. Gao, C. Li, Y. Feng, and X. Zhou, «Tumor-associated macrophages: recent insights and therapies», Frontiers in Oncology **10**, 188 (2020).

[14] Z. Duan and Y. Luo, «Targeting macrophages in cancer immunotherapy», Signal Transduction and Targeted Therapy **6**, 127 (2021).

[15] P. Pathria, T. L. Louis, and J. A. Varner, «Targeting tumor-associated macrophages in cancer», Trends in Immunology **40**, 310–327 (2019).

[16] Z. X. Liao, Y. C. Fa, I. M. Kempson, and S. J. Tseng, «Repolarization of m2 to m1 macrophages triggered by lactate oxidase released

from methylcellulose hydrogel», Bioconjugate Chemistry **30**, 2697–2702 (2019).

[17] R. N. Zare and S. Kim, «Microfluidic platforms for single-cell analysis», Annual Review of Biomedical Engineering **12**, 187–201 (2010).

[18] S. F. Berlanda, M. Breitfeld, C. L. Dietsche, and P. S. Dittrich, «Recent advances in microfluidic technology for bioanalysis and diagnostics», Analytical Chemistry **93**, 311–331 (2021).

[19] L. Chappell, A. J. Russell, and T. Voet, «Single-cell (multi)omics technologies», Annual Review of Genomics and Human Genetics **19**, 15–41 (2018).

[20] S. Vyawahare, A. D. Griffiths, and C. A. Merten, «Miniaturization and parallelization of biological and chemical assays in microfluidic devices», Chemistry and Biology **17**, 1052–1065 (2010).

[21] P. S. Dittrich and A. Manz, «Lab-on-a-chip: microfluidics in drug discovery», Nature Reviews Drug Discovery **5**, 210–218 (2006).

[22] E. Z. Macosko, A. Basu, R. Satija, J. Nemesh, K. Shekhar, M. Goldman, I. Tirosh, A. R. Bialas, N. Kamitaki, E. M. Martersteck, J. J. Trombetta, D. A. Weitz, J. R. Sanes, A. K. Shalek, A. Regev, and S. A. McCarroll, «Highly parallel genome-wide expression profiling of individual cells using nanoliter droplets», Cell **161**, 1202–1214 (2015).

[23] V. Chokkalingam, J. Tel, F. Wimmers, X. Liu, S. Semenov, J. Thiele, C. G. Figdor, and W. T. Huck, «Probing cellular heterogeneity in cytokine-secreting immune cells using droplet-based microfluidics», Lab on a Chip **13**, 4740–4744 (2013).

[24] Y. Bounab, K. Eyer, S. Dixneuf, M. Rybczynska, C. Chauvel, M. Mistretta, T. Tran, N. Aymerich, G. Chenon, J. F. Llitjos, F. Venet, G. Monneret, I. A. Gillespie, P. Cortez, V. Moucadel, A. Pachot, A. Troesch, P. Leissner, J. Textoris, J. Bibette, C. Guyard, J. Baudry, A. D. Griffiths, and C. Védrine, «Dynamic single-cell phenotyping of immune cells using the microfluidic platform dropmap», Nature Protocols **15**, 2920–2955 (2020).

[25] M. N. Hsu, S.-C. Wei, S. Guo, D.-T. Phan, Y. Zhang, and C.-H. Chen, «Smart hydrogel microfluidics for single-cell multiplexed secretomic analysis with high sensitivity», Small **14**, 1802918 (2018).

[26] D. M. Rissin, C. W. Kan, T. G. Campbell, S. C. Howes, D. R. Fournier, L. Song, T. Piech, P. P. Patel, L. Chang, A. J. Rivnak, E. P. Ferrell, J. D. Randall, G. K. Provuncher, D. R. Walt, and D. C. Duffy, «Single-molecule enzyme-linked immunosorbent assay detects serum proteins at subfemtomolar concentrations», Nature Biotechnology **28**, 595–599 (2010).

[27] J. R. Choi, J. H. Lee, A. Xu, K. Matthews, S. Xie, S. P. Duffy, and H. Ma, «Monolithic hydrogel nanowells-in-microwells enabling simultaneous single cell secretion and phenotype analysis», Lab on a Chip **20**, 4539–4551 (2020).

[28] X. An, V. G. Sendra, I. Liadi, B. Ramesh, G. Romain, C. Haymaker, M. Martinez-Paniagua, Y. Lu, L. G. Radvanyi, B. Roysam, and N. Varadarajan, «Single-cell profiling of dynamic cytokine secretion and the phenotype of immune cells», PLoS ONE **12**, e0181904 (2017).

[29] L. Armbrecht and P. S. Dittrich, «Recent advances in the analysis of single cells», Analytical Chemistry **89**, 2–21 (2017).

[30] L. Armbrecht, R. S. Müller, J. Nikoloff, and P. S. Dittrich, «Single-cell protein profiling in microchambers with barcoded beads», Microsystems and Nanoengineering **5**, 55 (2019).

[31] Y. Lu, J. J. Chen, L. Mu, Q. Xue, Y. Wu, P. H. Wu, J. Li, A. O. Vortmeyer, K. Miller-Jensen, D. Wirtz, and R. Fan, «High-throughput secretomic analysis of single cells to assess functional cellular heterogeneity», Analytical Chemistry **85**, 2548–2556 (2013).

[32] A. J. Kaestli, M. Junkin, and S. Tay, «Integrated platform for cell culture and dynamic quantification of cell secretion», Lab on a Chip **17**, 4124–4133 (2017).

[33] Y. Lu, Q. Xue, M. R. Eisele, E. S. Sulistijo, K. Brower, L. Han, E. A. D. Amir, D. Pe'er, K. Miller-Jensen, and R. Fan, «Highly multiplexed profiling of single-cell effector functions reveals deep functional heterogeneity in response to pathogenic ligands», Pro-

ceedings of the National Academy of Sciences of the United States of America **112**, E607–E615 (2015).

[34] N. Koide, E. Odkhuu, Y. Naiki, B. Tsolmongyn, K. Ito, T. Komatsu, T. Yoshida, and T. Yokochi, «Augmentation of lps-induced vascular endothelial cell growth factor production in macrophages by transforming growth factor-b1», Innate Immunity **20**, 816–825 (2014).

[35] Q. Xue, Y. Lu, M. R. Eisele, E. S. Sulistijo, N. Khan, R. Fan, and K. Miller-Jensen, «Analysis of single-cell cytokine secretion reveals a role for paracrine signaling in coordinating macrophage responses to tlr4 stimulation», Science Signaling **8**, ra59 (2015).

[36] S. Okikawa, Y. Morine, Y. Saito, S. Yamada, K. Tokuda, H. Teraoku, K. Miyazaki, S. Yamashita, T. Ikemoto, S. Imura, and M. Shimada, «Inhibition of the vegf signaling pathway attenuates tumor-associated macrophage activity in liver cancer», Oncology Reports **47**, 71 (2022).

[37] M. L. Squadrito and M. D. Palma, «Macrophage regulation of tumor angiogenesis: implications for cancer therapy», Molecular Aspects of Medicine **32**, 123–145 (2011).

[38] J. S. Lewis, R. J. Landers, J. C. E. Underwood, A. L. Harris, and C. E. Lewis, «Expression of vascular endothelial growth factor by macrophages is up-regulated in poorly vascularized areas of breast carcinomas», The Journal of Pathology **192**, 150–158 (2000).

Chapter 4

Wells-in-well microarray for multiplexed and quantitative analysis of cytokines from single macrophages

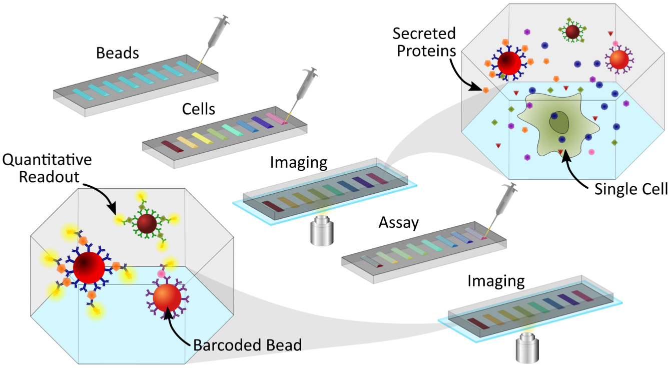

Authors: **Claudius L. Dietsche**
Lucien Stöcklin
Raphal Dezauzier
Robert Strutt
Petra S. Dittrich
Published: In preparation (2024)

Wells-in-well microarray for multiplexed and quantitative analysis of cytokines from single macrophages

Claudius L. Dietsche[1], Lucien Stöcklin[1], Raphael Dezauzier[1], Robert Strutt[1], and Petra S. Dittrich[1,*]

[1]Department of Biosystems Science and Engineering, Schanzenstrasse 44, 4056 Basel, Switzerland
*petra.dittrich@bsse.ethz.ch

Macrophages play a critical role in the development of the tumour microenvironment (TME). Recruited macrophages are affected by secreted proteins from the TME to differentiate predominantly into a tumour-supportive phenotype of macrophages. The vast variety of cells and phenotypes in the TME, and the even more complex signaling between cells based on secreted cytokines, requires novel tools to quantify proteins secreted from single cells. Here, we have developed a wells-in-well array for the multiplexed analysis of secreted proteins of up to 10^5 single cells. We use a cyclic olefin copolymer (COC) device with more than 100'000 wells, each of which has seven smaller indents for co-capturing functionalized beads. These barcoded beads capture cytokines of interest and allow their quantitative analysis by sandwich immunoassay. The microwell array is operated using only standard laboratory equipment such as pipettes and microscopes. With the developed device, we were able to characterize profiles of secreted proteins and investigate the impact of different stimuli on the secretion pattern. We found that interleukin 1β (IL-1β), IL-8, and macrophage inflammatory protein 1α (MIP-1α/CCL3) were highly secreted by more than 43% of the macrophages with an increase of MIP-1α when stimulated with the chemotherapeutic drugs, paclitaxel or docetaxel. Multiplexed measurements confirmed co-secretion of IL-1β and IL-6 in the macrophages stimulated with IL-4/IL-13 which prove that the developed device is capable to facilitate the search for novel drug targets. In summary, we showed that the developed device is an easy-to-use analytical tool that can be applied in basic research, diagnostics, and personal medicine.

4.1 Introduction

Macrophages, an important part of the immune system, use paracrine signalling of cytokines to activate various functions of the immune system [1]. Specifically, in the tumour microenvironment (TME) macrophages play a crucial role [2]. The highly plastic macrophages can respond to stimuli from their environment and adapt their phenotype accordingly [1, 3]. The heterogeneity of the TME results in diverse stimuli for individual macrophages resulting in a range of different phenotypes. Two extreme phenotypes of macrophages are well studied in the TME: the pro-inflammatory phenotype, also known as M1 macrophages, have an anti-tumoural impact on the tumour progression and the anti-inflammatory phenotype, also known as M2 macrophages, have a pro-tumoral impact [3, 4]. Undifferentiated macrophages are polarized to the M1 phenotype by stimuli such as lipopolysaccharide (LPS) and interferon γ (INF-γ) whereas interleukin 4 (IL-4) and IL-13 stimulates macrophages towards a more M2-like phenotype [3, 5]. M1 macrophages secrete mainly pro-inflammatory proteins such as IL-1β, IL-6, IL-8, or tumour necrosis factor α (TNF-α) whereas M2 macrophage secrete cytokines such as macrophage inflammatory protein-4 (MIP-4/CCL18) or vascular endothelial growth factor A (VEGF) [3, 5–7]. Macrophages are known to adapt to stimuli from the TME but also change their phenotype in response to various anti-cancer drugs [4, 8, 9]. Recently, it was shown that taxanes, a chemotherapeutic drug against various cancer types, change the macrophages towards the pro-inflammatory phenotype, aiding the tumour regression [9]. Here, we investigate the secretion profile of the highly plastic macrophages at the single-cell level in response to anti-cancer drugs which is important for the development of innovative and efficient cancer treatments.

Microfluidic technology provides well-suited tools for the analysis of secreted proteins at the single-cell level [10, 11]. To prevent cross-contamination between cells, the individual cells are completely isolated from each other, e.g., by means of (i) droplet microfluidics [12–18], (ii) microchambers [19–23], or (iii) microwells [24–28]. (i) In droplet microfluidics, single cells are encapsulated in water-in-oil emulsions, and cytokines secreted from the cells are accumulating within the aqueous droplets. The fluorescence readout is usually based on a re-localisation immunoassay capturing the secreted proteins on functionalized microspheres [12, 14] or magnetic nanoparticles [15, 17, 18]. Mostly, all reagents are encapsulated during droplet generation enabling time resolved secretion measurements from the cells [15, 18]. (ii) In contrast, microchambers isolate single cells in closed compartments and spatially separate the cells. A highly versatile and flexible method to segregate single cells uses actively controlled pneumatic valves, shaped like a ring, to form a round microchamber with a cell trapped in its centre [19, 21–23]. The precise control of the fluid flow enables specific reagent exchange and washing steps for more sophisticated assays. In recent studies, commercially available barcoded beads were introduced to enable multiplexed on-bead immunoassays inside of microchambers [21, 22]. (iii) Microwells can be realized in different ways. A well-developed platform, the single-cell barcode chip (SCBC), stochastically captures cells in PDMS wells and seals them with a glass slide [19, 20, 29, 30]. The glass slide is patterned with an antibody barcode enabling multiplexed measurements of up to 42 proteins from each cell [20]. The secreted proteins are up-concentrated in the small volume of the microchambers and are quantified by a sandwich immunoassays. A novel technology, lab on a particle, was recently developed to measure cytokines secreted by single cells trapped on a cavity-containing hydrogel particle [31, 32]. The hydrogel particles containing the cells can be encapsulated in oil, washed, and sorted based on the protein secretion. Open microwells have a high throughput and are generally easy to operate [24, 25, 27, 28]. The cells are captured and held in place by gravity in the open well-like compartments. The secreted proteins are captured in proximity of the cell either on the surface of the microwell [25, 27] or the surface of a co-captured bead [26, 28].

In this study, we developed and optimized a ultra-high density, easy-to-use microwell array for the quantitative measurement of secreted cytokines from individual macrophages and investigated their phenotype in response to various stimuli. The microwell array consists of 100’992 hexagonal wells, with a density as high as 415 wells per mm^2. We integrated smaller wells in the larger well to co-capture single cells and magnetic beads. Cells and beads remain at these defined sites, which allows for fast imaging and simplifies the data analysis. Multiple secreted proteins from cells are measured using a commercially available on-bead sandwich immunoassay at levels down to 1136 molecules per well. With the proposed system, we showed the secretion pattern of macrophages at the single-cell level, studied the impact of anti-cancer drugs, and explored the correlation between more than 40 pairs of proteins.

4.2 Results and discussion

4.2.1 Development and characterization of the microwell array

The developed microfluidic system contains 100’992 individual wells to analyse the secreted proteins from single cells with an on-bead immunoassay (Fig. 4.1). The wells are spatially separated in eight distinct areas which are suited to conduct different experimental conditions in parallel (Fig. 4.2a). Between the areas, a drainage system was introduced which consists of 250 μm wide trenches. Each condition

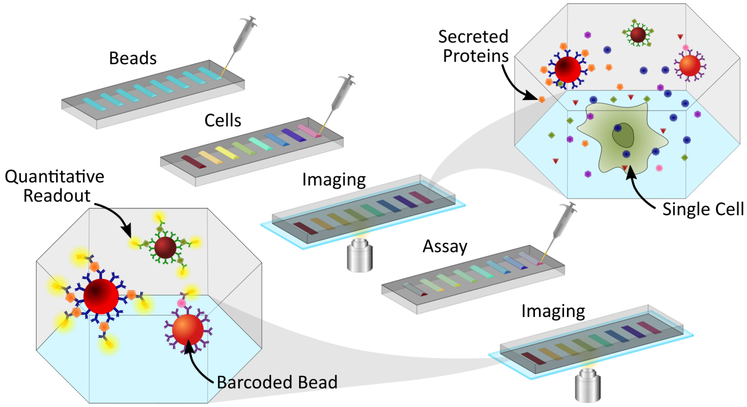

Figure 4.1: Conceptual abstract of the developed well-in-well microarray device for the quantitative analysis of secreted proteins from single cells. Functionalized magnetic beads are pipetted into the 100’992 wells. Individual cells are isolated with the functionalized beads and incubated in up to eight different conditions. The secreted proteins are captured with a multiplexed on-bead immunoassay, imaged by a fully automated microscope, and finally quantified by an image analysis software.

contains 12’624 hexagonal shaped wells with a side length of 20 μm. The wells are separated by a thin wall of 20 μm on every side resulting in a well density of 415 $wells\ mm^{-2}$. Each well contains seven indents ($\varnothing$ = 7.5 μm) to capture and retain magnetic beads with a diameter of 6.5 μm. Initially, the beads are loaded on each condition of the device by pipetting (Fig. 4.2b). A magnet, which is placed beneath the device, prevents the magnetic beads from escaping the magnetic traps. After washing, the cells are introduced with the same method. The device is submerged in a fluorinated oil bath and the wells are isolated by removing the excess aqueous phase with a pipette. For the incubation and imaging of the cells, the device is rotated 180ř and placed on the microscope. To perform the immunoassay after the incubation, the device is removed from the oil bath, all cells are washed away, and the secondary antibody mix and readout fluorophore are pipetted on each condition. Finally, the device with the beads is imaged upside down.

We characterized the developed device regarding well occupancy with beads and cells; the bead retention during washing steps; cross contamination between conditions and individual wells; and the cell viability and metabolic activity on the device (Fig. 4.3). The number of captured beads per well increases with the bead concentration (Fig. 4.3a). At the maximum tested concentration of 5.5×10^6 beads per millilitre, 90% of all wells contains at least one bead with the highest probabil-

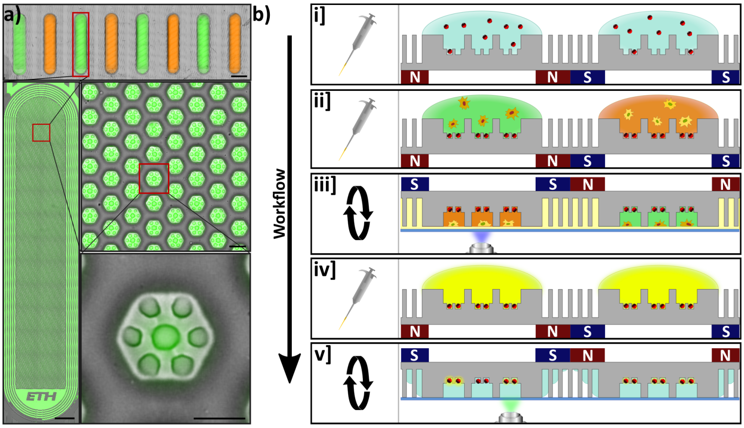

Figure 4.2: Design and workflow of the well-in-well microarray device. a) Microscopy images of the microwell array. Each device contains 100'992 hexagonal wells which are designed to achieve a high well density and favour single-cell capture. In each well, seven small indents are utilized to co-capture functionalized magnetic beads to immobilize and analyse secreted proteins. The device is designed to perform up to eight different experimental conditions at the same time. The scale bars represent 4 *mm*, 1 *mm*, 40 *µm*, and 20 *µm*. b) i] The commercially available magnetic beads are pipetted on the device and retained by a magnet placed beneath the microarray. ii] The cells are pipetted on each condition area and captured by the hexagonal cell traps. iii] The wells are 'sealed' by placing the microwell array in an HFE oil bath and removing the excess aqueous solution. During the incubation, the device is turned around and imaged by an inverted microscope. iv] The oil is removed, and the device is turn back around to perform the immunoassay with the magnetic beads. v] Finally, the beads are images with a fully automated microscope.

ity (20%) of having four beads in one chamber (Fig. 4.3b). The capture efficiency of beads solely relies on the concentration of beads used and can be adapted according to the experiment conducted. We observed the same pattern with the capture probability of the cell number in each well (Fig. 4.3c). At a concentration of 1×10^6 cells per millilitre, a third of all wells contain a single cell. However, at concentrations above 1×10^6 cells per millilitre, the probability of capturing two cells in one well increases proportionally more than the probability of capturing only a single cell. At the highest concentration of cells, 93% of all wells contain at least one cell and up to 69% at a concentration of 1×10^6 (Fig. 4.3d). We imaged the beads of a device before and after several washing steps and evaluated the read retention after each step (Fig. 4.3e). We found that the bead retention is around 99% implying that all beads are retained during the washing procedure. The slight mismatch ($\sim$1%) is mainly due to image processing errors during the data evaluation.

A critical parameter of microwell arrays is the isolation of each well preventing

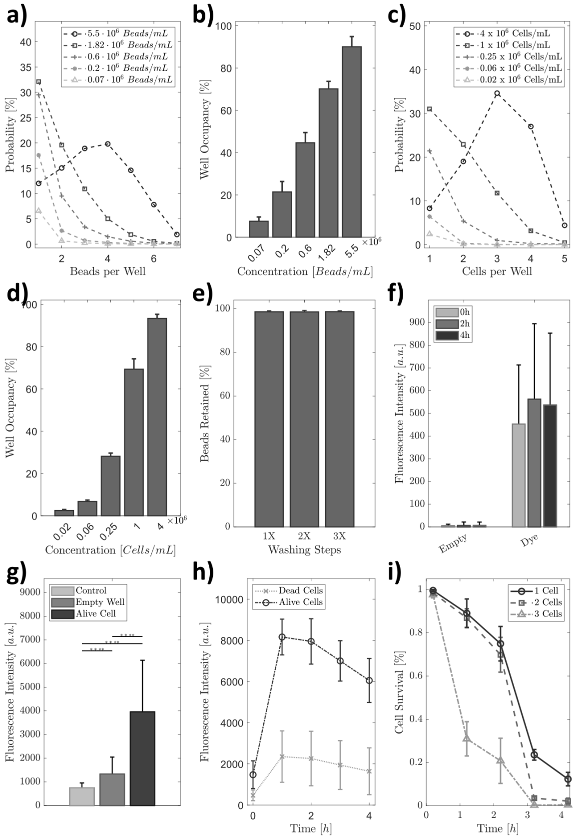

Figure 4.3: Platform characterization. a)-b) The probability of the captured bead number in each well (a) and the probability of occupied wells with at least one bead (b) as a function of the bead concentration. c)-d) The probability of the captured cell number in each well (c) and the probability of occupied wells with at least one cell (d) as a function of the cell concentration. e) The bead retention after several washing steps. f) Calcein AM intensity measured over 4 hours to show well-to-well isolation. Empty wells contain no cell whereas dyed wells contain membrane permeated cells (dead) stained with Calcein AM. g) Fluorescence signal of IL-8 was measured in pure media (Control), wells containing no cells (Empty) and wells containing metabolic active cells (Alive Cell). h) alamar Blue^{TM} intensity shown for alive and dead cells for the duration of 4 hours. g) Cell survival over a period of 4 hours depending on the number of cells in the each well.

cross-contamination between a well and its neighbouring wells. We examined the Calcein AM concentration of wells containing no cell (empty) and wells containing dead cells (dyed) over the duration of 4 hours (Fig. 4.3f). During this time, no leakage from dye containing wells to empty wells could be observed. Additionally, we analysed wells containing highly secreting cells and neighbouring empty wells (Fig. 4.13c). The neighbouring empty wells have a protein readout below the limit of detection (LOD) which implies that the proteins are isolated in each well and show no cross contamination to adjacent wells. However, evaluating all empty wells of an experiments results in a background slightly higher than a control (pure media) condition (Fig. 4.3g). Due to our sensitive system, the immunoassay detects proteins secreted by the cells during washing and cell handling before they are isolation into the microarray wells. To compensate for this, we evaluated the protein concentration by calculating the difference between empty and target wells. The separation of each condition was demonstrated filling each condition with two fluorophores in alternating order (Fig. 4.13b). The fluorophores are contained in the drainage system around the conditions but do not spread to adjacent condition due to the design of the drainage system.

We investigated the viability and the average cell survival on our device for four hours. We observed that cells which are alive (non-permeated membrane) show an increased alamarBlueTM intensity compared to cells which are declared dead (permeated membrane) (Fig. 4.3h). Initially, 99% of cells are alive on chip (Fig. 4.3i). After two hours, 75% of cells in single-occupied wells are still alive and the cell viability drops further drastically. The survival of cells is even lower, when three cells are isolated in the same chamber. We assume that this high mortality rate is due to the limited volume of media inside each well. In standard cell culture, every cell is suspended in average in $\sim 5\ nL$ of medium. In the microwells each cell as only 62 pL, reducing the total amount of nutrients available for the cell. This limits the required nutrition inside the wells which prevents cells from surviving for a long period of time inside the wells. Hence, our small medium is a compromise to reduce volumes and footprint of the device and maximum duration of the experiments. For longer measurements, the volume should be increased to maintain a longer cell viability.

4.2.2 Characterization of the on-bead sandwich immunoassay

The commercial bead assays (ProcartaPlex^{TM}, Thermo Fisher Scientific) were characterized on the platform for the 10 target proteins VEGF, MIP-4, IL-1β, IL-6, IL-8, IP-10, TNF-α, OPN, MCP-1, and MIP-1α (Fig. 4.4). Because we have seven traps per well, not all proteins can be measured from each single cell at the same time. However, every bead combination of 4 and below appeared relative often resulting in statistical correlations between the target proteins. The fluorescence intensity combination of two far-red fluorophores resulted in the barcode which defines every bead type (Fig. 4.4a). The barcode correlates to the primary antibody conjugated on the surface of the bead and the protein concentration was determined by the fluorescence intensity in the yellow spectrum (phycoerythrin, PE). The barcode classification was based on a trained convolutional neural network (CNN) (Fig. 4.4b). The network was trained with thousands of bright field and fluorescence images of beads to be able to assign each bead a barcode and, therefore, the corresponding protein (Fig. 4.4c). For the calibration curve, seven known concentrations of the proteins were measured with the bead assay on the device . The limit of detection (LOD) reaches from 0.289 $ng\ mL^{-1}$ (MIP-4) to 9.58 $ng\ mL^{-1}$ (TNF-α) and strongly depends on the analysed protein. Because of the small volumes of the microwell, the LOD is lower in terms of the concentration compared to the bulk assay; however, in absolute molecule numbers, the LOD of the assay, specifically of MIP-4, IL-1β, and MIP-1α, was below 1450 molecules (Fig. 4.11).

4.2.3 Secretion profile of single macrophages

Next, we analyzed protein secretion of macrophages. We used a cell concentration of approximately 1.5 million cells per millilitre that leads to ca. 60% occupancy of the wells. After distribution of the macrophages on the chip, we incubated the sealed chip for 2 h. Afterwards, the concentrations of the 10 target proteins (VEGF, MIP-4, IL-1β, IL-6, IL-8, IP-10, TNF-α, OPN, MCP-1, MIP-1α) are determined using the protocol described above. The wells contain between 1 to 6 beads of random type so that at least 38′202 or 38% of wells with contain a macrophage and one target protein-capturing bead. Of note is that we used also wells with a macrophage and two beads of the same type, where the signals from the beads were averaged.

The measured fluorescence signal of beads co-incubated with unpolarized macrophages (MΦ) strongly depends on the target protein of the bead (Fig. 4.5a). In some cases cases the measured intensity is above the LOD for the majority of cells; IL-8 (59%), IL-1β (57%), and MIP-1α (59%). In contrast, the relatively high LOD of OPN and the low secretion of VEGF, MIP-4, IL-6, IP-10, TNF-α, and MCP-1 results in a low number of beads exhibiting fluorescence above the LOD. Based on the calibration curves, the fluorescence signals are converted to the secreted

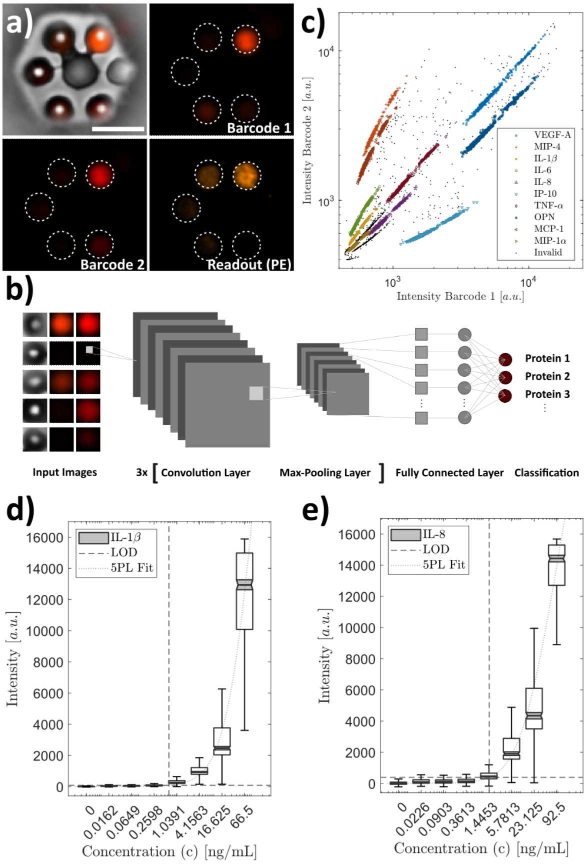

Figure 4.4: Bead assay characterization. a) Images of a single well containing five different bead types. The two fluorophores in the red spectrum are used to determine the barcode of the beads, while the intensity of the yellow fluorophore quantifies the respective protein concentration in the well. Scale bar: 20 μm. b) The barcode and thereby the protein of each bead is determined by a convolutional neural network (CNN) which classifies each bead based on its bright field and fluorophore images. c) Example classification of one experiment based on the CNN. d-e) Example calibration curve of the proteins IL-1β and IL-8. The LOD is calculated by adding three times the standard deviation to the mean of the control.

protein concentrations (Fig. 4.5b). The MΦ macrophages are compared to MΦ macrophages that were stimulated with LPS/INF-γ to differentiate them to the pro-inflammatory phenotype (M1) and to the anti-inflammatory phenotype (M2) that were obtained by treating MΦ macrophages with IL-4/IL-13 (Fig. 4.5b/c). The secretion of the pro-inflammatory cytokine IL-8 is significantly higher for M1 differentiated macrophages (8.6 $ngmL^{-1}$) compared to MΦ macrophages (4.9 $ngmL^{-1}$). Other pro-inflammatory proteins such as MCP-1, MIP-1α, and TNF-α are higher secreted as well but but statistical analysis indicated that the increase in not significant (α = 0.05). The higher secretion of pro-inflammatory proteins agrees with previous observations for macrophages stimulated with LPS and/or INF-γ [20, 33–35]. In contrast, M2 differentiated macrophages exhibit lower secretion of IL-1β, IL-8 and IP-10 compared to the MΦ macrophages. The number of cells secreting over the LOD show the same relative results as the concentration measurements (Fig. 4.5d). Additionally, we calculated the average secreted molecules over two hours for all proteins and stimulation conditions (Fig. 4.5e). The proteins IL-8, TNF-α and OPN belonged to the most secreted proteins across all stimulation conditions with the highest secretion of IL-8 and TNF-α by the LPS/INF-γ treated MΦ macrophages.

MΦ were also treated with two different drugs used in chemotherapy to treat various types of cancer, paclitaxel (PTX, Taxol) and docetaxel (DTX, Taxotere) (Fig. 4.5b/c) [8, 9]. MΦ macrophages treated with DTX showed a significant increase in MIP-1α secretion compared to the MΦ macrophages but no increase of IL-8 or IL-1β secretion, which was observed previously in bulk experiments [8]. A similar but slightly weaker increase of MIP-1α secretion can be seen by MΦ macrophages treated with PTX (Fig. 4.5c/d). A similar increase in in MIP-1α was measured by Wanderley et al. after two doses of PTX over 48 hours [9]. The MIP-1α is an inflammatory chemokine regulating the immune cell trafficking around the TME and is associated with a pro-tumoural function in the TME [36–38]. Based on our findings, the investigation of a combinatorial drug treatment that is reducing the secreted MIP-1α concentration during paclitaxel or docetaxel drug treatment with a MIP-1α antagonist is of great interest.

4.2.4 Multiplexed analysis of secreted cytokines

The multiplexed analysis of single cells exposes the correlation between different proteins. Since we have approximately 14% of wells where two beads of different type are co-encapsulated, we can reveal if the proteins are co-secreted (+/+), only one protein is secreted above the LOD (+/-, -/+), or both proteins are secreted be-

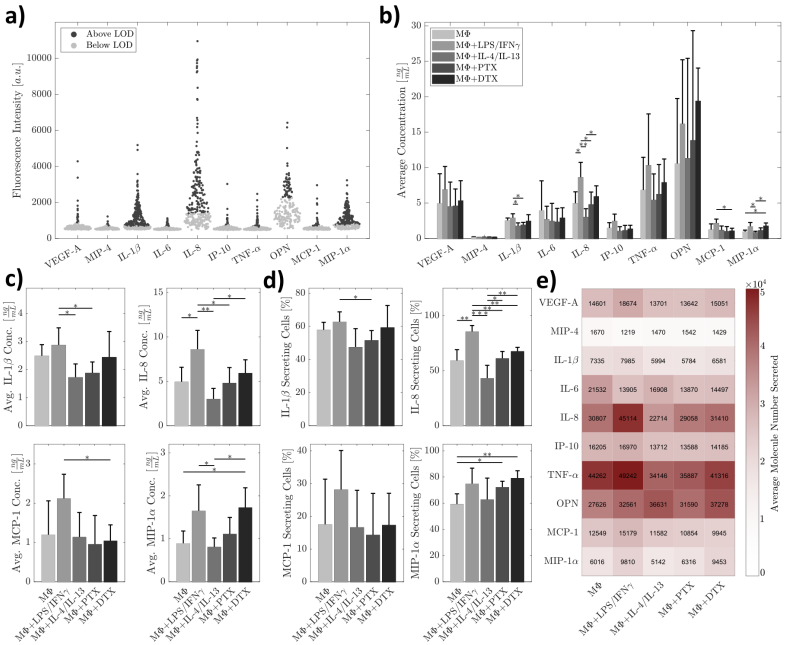

	MΦ	MΦ+LPS/IFNγ	MΦ+IL-4/IL-13	MΦ+PTX	MΦ+DTX
VEGF-A	14601	18674	13701	13642	15051
MIP-4	1670	1219	1470	1542	1429
IL-1β	7335	7985	5994	5784	6581
IL-6	21532	13905	16908	13870	14497
IL-8	30807	45114	22714	29058	31410
IP-10	16205	16970	13712	13588	14185
TNF-α	44262	49242	34146	35887	41316
OPN	27626	32561	36631	31590	37278
MCP-1	12549	15179	11582	10854	9945
MIP-1α	6016	9810	5142	6316	9453

Figure 4.5: Protein secretion from single cells. a) The readout fluorescence intensities measured for the ten target proteins secreted by MΦ macrophages. Every datapoint represent the readout of one single cell. (N = 1, n = 1, ntotal = 2’520) b) MΦ macrophages are stimulated off-chip for one hour with different stimuli. The average protein concentration secreted by single cells over two hours was evaluated for all target proteins. (N = 3, n = 4, ntotal = 41’753) c) The average secreted protein concentration depicted for selected proteins. d) The percentage of cell secreting over the LOD shown for selected proteins and different stimulation conditions. e) The average secreted molecule number for each protein and condition averaged over all single cell of all measurements ($n \geq 401$). N = number of experiments, n = number of conditions, ntotal = number of cells.

low the LODs (Fig. 4.6a). The percentage of co-secreting MIP-1α and IL-8 single cells drastically changes based on the stimulation of the macrophages (Fig. 4.6b). LPS/INF-γ stimulation results in a high co-secretion (76.9%) whereas the stimulation with IL-4/IL-13 leads to half the co-secretion (31.6%). Interestingly, the ratio of only MIP-1α secreting cells compared to only IL-8 secreting cells changes drastically from around 1:1 in case of MΦ and MΦ+LPS/INF-γ to 14:1 in the case of IL-4/IL-13 stimulation. This implies that the relative percentage of secreting MIP-1α cells increases while the percentage of IL-8 secreting cells decreases. In contrast, in the case of IL-1β and IL-8 the stimulation with LPS/INF-γ results in a 1:11 ratio between IL-1β to IL-8 secreting cells. Even though this classification depends on the

LOD of our device, it is a qualitative method to compare the change of percentage in each region depending on the stimulation of the macrophages.

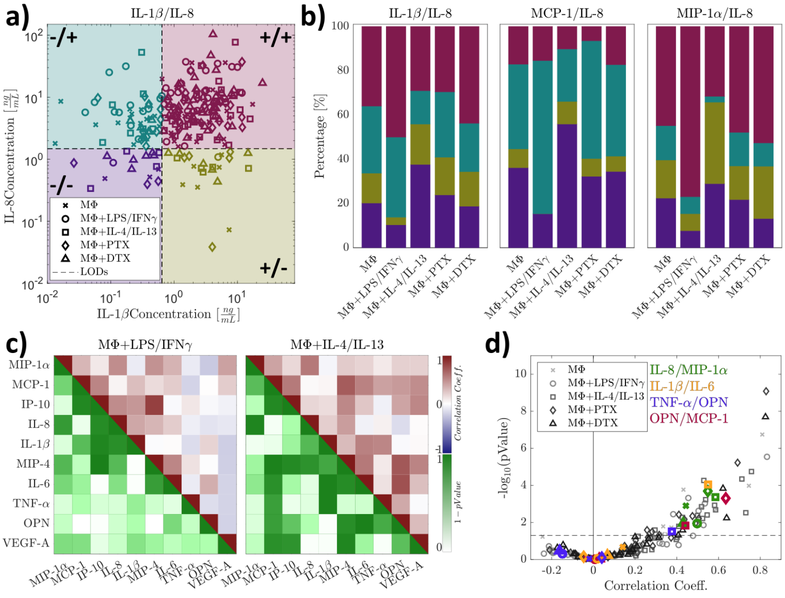

Figure 4.6: Pairwise correlation analysis. a) IL-1β secretion plotted versus IL-8 concentration of single cells. Each cell is classified by its secretion level: secreting both proteins (top right), secreting only one (top left, bottom right), or none (bottom left). (n = 386) b) The percentage of cells in each classification region shown for different stimulations and selected protein pairs. c) The pair wise correlation matrix and their significance for MΦ+LPS/INF-γ and MΦ+IL-4/IL-13 macrophages are shown for all measured proteins. d) Volcano plot of the correlation coefficient between the proteins. The significance level of 0.05 is shown by the dashed line.

The pair-wise correlation coefficient matrix reveals the secretion relationship between all proteins for each stimulation condition (Fig. 4.6c). Specifically, the correlations of TNF-α, VEGF, and OPN with most other proteins changes with the stimulation of the macrophages. Noteworthy is the change from the mainly negative correlation when stimulated with LPS/INF-γ to the positive dominating correlations when stimulated with IL-4/IL-13 indicating the co-secretion of these proteins. The stimulation with IL-4/IL-13 corresponds to M2-like macrophages which are known for their pro-tumoural function in the TME [4]. A high level of VEGF, OPN and/or TNF-α in the TME is associated with poor tumour progression [39–41]. To visualize the different correlations and their significance, we created a volcano plot highlighting the significant protein pairs (Fig. 4.6d). The pro-inflammatory protein pair, IL-8/MIP-1α, is positively correlated independent of the stimulation condition. However, we found a significant positive correlation between IL-1β and IL-6 by macrophages treated with IL-4/IL-13 (0.55) compared to no correlation (0.018) by macrophages treated with LPS/INF-γ. It was shown that IL-6 is a pro-tumorigenic agent and is induced by IL-1β [42]. By blocking the IL-1/IL-6 pathway, the overall patient survival of multiple myeloma patient could be increased [42]. The same correlation change can be seen in the pro-tumoural protein pairs TNF-α/OPN and OPN/MCP-1. Interestingly, the treatment with paclitaxel results in an even higher correlation between OPN/MCP-1 compared to the IL-4/IL-13 treated macrophages. This suggests that OPN/MCP-1 is a potential drug target for a combinatorial treatment with taxanes.

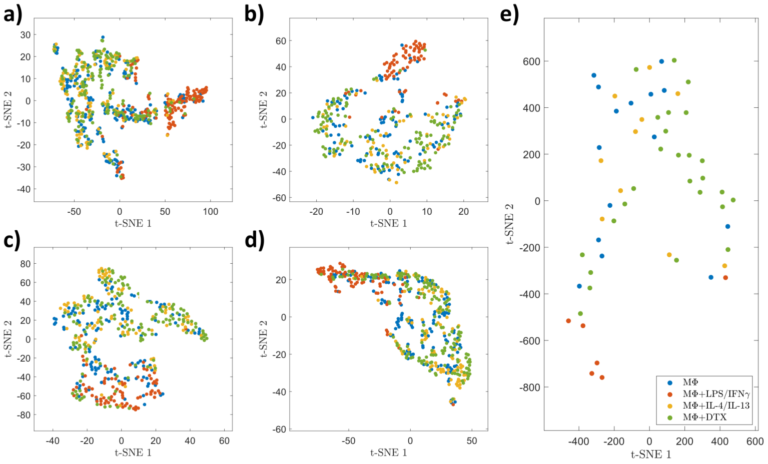

Figure 4.7: Multiplexed protein secretion from single cells. a-d) The t-SNE algorithm was used to generate a 2d representation based on the secretion of IL-1β, IL-8 and TNF-α (a, n = 555), IL-1β, IL-8 and MIP-1α (b, n = 360), IL-1β, TNF-α, and MIP-1a (c, n = 442), and IL-8, TNF-α, and MIP-1α (d, n = 445). Each data point originates from an individual cell and the colour indicates the stimulation condition. e) T-SNE representation of all four proteins (IL-1β, IL-8, TNF-α, and MIP-1α).

We investigated the multiplexed secretion of IL-1β, IL-8, TNF-α, and MIP-1α in more detail by reducing the number of different bead types to four and, therefore, increasing the probability of having wells with one cell and three or even all four target proteins. The secreted proteins are projected onto a two-dimensional map using the t-distribution stochastic neighbour embedding (t-SNE) algorithm (Fig. 4.7).

The pro-inflammatory macrophages (red) cluster shows a distinctive cluster compared to the other stimulation conditions; specifically, to the anti-inflammatory (yellow) and docetaxel treated (green) macrophages. This clustering is visible for all combinations of proteins and indicates that the pro-inflammatory macrophages have a more distinct phenotype with respect to the selected proteins. In contrast, no clear clustering of the native (blue), anti-inflammatory (yellow), and docetaxel treated (green) macrophages can be seen.

Despite the reduction of the target proteins, the number of wells with one cell and all four beads was low (n=57 wells in total). Nevertheless, the same visualization indicates again a cluster of pro-inflammatory cells, while the otherwise treated macrophages and the native macrophages are scattered (Fig. 4.7e).

Our results demonstrate that the developed wells-in-well microarray is a highly parallelized, versatile, and easy-to-use microfluidic device with the capability to investigate a large population of single cells. We showed that the device can detect low numbers of proteins in each well based on an on-bead sandwich immunoassay. The developed device enabled the study of macrophage polarization based on 10 secreted proteins and in depth analysis of the impact of anti-cancer drugs on the secretion pattern of them.

4.3 Conclusion

We developed a versatile wells-in-well microarray to quantitatively measure secreted cytokines from single macrophages. Functionalized magnetic beads are co-captured with individual cells in more than 10^5 microwells. The multiplexed, barcoded, and commercially available beads detect the secreted proteins from the co-captured macrophages. The magnetic beads are retained in each well by magnetic forces, allowing thorough washing, resulting in a highly sensitive immune sandwich assay with LODs below 1200 molecules per well. A convolutional neural network was trained to classify each bead to the corresponding protein. With the microwell array, we successfully characterized and measured 10 different proteins from thousands of macrophages. We showed the effect of different stimulations on the secretion of single macrophages including the effect of cancer drugs on the cells. The most abundant secretion by the macrophages was measured by the cytokines IL-1β, IL-8, and MIP-1α and the stimulation with LPS/INF-γ resulted in a 76% increase in the IL-8 secretion. Additionally, we demonstrated that the treatment of macrophages with the taxanes, paclitaxel and docetaxel, resulted in an increase of MIP-1α secretion. Moreover, we studied the pairwise correlation between 45 protein pairs, identifying significant protein correlations. Specifically, our results indicate the importance of the co-secretion of IL-1β/IL-6 which is a target in a current phase II study and of OPN/MCP-1 as a potential drug target for combinatorial treatment with taxanes. We also analysed combinations of three and four proteins. To increase the probability to co-capture three or four different bead types plus one macrophage in one well, we reduced the initial bead mixture to four types (instead of ten). We found that pro-inflammatory macrophages are more distinct in their protein secretion profile than the other investigated macrophages with respect to the investigated proteins IL-1β, IL-8, TNF-α, and MIP-1α. In summary, our results underline the versatility of our method for obtaining large single-cell data sets, and we believe that it can be alike employed for other cell types and other cytokines.

4.4 Materials and methods

4.4.1 Wafer fabrication

The microwell device was fabricated by the standard soft lithography process (Fig. 4.8). The master mould was produced by exposing two layers of SU-8 with different mask designs. The masks for the different layers were designed in AutoCAD (Autodesk) and were fabricated and purchased from Selba S.A. The first layer contains the pattern for the hexagonal cell traps (height: $\sim$45 μm) and the second layer contains the drainage system and magnetic traps with a diameter of 8.5 μm (height: $\sim$9 μm). For the first layer, SU-8 3050 is spin coated (2500 rpm) on a dehydrated silicon wafer. After 10 min of pre-exposure bake at 95 $^\circ C$, the SU-8 layer is exposed with 175 $mJ\ cm^{-2}$ in a mask aligner followed by a post-exposure bake of 3 min at 95 $^\circ C$. The second layer (SU-8 3005) is directly spin coated on top of the first layer with a spin coating speed of 5000 rpm. The pre-exposure bake was reduced to 5 min followed by an exposure of the second layer with 450 $mJ\ cm^{-2}$. The post exposure bake stayed the same. Finally, the device was developed in mr-DEV600 for 15 min and post baked for 2 h at 160 $^\circ C$. The final master mould wafer was silanized by perfluorooctyl trichlorosilane (PFOTS).

4.4.2 Device fabrication and preparation

The thermoplastic device was fabricated by a hot embossing method developed by Kling et al [43]. The COC2008 foil with a thickness of 240 μm is placed above the SU-8 master mould in a compact nanoimprint (CNI) tool (NIL Technology) (Fig. 4.9). To prevent breaking of the master mould, a silanized silicon wafer and a 1 mm

thick aluminium plate is placed on top of the COC to homogenously distribute the applied pressure by the CNI tool on the master mould. Two Teflon sheets prevent adhesion of the master mould and the aluminium plate to the CNI tool. The hot embossing was conducted with 6 *bar* at 145 °*C* for 5 *min*. The final devices were cut out and sealed with a scotch tape to reduce contamination and for further use in the experiments.

Directly before the experiment was conducted and to reduce protein adhesion to the COC, the conditions were coated with anti-adherence rinsing solution (STEMCELL). This was achieved by pipetting 25 μL of the solution on each condition, placing the device in vacuum for 1 *min* to fill all wells and incubating the device for 30 *min*.

4.4.3 Magnet holder fabrication

The magnetic field was simulated in COMSOL Multiphysics (Comsol, Inc.) to achieve a homogenous force on the magnetic beads in the microwells. After the optimal placement of the magnets was simulated, the holder was designed in SOLIDWORKS 2018 (Dassault Systèmes, Fig. 4.10), and 3d printed with black poly carbonate (Ultimaker 3). With the help of a plier, 45 quadratic neodym magnets (3×4×8 *mm*, Webcraft AG) were inserted in the mount.

4.4.4 Cell culture

The THP-1 cell line was cultured in the Roswell Park Memorial Institute (RPMI) media supplemented with 10% foetal bovine serum (FBS), 1xGLutaMAX and 1000 $U\ mL^{-1}$ penicillin and streptomycin. To initiate the macrophage differentiation, THP-1 cells were cultivated for 24 *h* in 100 $ng\ mL^{-1}$ phorbol 12-myristate 13-acerate (PMA). After 24 *h*, the cells were stimulated with either LPS (1 $\mu g\ mL^{-1}$) and INF-γ (50 $ng\ mL^{-1}$), IL-4 (50 $ng\ mL^{-1}$) and IL-13 (50 $ng\ mL^{-1}$), paclitaxel (Taxol), or docetaxel (Taxotere) for 1 *h*.

The cells were detached by washing them in phosphate-buffered saline (PBS) before incubating them for 15 *min* in tripLE^{TM}. After successful detachment, they were stained with CellTrace^{TM} Calein AM for 15 *min*. Before introducing the cells on the device, 3 washing steps in PBS were conducted.

4.4.5 Experimental procedure

All different ProcartaPlex^{TM} magnetic beads (Thermo Fisher Scientific) were diluted to achieve a final concentration of 5× (50× stock concentration). The beads were washed two time before used on chip. On each condition, 20 μL of the bead suspension was pipetted and carefully distributed by up and down pipetting of 10 μL multiple times. The assay washing buffer (1×) was used to wash the beads and remove all not-trapped magnetic beads from the device. The device was washed three times with the cell culture media (DMEM, Gibco) to remove all residues of the washing buffer. Afterwards, 20 μL of the cells were pipetted directly on each condition. After 2 *min* settling time on a shaker, the device is immersed in HFE-7500 Engineered fluid. The residue media is removed from beneath the oil. The device is turned around and placed on a fully automated microscope. During the 2 *h* incubation time, the cells were in an environmental chamber which provided an atmosphere of 5% CO_2, a humidity of at least 80% and a temperature of 37 $^\circ C$. Microscopy images of each condition was taken. After the device is taken out of the HFE-7500 container, all liquid absorbed by a filter paper (Whatman^{TM}, Sigma Aldrich) to prevent cross-contamination between wells. The device is put in 500 *mL* of DI water and placed in vacuum for 1 *min* to refill all wells. After rigorous washing with washing buffer (1×), 20 μL of the secondary antibodies at a concentration of 1× were pipetted on the conditions and incubated for 30 *min* on a shaker at 150 *rpm*. This was repeated for the streptavidin-PE conjugate to stain the beads. Finally, the reading buffer (1×) of the assay was pipetted on the device and a microscopy slide placed on the device for the imaging of the barcoded beads.

4.4.6 Bead assay characterization

The protein dilution series for the calibration curves was prepared according to the ProcartaPlex^{TM} protocol with the provided proteins in DMEM media at 0.1×. The beads were loaded on the device according to the experimental procedure protocol. The beads were washed three times with DMEM media before all liquid was removed with a filter paper. On each condition, 20 μL of the protein dilution series was pipetted. The device was vacuumed for 1 *min* to guarantee a homogenous filling of the microwells. After 2 *h* of incubation at 37 $^\circ C$ and 5% CO_2 the assay and readout of the beads was conducted according to the experimental procedure protocol. For the standard calibration curves, the 5PL fit was used to calculate the protein concentration as a function of the fluorescence intensity. The limit of detection (LOD) was established by adding three times the standard deviation to the mean of the control.

4.4.7 Cellular metabolism and survival experiment

The cellular metabolism and survival experiment was conducted with THP-1 cells. The cells were stained with Calcein AM and the media contained 10% of alamarBlue^{TM} to show the metabolic activity of the cells. Dead cells were identified by the Calcein AM leaking from the cytosol into the chamber decreasing the ration between the intra-cellular Calcein AM concentration and the outside.

4.4.8 Optical setup

All images were taken with a fully automated Eclipse Ti2 (Nikon) microscope with a SOLA II (Lumencore) as a fluorescence excitation light engine. A DS-Qi2 camera (Nikon) and a 20X objective (Plan Apo VC 20X, NA:0.75, Nikon) was used for the acquisition of the images. The standard DAPI, GFP, mCherry fluorescence cubes were used for fluorescence imaging. For the readout of the beads, three custom cubes were used: one for the assay readout of Phycoerythrin (PE: EX 530/40, DM 565, EM 611/75), and two for the barcode in the far-red spectrum (B1: EX 628/32, DM 649, EM 670/30; B2: EX 640/30, DM 649, EM 711/25). The light intensity and exposure time was fixed over all experiments and was set to 2%, 20%, 50%, 50%, 50%, 50% and 100 ms, 50 ms, 500 ms, 500 ms, 100 ms, 200 ms for DAPI, GFP, mCherry, PE, B1, B2, respectively.

4.4.9 Data evaluation

The images were evaluated with a custom MATLAB script with a graphical user interface. Briefly, the locations of the microwells were determined on each image. In every well, the cells and the barcoded beads were detected and the mean fluorescence intensity over the diameter of the beads in three channels (PE, B1, B2) was evaluated. The mean fluorescence data of each bead was used for further data analysis. The fluorescence data of each bead was converted to the protein concentration based on the standard calibration curve evaluated for each protein. Beads below the background fluorescent intensity were assigned a concentration of 0 $ng\ mL^{-1}$.

For Fig. 4.5 b) to d), the average concentration was calculated by averaging the mean secreted protein concentration over one condition over all device replicates. All beads, above and below the LOD, were considered. For the multiplexed data set in Fig. 4.6, only beads with protein concentrations bigger than 0 $ng\ mL^{-1}$ were considered.

4.4.10 Convolutional neural network

The convolutional neural network was created with the Deep Learning Toolbox^{TM} from MATLAB. The network consists of three convolutional layers (3×3 kernel) followed by a batch normalization and ReLU layer. The number of filters used per layer was 8, 12, and 32. The stride length was fixed to 1 pixel. Between the convolution layer, a maximal pooling with a factor of two was performed. The validation accuracy was 97.8% with a data set of more than 10'000 beads.

4.4.11 Statistical analysis

All statistical evaluations were performed with MATLAB. The significant difference between distributions was evaluated with the two-sided student t-test. If no indicator above a plot is shown, the two data sets are not significant different (ns). **** $p < 0.0001$, *** $p < 0.001$, ** $p < 0.01$, * $p < 0.05$.

4.5 Acknowledgments

We thank Dr. Darius Rackus (ETH Zurich, Switzerland) for proofreading. Financial support by the Swiss National Science Foundation (NCCR Molecular Systems Engineering) and the ERANet-RUS Program (Project TARQUS) is gratefully acknowledged.

4.6 Supplementary information

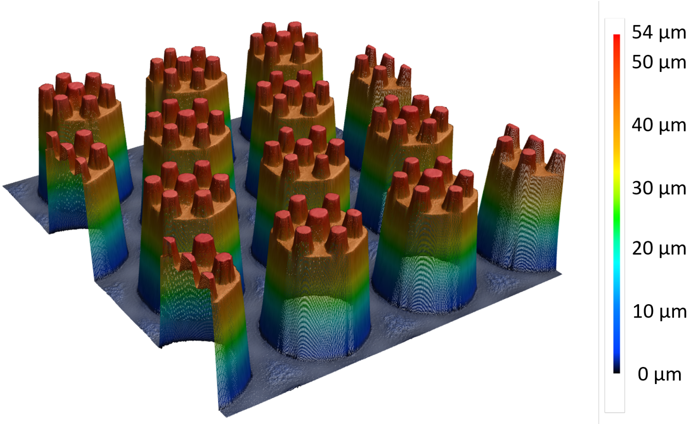

Figure 4.8: Microscopic image of the master mould wafer with its SU8 structures. The image was taken with a 3d laser scanning microscope (Keyence VK-X3000). The height of the hexagonal wells is ∼44 *µm* and the height of the magnetic bead traps is ∼9 *µm*.

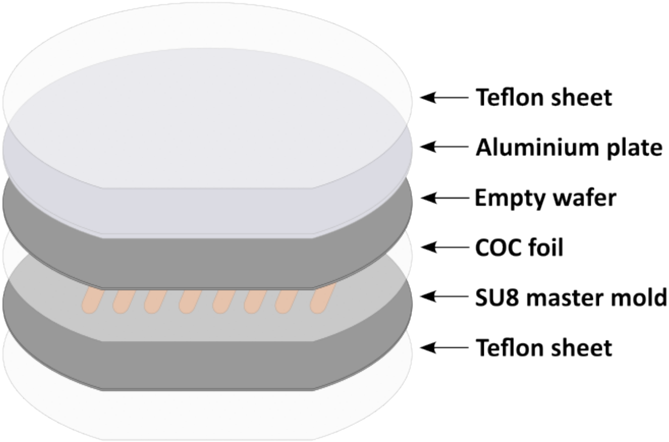

Figure 4.9: Fabrication process of the COC device. Two Teflon sheets prevent sticking of the master mould and the aluminium plate to the CNI tool. The COC foil is heated between the master mould and an empty, silanized wafer. The aluminium plate prevents the silicon wafers from breaking.

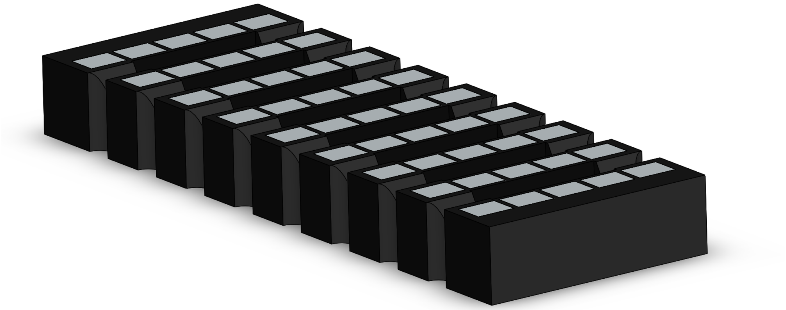

Figure 4.10: CAD model (Solidworks 2021) of the magnet holder. Five magnets are placed on each side of the eight conditions (45 in total). Due to the placement of the magnets, the microwell array is located in a strong magnetic field pulling the magnetic beads downwards without blocking the view for brightfield imaging.

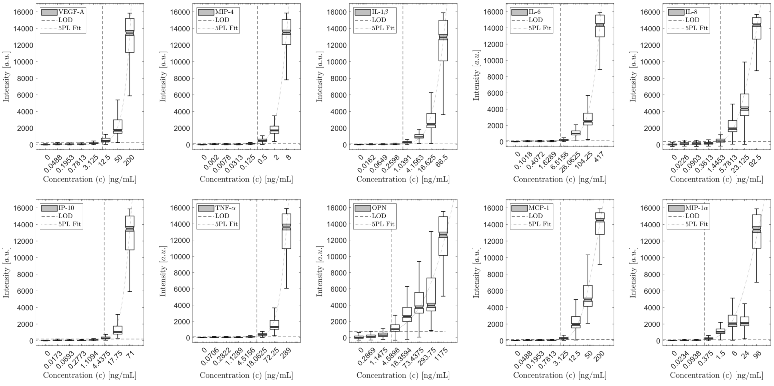

Protein	VEGF-A	MIP-4	IL-1β	IL-6	IL-8	IP-10	TNF-α	OPN	MCP-1	MIP-1α
LOD Concentration (ng/mL)	8.51	0.289	0.643	4.37	1.48	3.73	9.58	3.18	2.06	0.232
LOD Number of Molecules	8490	1412	1416	7945	6705	16508	20989	3591	9130	1136

Figure 4.11: Calibration curves for all proteins analysed. The limit of detection (LOD) is calculated by adding 3 time the standard deviation to the median value of the control (0 $ng\ mL^{-1}$). The 5PL Fit was fitted with MATLAB. For the fit, the concentrations around the LOD were more heavily weighted to increase the precision of the fit around the LOD. A volume of 63.29 picolitre was used to calculate the number of molecules in each well at the LOD.

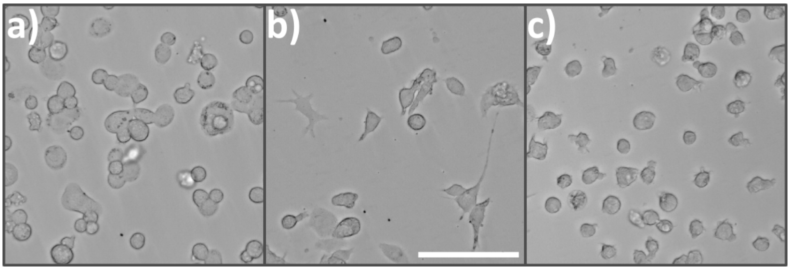

Figure 4.12: Microscopic images of differently stimulated macrophages. a) THP-1 cells were incubated in 100 $ng\ mL^{-1}$ PMA for 24h (MΦ). b) After incubation with PMA for 24h, LPS (1 μg/mL) and IFN-γ (50 $ng\ mL^{-1}$) was added for 12 h (MΦ+LPS/IFN-γ). c) IL-4 (50 $ng\ mL^{-1}$) and IL-13 (50 $ng\ mL^{-1}$) was added after 24h for 12 h (MΦ+IL-4/IL-13). Scalebar: 100um

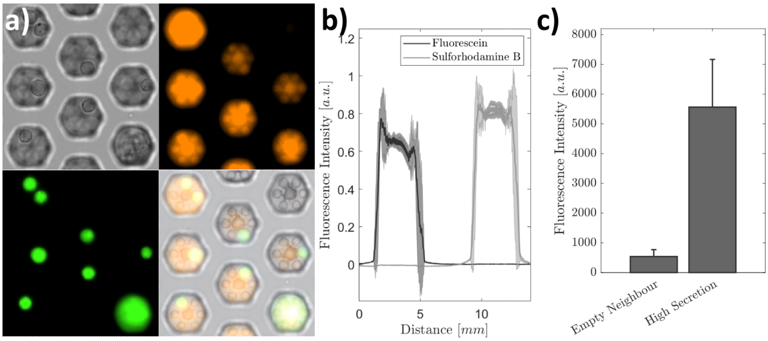

Figure 4.13: Additional characterization. a) Example image of cells in media containing 15 alamarBlueTM stained with Calcein AM. An empty well can be seen in the top right corner. In the lower left corner, the Calcein AM leaked out of the cell indicating a dead cell. b) Each condition is filled either with fluorescein or sulforhodamine B in alternating order. Depicted is the normalized mean intensity of 4 pairs of neighbouring conditions so demonstrate the spatial separation between conditions. c) Selected are the 2% highest secreting cells for IL-8 and their empty neighbours wells. The readout in the empty wells is below the detection limit showing no cross-contamination from one well to the other.

4.7 References

[1] M. Locati, G. Curtale, and A. Mantovani, «Diversity, mechanisms, and significance of macrophage plasticity», Annual Review of Pathology: Mechanisms of Disease **15**, 123–147 (2020).

[2] L. Cassetta and J. W. Pollard, «A timeline of tumour-associated macrophage biology», Nature Reviews Cancer **23**, 238–257 (2023).

[3] P. J. Murray, «Macrophage polarization», Annual Review of Physiology **79**, 541–566 (2017).

[4] A. Mantovani, P. Allavena, F. Marchesi, and C. Garlanda, «Macrophages as tools and targets in cancer therapy», Nature Reviews Drug Discovery **21**, 799–820 (2022).

[5] A. Shapouri-Moghaddam, S. Mohammadian, H. Vazini, M. Taghadosi, S. A. Esmaeili, F. Mardani, B. Seifi, A. Mohammadi, J. T. Afshari, and A. Sahebkar, «Macrophage plasticity, polarization, and function in health and disease», Journal of Cellular Physiology **233**, 6425–6440 (2018).

[6] M. D. Palma, D. Biziato, and T. V. Petrova, «Microenvironmental regulation of tumour angiogenesis», Nature Reviews Cancer **17**, 457–474 (2017).

[7] A. Marrocco and L. A. Ortiz, «Role of metabolic reprogramming in pro-inflammatory cytokine secretion from lps or silica-activated macrophages», Frontiers in Immunology **13**, 936167 (2022).

[8] C. R. Millrud, M. Mehmeti, and K. Leandersson, «Docetaxel promotes the generation of anti-tumorigenic human macrophages», Experimental Cell Research **362**, 525–531 (2018).

[9] C. W. Wanderley, D. F. Colón, J. P. M. Luiz, F. F. Oliveira, P. R. Viacava, C. A. Leite, J. A. Pereira, C. M. Silva, C. R. Silva, R. L. Silva, C. A. Speck-Hernandez, J. M. Mota, J. C. Alves-Filho, R. C. Lima-Junior, T. M. Cunha, and F. Q. Cunha, «Paclitaxel reduces tumor growth by reprogramming tumor-associated macrophages to an m1 profile in a tlr4-dependent manner», Cancer Research **78**, 5891–5900 (2018).

[10] F. C. Jammes and S. J. Maerkl, «How single-cell immunology is benefiting from microfluidic technologies», Microsystems and Nanoengineering **6**, 45 (2020).

[11] S. T. Gebreyesus, G. Muneer, C.-C. Huang, A. A. Siyal, M. Anand, Y.-J. Chen, and H.-L. Tu, «Recent advances in microfluidics for single-cell functional proteomics», Lab on a Chip **23**, 1726–1751 (2023).

[12] T. Konry, M. Dominguez-Villar, C. Baecher-Allan, D. A. Hafler, and M. Yarmush, «Droplet-based microfluidic platforms for single t cell secretion analysis of il-10 cytokine», Biosensors and Bioelectronics **26**, 2707–2710 (2011).

[13] V. Chokkalingam, J. Tel, F. Wimmers, X. Liu, S. Semenov, J. Thiele, C. G. Figdor, and W. T. S. Huck, «Probing cellular heterogeneity in cytokine-secreting immune cells using droplet-based microfluidics», Lab on a Chip **13**, 4740 (2013).

[14] L. Mazutis, J. Gilbert, W. L. Ung, D. A. Weitz, A. D. Griffiths, and J. A. Heyman, «Single-cell analysis and sorting using droplet-based microfluidics», Nature Protocols **8**, 870–891 (2013).

[15] K. Eyer, R. C. L. Doineau, C. E. Castrillon, L. Briseño-Roa, V. Menrath, G. Mottet, P. England, A. Godina, E. Brient-Litzler, C. Nizak, A. Jensen, A. D. Griffiths, J. Bibette, P. Bruhns, and J. Baudry, «Single-cell deep phenotyping of igg-secreting cells for high-resolution immune monitoring», Nature Biotechnology **35**, 977–982 (2017).

[16] M. N. Hsu, S.-C. Wei, S. Guo, D.-T. Phan, Y. Zhang, and C.-H. Chen, «Smart hydrogel microfluidics for single-cell multiplexed secretomic analysis with high sensitivity», Small **14**, 1802918 (2018).

[17] Y. Bounab, K. Eyer, S. Dixneuf, M. Rybczynska, C. Chauvel, M. Mistretta, T. Tran, N. Aymerich, G. Chenon, J. F. Llitjos, F. Venet, G. Monneret, I. A. Gillespie, P. Cortez, V. Moucadel, A. Pachot, A. Troesch, P. Leissner, J. Textoris, J. Bibette, C. Guyard, J. Baudry, A. D. Griffiths, and C. Védrine, «Dynamic single-cell phenotyping of immune cells using the microfluidic platform dropmap», Nature Protocols **15**, 2920–2955 (2020).

[18] K. Portmann, A. Linder, N. Oelgarth, and K. Eyer, «Single-cell deep phenotyping of cytokine release unmasks stimulation-specific biological signatures and distinct secretion dynamics», Cell Reports Methods **3**, 100502 (2023).

[19] C. Ma, R. Fan, H. Ahmad, Q. Shi, B. Comin-Anduix, T. Chodon, R. C. Koya, C.-C. Liu, G. A. Kwong, C. G. Radu, A. Ribas, and J. R. Heath, «A clinical microchip for evaluation of single immune cells reveals high functional heterogeneity in phenotypically similar t cells», Nature Medicine **17**, 738–743 (2011).

[20] Y. Lu, Q. Xue, M. R. Eisele, E. S. Sulistijo, K. Brower, L. Han, E. A. D. Amir, D. Pe'er, K. Miller-Jensen, and R. Fan, «Highly multiplexed profiling of single-cell effector functions reveals deep functional heterogeneity in response to pathogenic ligands», Proceedings of the National Academy of Sciences of the United States of America **112**, E607–E615 (2015).

[21] L. Armbrecht, R. S. Müller, J. Nikoloff, and P. S. Dittrich, «Single-cell protein profiling in microchambers with barcoded beads», Microsystems and Nanoengineering **5**, 55 (2019).

[22] L. Armbrecht, O. Rutschmann, B. M. Szczerba, J. Nikoloff, N. Aceto, and P. S. Dittrich, «Quantification of protein secretion from circulating tumor cells in microfluidic chambers», Advanced Science **7**, 1903237 (2020).

[23] C. L. Dietsche, E. Hirth, and P. S. Dittrich, «Multiplexed analysis of signalling proteins at the single-immune cell level», Lab on a Chip **23**, 362–371 (2022).

[24] J. C. Love, J. L. Ronan, G. M. Grotenbreg, A. G. van der Veen, and H. L. Ploegh, «A microengraving method for rapid selection of single cells producing antigen-specific antibodies», Nature Biotechnology **24**, 703–707 (2006).

[25] A. J. Torres, A. S. Hill, and J. C. Love, «Nanowell-based immunoassays for measuring single-cell secretion: characterization of transport and surface binding», Analytical Chemistry **86**, 11562–11569 (2014).

[26] X. An, V. G. Sendra, I. Liadi, B. Ramesh, G. Romain, C. Haymaker, M. Martinez-Paniagua, Y. Lu, L. G. Radvanyi, B. Roysam, and N. Varadarajan, «Single-cell profiling of dynamic cytokine secretion and the phenotype of immune cells», PLOS ONE **12**, e0181904 (2017).

[27] J. R. Choi, J. H. Lee, A. Xu, K. Matthews, S. Xie, S. P. Duffy, and H. Ma, «Monolithic hydrogel nanowells-in-microwells enabling simultaneous single cell secretion and phenotype analysis», Lab on a Chip **20**, 4539–4551 (2020).

[28] Y. Zhou, N. Shao, R. B. de Castro, P. Zhang, Y. Ma, X. Liu, F. Huang, R.-F. Wang, and L. Qin, «Evaluation of single-cell cytokine secretion and cell-cell interactions with a hierarchical loading microwell chip», Cell Reports **31**, 107574 (2020).

[29] M. Elitas, K. Brower, Y. Lu, J. J. Chen, and R. Fan, «A microchip platform for interrogating tumor-macrophage paracrine signaling at the single-cell level», Lab on a Chip **14**, 3582–3588 (2014).

[30] N. Kravchenko-Balasha, Y. S. Shin, A. Sutherland, R. D. Levine, and J. R. Heath, «Intercellular signaling through secreted proteins induces free-energy gradient-directed cell movement», Proceedings of the National Academy of Sciences **113**, 5520–5525 (2016).

[31] S. Lee, J. de Rutte, R. Dimatteo, D. Koo, and D. D. Carlo, «Scalable fabrication and use of 3d structured microparticles spatially functionalized with biomolecules», ACS Nano **16**, 38–49 (2022).

[32] J. de Rutte, R. Dimatteo, M. M. Archang, M. van Zee, D. Koo, S. Lee, A. C. Sharrow, P. J. Krohl, M. Mellody, S. Zhu, J. V. Eichenbaum, M. Kizerwetter, S. Udani, K. Ha, R. C. Willson, A. L. Bertozzi, J. B. Spangler, R. Damoiseaux, and D. D. Carlo, «Suspendable hydrogel nanovials for massively parallel single-cell functional analysis and sorting», ACS Nano **16**, 7242–7257 (2022).

[33] D. M. Mosser and J. P. Edwards, «Exploring the full spectrum of macrophage activation», Nature Reviews Immunology **8**, 958–969 (2008).

[34] Q. Xue, Y. Lu, M. R. Eisele, E. S. Sulistijo, N. Khan, R. Fan, and K. Miller-Jensen, «Analysis of single-cell cytokine secretion reveals a role for paracrine signaling in coordinating macrophage responses to tlr4 stimulation», Science Signaling **8**, ra59 (2015).

[35] E. Müller, P. F. Christopoulos, S. Halder, A. Lunde, K. Beraki, M. Speth, I. Øynebråten, and A. Corthay, «Toll-like receptor ligands and interferon-y synergize for induction of antitumor m1 macrophages», Frontiers in Immunology **8**, 1383 (2017).

[36] D. Argyle and T. Kitamura, «Targeting macrophage-recruiting chemokines as a novel therapeutic strategy to prevent the progression of solid tumors», Frontiers in Immunology **9**, 2629 (2018).

[37] T. Kodama, Y.-i. Koma, N. Arai, A. Kido, N. Urakawa, M. Nishio, M. Shigeoka, and H. Yokozaki, «Ccl3-ccr5 axis contributes to progression of esophageal squamous cell carcinoma by promoting cell migration and invasion via akt and erk pathways», Laboratory Investigation **100**, 1140–1157 (2020).

[38] S. K. Y. To, M. K. S. Tang, Y. Tong, J. Zhang, K. K. L. Chan, P. P. C. Ip, J. Shi, and A. S. T. Wong, «A selective beta-catenin-metadherin/ceacam1-ccl3 axis mediates metastatic heterogeneity upon tumor-macrophage interaction», Advanced Science **9**, e2103230 (2022).

[39] D. Ribatti, B. Nico, E. Crivellato, and A. Vacca, «Macrophages and tumor angiogenesis», Leukemia **21**, 2085–2089 (2007).

[40] S. A. Lund, C. M. Giachelli, and M. Scatena, «The role of osteopontin in inflammatory processes», Journal of Cell Communication and Signaling **3**, 311–322 (2009).

[41] Y. Wu and B. P. Zhou, «Tnf-a/nf-kb/snail pathway in cancer cell migration and invasion», British Journal of Cancer **102**, 639–644 (2010).

[42] J. A. Lust, M. Q. Lacy, S. R. Zeldenrust, T. E. Witzig, L. L. Moon-Tasson, C. A. Dinarello, and K. A. Donovan, «Reduction in c-reactive protein indicates successful targeting of the il-1/il-6 axis resulting in improved survival in early stage multiple myeloma», American Journal of Hematology **91**, 571–574 (2016).

[43] A. Kling, L. Dirscherl, and P. S. Dittrich, «Laser-assisted protein micropatterning in a thermoplastic device for multiplexed prostate cancer biomarker detection», Lab on a Chip **23**, 534–541 (2023).

Chapter 5

Conclusion and Outlook

In this dissertation we presented two novel microfluidic devices for the multiplexed quantification of secreted proteins from single cells at high throughput. We quantified the secretion of thousands of single cells employing a commercially available on-bead immune sandwich assay that has the potential to multiplex up to 100 target proteins. The combination of an open hexagonal microwell array with a two-phase system enables a high well density resulting in a throughput of up to 10^5 single cells. The microfluidic devices were used to analyse the secretion profile of macrophages and the impact of different stimuli on them. Specifically, the impact of stimuli from the tumour microenvironment was explored in more detail.

The first developed device enabled the capture of up to 1084 single cells in microchambers isolated by pneumatically activated valves. The introduction of hydrodynamic traps in combination with magnetic traps allowed the label-free capture of single cells and magnetic beads in the same microchambers. Compared to previous works in the group [1, 2], the single-bead magnetic traps improved the retention of beads, their automatic imaging and readout. A specifically designed magnetic arrangement of 14 neodymium magnets permitted bright field microscopy during the experimental procedures enabling morphological studies as well as improved imaging. The major limitations of the device presented in chapter 3 are the number of single-cell traps and the restricted multiplexing capability due to the number of magnetic traps inside each microchamber. For future studies, we further improved the design increasing the number of microchambers to 5184 (Fig. 5.1). This is achieved by fusing the pneumatic valves for each microchamber increasing the well density from 8.8 wells per square millimetre to 13.5 wells per square millimetre by more than 50%. Additionally, the number of magnetic traps in each microchamber was increased leading to more beads captured inside each chamber. The versatile platform is well suited to do fundamental studies in specialised labs where flexibility and multiple reagent exchanges are paramount, but it is ill suited for the commercial application. This is mainly due to the highly complex fabrication process of the pneumatic valve layer with PDMS and complicated assay protocol to perform single-cell secretion measurements. Furthermore, to achieve statistically significant results, it is crucial to increase the number of captured and assessed single cells even more.

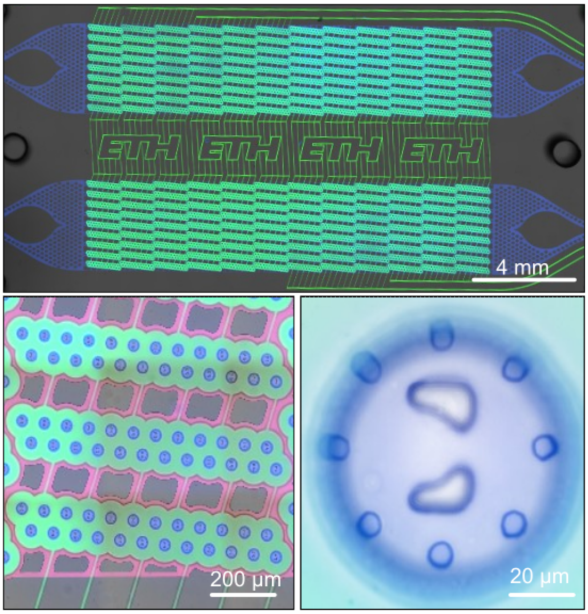

Figure 5.1: The proposed device has 5184 microchambers each containing a centrally located hydrodynamic trap for single-cell capture and 8 magnetic bead traps. The pneumatic control layer of neighbouring microchambers is fused together. This results in a higher microchamber density compared to the previous design.

The device presented in chapter 4 was developed with the shortcomings of the first device in mind. We increased the number of cell traps from 10^3 to 10^5 by two orders of magnitude. At the same time, the fabrication process was changed from soft lithography with PDMS as the device material to hot embossing of COC, a competitive fabrication method for commercial applications [3, 4]. The high well density of 415 wells per square millimetre is the result of smaller well sizes in combination to a different isolation technique avoiding the use of pneumatic valves. The challenge of cross-contamination in between such highly packed wells was overcome by immersing the microwell array in fluorinated oil during the incubation phase. The open microwell design not only offered higher well density, but also overcame a weakness of many microfluidic platforms: a complex assay protocol that requires trained personal. The microwell is loaded and operated with standard pipettes without the need for syringes or pressure pumps; the ever-present error source of air bubbles in closed microfluidic chips; or the clogging of microfluidic channels due to debris.

The developed microfluidic devices improved the previous systems substantially, but there is room for optimization. A major shortcoming of the microwell device is the lack of high-dimensional multiplexing of more than 10 proteins. Increasing the number of magnetic traps by reducing the bead size for the on-bead immune assay would be a simple optimization. The diameter size of the bead is limited by the resolution of the microscope used; however, reducing the bead diameter by half would increase the number of magnetic bead traps by a factor of four. An additional weakness is the spread of the fluorescent signal measured on different beads at the same concentration. This inter-bead variation reduces the precise determination of the protein concentration measured by each bead. This weakness can also be tackled by increasing the number of beads per protein in each well resulting in an average signal from multiple beads. In conclusion, we propose that a future platform should increase the number of beads in each well to improve the robustness of the readout for the device and enable higher dimensional multiplexing.

Similar to a 96-well plate, it would be beneficial to be able to perform triplicates of many conditions on one device. Up to four conditions could be analysed in parallel by using separately controllable valve arrays in the initial design. In the device presented in chapter 4 and the proposed design for a novel microchamber platform (Fig. 5.1), we doubled the number of paralleled conditions to eight. However, the microfluidic device presented was limited to a microscopy slide which has a six-time lower footprint than a 96-well plate. Therefore, using the same footprint of the device on the area of a 96-well plate results in more than 48 parallel conditions. To further increase the number of conditions, the implementation of radial polarised circular neodymium magnets could be considered. However, the size of permanent magnets is still the limiting factor which could be reduced by integrating electromagnets directly inside the microfluidic system [5].

As an application on both devices, the secretion of single macrophages was measured, and the impact of different stimuli investigated. With detection limits below 1150 molecules, we were able to characterize macrophages based on their secretion profile of up to 10 cytokines. We could show that macrophages treated with supernatant from breast cancer cells show characteristics of M2 like macrophages. Furthermore, the treatment with chemotherapeutics, paclitaxel and docetaxel, showed an increase in MIP-1α secretion indicating a potential drug target for a combinatorial treatment. Multiplexed measurements revealed the co-secretion of IL-10/VEGF when stimulated with IL-4/IL-13 and highlighted the MCP-1/OPN protein pair as an interesting pathway for further investigation. In total, we were able to correlate more than 40 proteins pairs due to the high number of wells. Up until now, we investigated the secretion of macrophages under different stimuli and could partially simulate the impact of the TME on the macrophages. In the future, it would be of interest to investigate the repolarization of macrophages from the M2 phenotype to the M1 phenotype by sequential treatment of different stimuli [6, 7]. The possibility to simultaneously measure intra cellular, membrane-bound, and secreted proteins qualifies the platform for precision medicine by analyzing single-cell suspension such as dissected tumour biopsies where sample volume is limited. The easy-to-use microwell device allows for the straightforward testing of the cell composition identifying its heterogeneity and detecting potential vulnerability against treatments.

In summary, the thesis presents a novel device for the quantitative measurement of secreted proteins from single cells at high throughput. We achieved an increased throughput of two orders of magnitude while reducing fabrication and handling complexity significantly. The developed device enables multiplexed secretion measurement at the single cell level, with potential uses in fundamental research, translational medicine or personalised medicine.

5.1 References

[1] L. Armbrecht, R. S. Müller, J. Nikoloff, and P. S. Dittrich, «Single-cell protein profiling in microchambers with barcoded beads», Microsystems and Nanoengineering **5**, 55 (2019).

[2] L. Armbrecht, O. Rutschmann, B. M. Szczerba, J. Nikoloff, N. Aceto, and P. S. Dittrich, «Quantification of protein secretion from circulating tumor cells in microfluidic chambers», Advanced Science **7**, 1903237 (2020).

[3] J. S. Jeon, S. Chung, R. D. Kamm, and J. L. Charest, «Hot embossing for fabrication of a microfluidic 3d cell culture platform», Biomedical Microdevices **13**, 325–333 (2011).

[4] G. Mehta, J. Lee, W. Cha, Y.-C. Tung, J. J. Linderman, and S. Takayama, «Hard top soft bottom microfluidic devices for cell culture and chemical analysis», Analytical Chemistry **81**, 3714–3722 (2009).

[5] R. Khojah, Z. Xiao, M. K. Panduranga, M. Bogumil, Y. Wang, M. Goiriena-Goikoetxea, R. V. Chopdekar, J. Bokor, G. P. Carman, R. N. Candler, and D. D. Carlo, «Single-domain multiferroic array-addressable terfenol-d (smart) micromagnets for programmable single-cell capture and release», Advanced Materials **33**, 2006651 (2021).

[6] C. W. Wanderley, D. F. Colón, J. P. M. Luiz, F. F. Oliveira, P. R. Viacava, C. A. Leite, J. A. Pereira, C. M. Silva, C. R. Silva, R. L. Silva, C. A. Speck-Hernandez, J. M. Mota, J. C. Alves-Filho, R. C. Lima-Junior, T. M. Cunha, and F. Q. Cunha, «Paclitaxel reduces tumor growth by reprogramming tumor-associated macrophages to an m1 profile in a tlr4-dependent manner», Cancer Research **78**, 5891–5900 (2018).

[7] M. Najafi, N. H. Goradel, B. Farhood, E. Salehi, M. S. Nashtaei, N. Khanlarkhani, Z. Khezri, J. Majidpoor, M. Abouzaripour, M. Habibi, I. R. Kashani, and K. Mortezaee, «Macrophage polarity in cancer: a review», Journal of Cellular Biochemistry **120**, 2756–2765 (2019).

Publications

Peer-reviewed articles

[1] C. L. Dietsche, E. Hirth, and P. S. Dittrich, «Multiplexed analysis of signalling proteins at the single-immune cell level», Lab on a Chip **23**, 362–371 (2022).

[2] C. L. Dietsche, L. Stöcklin, R. Dezauzier, R. Strutt, and P. S. Dittrich, «Wells-in-well microarray for multiplexed and quantitative analysis of cytokines from single macrophages», In preparation (2024).

[3] S. F. Berlanda, M. Breitfeld, C. L. Dietsche, and P. S. Dittrich, «Recent advances in microfluidic technology for bioanalysis and diagnostics», Analytical Chemistry **93**, 311–331 (2021).

[4] E. Hirth, W. Cao, M. Peltonen, E. Kapetanovic, C. Dietsche, S. Svanberg, M. Filippova, S. Reddy, and P. S. Dittrich, «Self-assembled and perfusable microvasculature-on-chip for modeling leukocyte trafficking», Lab Chip **24**, 292–304 (2024).

[5] E. Kapetanovi, C. R. Weber, M. Bruand, D. Pöschl, J. Kucharczyk, E. Hirth, C. L. Dietsche, R. Khan, B. Wagner, O. Belli, R. Vazquez-Lombardi, R. Castellanos-Rueda, R. B. D. Roberto, K. Kalinka, L. Raess, K. Ly, P. S. Dittrich, R. J. Platt, E. Oricchio, and S. T. Reddy, «Enhancing bispecific antibody therapies by engineering allogeneic t cells via molecular decoupling of the tcr-cd3 signaling complex», Accepted in Nature Biomedical Engineering (2023).

[6] A. Kling, J. M. Nikoloff, C. L. Dietsche, and P. S. Dittrich, «Enrichment and cargo analysis of extracellular vesicles derived from taxol treated breast cancer cells on a microfluidic device», In preparation.

[7] E. Hirth, C. L. Dietsche, M. A. Saucedo-Espinosa, W. Cao, E. Kapetanovic, D. Ritz, S. Reddy, and P. S. Dittrich, «Paracrine vegf secretion by polarized perivascular macrophages can induce self-assembled capillary formation and angiogenesis on-chip», In preparation (2024).

[8] L. R. Stöcklin, C. L. Dietsche, and P. S. Dittrich, «A microfluidic platform for the analysis of extracellular vesicles derived from single cancer cells», In preparation (2024).

[9] M. Breitfeld, C. L. Dietsche, M. A. Saucedo-Espinosa, S. F. Berlanda, and P. S. Dittrich, «High-throughput droplet-printing of concentration gradients for multimodal fluorescence- and maldi-ms analysis», In preparation (2024).

[10] M. Breitfeld, F. Born, I. Onipko, C. L. Dietsche, S. Berlanda, and P. Dittrich, «Formation of antibiotic gradients into picoliter droplet arrays for antimicrobial suscep. testing of e.coli», In preparation (2024).

Conference contributions

[1] L. Armbrecht, C. L. Dietsche, R. S. Müller, J. Nikoloff, and P. S. Dittrich, *Co-capture of magnetic beads and cells for single-cell analysis in microfluidic chambers*, 23th International Conference on Miniaturized Systems for Chemistry and Life Sciences (μTAS 2019).

[2] E. Hirth, C. Dietsche, T. Duncombe, D. Ritz, M. Filippova, and P. S. Dittrich, *Secretome analysis with simultaneous on-chip angiogenesis and anastomosis between human arterial and venous cells*, 24th International Conference on Miniaturized Systems for Chemistry and Life Sciences (μTAS 2020).

[3] C. Dietsche and P. S. Dittrich, *Deterministic co-encapsulation of beads and cells in nl-droplets for high throughput multiplexed single-cell analysis*, MaP Graduate Symposium 2020 (MaP 2020).

[4] C. L. Dietsche, E. Hirth, and P. S. Dittrich, *Multiplexed analysis of signaling proteins at the single immune cell level*, 25th International Conference on Miniaturized Systems for Chemistry and Life Sciences (μTAS 2021).

[5] C. L. Dietsche, E. Hirth, and P. S. Dittrich, *Multiplexed analysis of signaling proteins at the single immune cell level*, MaP Graduate Symposium 2021 (MaP 2021).

Author contributions

In the following, the contributions of Claudius L. Dietsche to the different journal publications presented in this thesis are listed:

Wells-in-well microarray for multiplexed and quantitative analysis of cytokines from single macrophages

C. L. Dietsche, L. Stöcklin, R. Dezauzier, R. Strutt, and P. S. Dittirich

In preparation (2024)

- Main contributions to all presented results.
- Design and fabrication of microfluidic devices.
- Performed all experiments on chip.
- Implemented a program for the anaylsis of large arrays.
- Evaluated all data.
- Wrote the manuscript.

Multiplexed analysis of signalling proteins at the single-immune cell level

C. L. Dietsche, E. Hirth, and P. S. Dittirich

Lab on a Chip **23**, 362-371 (2022).

- Main contributions to all presented results.
- Design and fabrication of microfluidic devices.
- Performed all experiments on chip.
- Implemented a program for the anaylsis of large arrays.
- Evaluated all data.
- Wrote the manuscript.

Recent Advances in Microfluidic Technology for Bioanalysis and Diagnostics

S. F. Berlanda, M. Breitfeld, C. L. Dietsche, and P. S. Dittirich

Analytical Chemistry **93**, 311-331 (2021).

- Reasearched chapter Materials and Fabrication.
- Wrote chapter Materials and Fabrication.

Acknowledgments

First of all, I would like to thank Prof. Petra S. Dittrich for giving me the opportunity to work and do my doctorate in her group. Her door was always open to discuss the project, she provided all the necessary financial support, and she welcomed novel ideas. Further, I want to thank Prof. Christoph Merten as my second supervisor for taking the time to listen to my progress through my PhD and giving me sound and constructive feedback. I also thank Prof. Ute Resch-Genger for listening to my problems and encouraging me during my time of struggles. Finally, I want to thank Prof. Barbara Treutlein for chairing my defence.

The people who made my time at the Dittrich Lab especially precious to me were my lab colleagues and friends. During my time in the group many people who are dear to me left and advanced in their life and careers. However, every time someone left, someone new joined and added to the group and the experience in the lab. Specially, I want to thank Elisabeth Hirth for being my office mate, collaboration partner, and my friend. I would like to thank Lucien Stöcklin for providing me macrophages and helping me to realize my project. Without him, I would still be doing my PhD. Special thanks go to my coworker and friend Maximilian Breitfeld for his input to my projects and always helpfull discussions. Furthermore, I thank Raphael Dezauzier and Dr. Robert Strutt for valuable discussions throughout my projects. I would like to acknowledge Theresa Emt and Alex Landolt who I have supervised and I hope that they have learned as much as I have during this time. Even though the recognized people are slightly focused on the people still remaining in the lab, I will never forget my first years and the fun we all had together.

Finally, I want to thank my family and friends who always supported me. They never doubted that I will accomplish what I started. I cannot express how grateful I am towards my parents and sister who are always there for me, listen to my problems, and help me feel better. Finally, I want to express my deep gratitude to my partner, Alexandra Gutzwiller, who always encourages me and helps me push through the hard times. Thank you all!